New Understanding of Iceberg Calving, Mass Loss, and Glacier Dynamics in Greenland Through Analysis of Glacial Earthquakes

Kira Olsen

Submitted in partial fulfillment of the
requirements for the degree of
Doctor of Philosophy
in the Graduate School of Arts and Sciences

COLUMBIA UNIVERSITY

2020

ABSTRACT

New Understanding of Iceberg Calving, Mass Loss, and Glacier Dynamics in Greenland Through Analysis of Glacial Earthquakes

Kira Olsen

I apply a suite of seismic techniques to investigate iceberg calving at large glaciers around Greenland. Iceberg calving accounts for up to half of the Greenland Ice Sheet's annual mass loss, which makes understanding the physics of the calving process vital to gaining a clear picture of current behavior and future evolution of the Greenland Ice Sheet. However, the varied and complex modes of calving behavior at individual glaciers, paired with the challenges to data collection presented by an actively calving glacier, mean that much remains unknown about the dynamics of calving at marine-terminating glaciers. Seismic data offer a unique opportunity to study this active phenomenon, by allowing remote observation of calving events and quantification of the forces active during calving.

Using seismic data collected during the most productive three years of buoyancy-driven calving on record, I estimate the forces active during iceberg calving at 13 glaciers around Greenland. My waveform-modeling results highlight the large number of buoyancy-driven calving events currently occurring at Jakobshavn Isbræ and other glaciers in west Greenland. I demonstrate that a glacier's grounded state exerts control on the production or cessation of rotational calving events and investigate the dynamics of calving at individual glaciers. I pair seismic results with terminus imagery to identify the location of individual calving events within calving sequences that occur over days to weeks at a single glacier terminus.

By applying a new cross-correlation technique to seismic data collected within

100 km of three of Greenland's largest glaciers, I identify the occurrence of buoyancy-driven calving events with iceberg volumes up to two orders of magnitude smaller than previously observed. These small calving events frequently occur within ∼30 minutes of a larger calving event. In between calving sequences, a glacier terminus changes little, suggesting that the majority of ice lost from marine-terminating glaciers occurs through these sequences. I estimate that these small events may contribute up to 30% more to dynamic mass loss than previously thought (up to 15 Gt/yr). I find no evidence of the cliff failure predicted by the marine-ice-cliff-instability hypothesis, in which catastrophic failure occurs when an ice cliff reaches a theoretical maximum-height limit, despite the three glaciers I investigate in detail having some of the tallest ice cliffs in the world.

I use independent constraints on iceberg size from high-quality terminus imagery to present the first demonstration of an empirical relationship between glacial-earthquake magnitude and iceberg size. I investigate this relationship further by considering additional metrics of glacial-earthquake magnitude, and find advantages to using maximum force, rather than the more commonly employed mass-distance product M_{CSF}, as a measure of glacial-earthquake size.

Through a detailed investigation into the character of the glacial-earthquake source, I identify key characteristics of the source function that generates the glacial-earthquake signal. I use experiments on both synthetic and observed waveforms to demonstrate that more-accurate estimates of glacial-earthquake size can be retrieved using source models constructed using a representation of the force history that is more sophisticated than that captured by the simple boxcar model. I confirm the presence of a correlation between iceberg volume and glacial-earthquake size, which moves us closer to having the ability to use remotely recorded seismic signals to quantify mass loss at Greenland glaciers. This work presents testable hypotheses for future model development.

Contents

List of Figures

List of Tables

Acknowledgements

Thank you to the many people of the Lamont community for all they have taught me, and for making these past five years so enjoyable and productive. I am grateful for the mentorship of my advisor Meredith Nettles who has provided me the opportunity to investigate exciting scientific questions, spend time in the field, pursue my interests in teaching, and has continuously supported me throughout my time at Lamont. Thank you to my committee members Göran Ekström and Spahr Webb for guidance during my graduate career. Thanks also to Jonny Kingslake and Geoff Abers for serving as my external defense-committee examiners. During my time at Lamont I have had the opportunity to take many wonderful and challenging classes and am appreciative of all of the professors who have shared their knowledge and broadened my understanding of our planet. My sincere thanks also to the Lamont administrators who have met my ideas and requests for projects, workshops, and trips with enthusiasm and support. Thank you to my stellar graduate-student peers who have made the seismology group such a fun one to be part of, and especially to my great office mates Zach Eilon and Chris Carchedi. I want to acknowledge with deep gratitude the love and support of my parents for a lifetime of encouragement to pursue the things I find exciting. Thank you also to my sister Svea for her friendship and support, especially as we have both made our way through our PhDs. And finally, thank you to my husband Dan for being my partner throughout.

Introduction

Greenland's ice sheet extends across 1.7 million km^2 and has undergone dramatic changes in recent years. Over the past two decades, the Greenland Ice Sheet has lost more mass annually than it has gained through snowfall, leading to an overall trend of mass loss at an accelerating rate (Khan et al., 2015). The changes that the Greenland Ice Sheet is undergoing have far-reaching effects. If fully melted, the ice within the Greenland Ice Sheet would raise global sea level by 7 m (Lemke et al., 2007) which would profoundly influence global ocean-circulation patterns (e.g., Böning et al., 2016). A clear understanding of how the Greenland ice sheet is behaving today, and of the processes that may affect its behavior in the future, is therefore vital.

The most significant changes to Greenland's mass balance are occurring at the ice sheet's margins (e.g., van den Broeke et al., 2009). In these regions, ice sits at low elevations where warm air temperatures drive melting. In addition, along significant portions of Greenland's coastline, ice in the lower reaches of marine-terminating glaciers comes into direct contact with ocean water, where it is subject to both submarine melting and iceberg calving. These mass-loss processes at the glacier terminus have a significant impact on the entire ice-sheet mass balance, as these processes not only impact the volumes of ice removed from the lowermost portions of the glacier, but also affect the velocity of a glacier tens of kilometers inland (Nettles et al., 2008). Our ability to understand the current ice-sheet system and accurately project its future behavior depends in large part on understanding and correctly accounting for the processes

occurring at the glacier terminus.

Iceberg-calving events are responsible for up to half of the ice lost annually from the Greenland ice sheet in recent years (Enderlin et al., 2014). The largest of these calving events occur at marine-terminating glaciers where a single calving iceberg can routinely remove up to a cubic kilometer of ice (e.g., James et al., 2014). Because glaciers exhibit a range of calving styles, and data collection is difficult at actively calving termini, development of a unified calving law has proved difficult, and the glaciology community lacks answers to many questions about the drivers of iceberg calving. This deficit stands in the way of a comprehensive understanding of ice-sheet evolution, and is a major source of uncertainty in projecting future ice-sheet mass balance and estimating sea-level rise under different climate scenarios (e.g., Nick et al., 2013).

Glacial environments are rich sources of seismic energy, which is generated by numerous brittle-failure and mass-movement processes such as iceberg calving, crevassing, and englacial and subglacial water transport. The elastic waves produced by these processes readily couple with the solid Earth and travel long distances, which allows study of glacier deformation and the forces active during calving from teleseismic distances.

The largest seismic signals emitted by glaciers are the magnitude $\sim$5 events known as glacial earthquakes (Ekström et al., 2003) which are generated by buoyancy-driven calving of icebergs up to 1 km^3 in volume. Glacial earthquakes occur when a tall, narrow iceberg capsizes against a glacier's terminus, and the rotating iceberg and the water it displaces exert a force on the calving front (Nettles and Ekström, 2010; Murray et al., 2015a). These long-period seismic events are recorded by the Global Seismographic Network (GSN) at locations thousands of kilometers away from the source glacier. As I demonstrate in the first chapter of this dissertation, glacial earthquakes occur only when a glacier terminates close to its grounding line, a condition that is satisfied by

many of Greenland's glaciers but is not typical of the ice margins around Antarctica. As a result, the vast majority of glacial earthquakes occur in Greenland.

Glacial earthquakes occur more slowly than tectonic earthquakes of comparable magnitude, and as a result they predominantly generate seismic energy at periods longer than 25 s. These source characteristics, combined with the earthquakes' unexpected location along the coast of tectonically inactive Greenland, delayed their discovery until 2003 (Ekström et al., 2003). Since then, systematic analysis has identified glacial earthquakes at 15 of Greenland's largest glaciers (Tsai and Ekström, 2007; Veitch and Nettles, 2012; Olsen and Nettles, 2017), and has tracked the northward progression of event onset at glaciers along Greenland's west coast (Veitch and Nettles, 2012).

Much of the glacial-earthquake analysis I undertake in this dissertation is based on a waveform-modeling technique similar to that used for centroid-moment-tensor (CMT) analysis of tectonic earthquakes (e.g., Dziewoński et al., 1981). Gravity-driven seismic sources such as landslides and glacial earthquakes are appropriately described by a single force that reverses direction as a mass first accelerates and then decelerates. Adaptation of the CMT formalism (Kawakatsu, 1989; Ekström et al., 2003) allows centroid-single-force (CSF) modeling of such sources. Initial glacial-earthquake detections are identified using the surface-wave detection algorithm of Ekström (2006), which gives initial estimates of centroid location and time. I manually select seismograms with high-quality recordings of each glacial earthquake, typically including data from 30–40 seismic stations with high signal-to-noise ratios at the time of each event. I perform an iterative, full-waveform CSF inversion to solve for the amplitude and orientation of the force that generated the glacial earthquake, as well as its centroid location and time. The excitation of seismic waves is calculated using the preliminary reference Earth model (PREM; Dziewoński and Anderson 1981); lateral variation in velocity structure encountered by the propagating surface waves is accounted for using the phase-velocity

maps of Ekström et al. (1997), following the approach of Ekström et al. (2012). In most of this work, I use a simple, fixed model for the shape of the force function, a choice that is explored in the later part of this thesis. For each glacial earthquake, the solution quality is evaluated based on the stability of the estimated source parameters, waveform fit, and other characteristics such as the azimuthal distribution of available data constraints.

In the first chapter of this dissertation I use this waveform-modeling approach to investigate a recent three-year period of glacial-earthquake activity that was the most productive on record. By analyzing 139 glacial-earthquake events I expand the glacial-earthquake catalog by nearly 50% (Olsen and Nettles, 2017). I use this robust catalog of recent events to investigate the relationship between the occurrence of glacial earthquakes and a glacier's grounding state, as well as to investigate calving patterns at individual glaciers and constrain the timing of changes in terminus geometry.

Glacial earthquakes have historically been identified using the surface-wave detection algorithm of Ekström (2006) and seismic data recorded primarily at stations within the GSN. Over the past decade the Greenland Ice Sheet Monitoring Network (GLISN; Clinton et al. 2014) has greatly improved broadband seismic instrumentation around Greenland through high-quality installation of seismometers both on and off the ice sheet, including a limited number of stations located within 100 km of some of the largest glaciers. In the second chapter of this dissertation I use this improved instrumentation to investigate seismic signals with amplitudes below the detection threshold of the automated detector. Using a cross-correlation detection technique I identify small, long-period seismic signals, concentrating my efforts on the hours immediately preceding and following cataloged glacial earthquakes. I investigate the possibility of a triggering mechanism preceding large-scale calving in locations where ice cliffs reach $\sim$100 m tall, a theoretical limit for cliff stability (Bassis and Walker, 2012), and evaluate

the buoyancy-driven calving budget.

An understanding of the relationship between iceberg volume and glacial-earthquake magnitude has long been sought. Determination of such a relationship would allow remote estimation of mass loss through calving at glaciers around Greenland using permanent seismic stations, without the need for deployment of local instruments, daylight, or cloud-free skies for clear observations. Scaling relationships between seismic magnitude and source area are applied to aid understanding of tectonic earthquakes and landslides, but development of such a relationship for glacial earthquakes has been hindered in part by the relatively narrow range of magnitude values displayed by events in the glacial-earthquake catalog (Tsai and Ekström, 2007; Veitch and Nettles, 2012; Olsen and Nettles, 2017). However, my discovery and analysis of glacial earthquakes generated by smaller icebergs, combined with robust iceberg-volume estimates from ground-based high-frame-rate imagery, allows me to demonstrate an empirical relationship between iceberg area and one measure of iceberg size, the CSF amplitude M_{CSF} (Olsen and Nettles, 2019).

M_{CSF} is calculated by twice integrating the force-time function returned in waveform modeling, and this metric has known limitations because of its dependence on assumptions made about the force-time history of the seismic source. I devote the third chapter of this dissertation to an in-depth investigation of the seismic source of glacial earthquakes, and the effect that source-modeling choices have on the recovery of glacial-earthquake source parameters. I construct and test a suite of more-sophisticated models of the glacial earthquake source against both synthetic and observed glacial-earthquake waveforms. I incorporate new constraints on the character of the glacial-earthquake force history from numerical models (Sergeant et al., 2018) and laboratory and field observations of calving (Murray et al., 2015a; Cathles et al., 2015). I identify key model characteristics that affect recovery of source parameters, and investigate the

correlation of maximum force with iceberg mass.

Chapter 1

Patterns in Glacial-Earthquake Activity Around Greenland, 2011–2013

This chapter has been previously published as:

Olsen, K. G., and M. Nettles (2017), Patterns in Glacial-Earthquake Activity Around Greenland, 2011–13, *Journal of Glaciology*, *63*(242), 1077–1089, 10.1017/jog.2017.78.

Abstract

Glacial earthquakes are caused by large iceberg calving events, which are an important mechanism for mass loss from the Greenland ice sheet. The number of glacial earthquakes in Greenland has increased six-fold over the past two decades. We use teleseismic surface waves to analyze the 145 glacial earthquakes that occurred in Greenland from 2011 through 2013, and successfully determine source parameters for 139 events at 13 marine-terminating glaciers. Our analysis increases the number of events in the glacial-earthquake catalog by nearly 50 % and extends it to 21 years. The period 2011–13 was the most prolific three-year period of glacial earthquakes on record, with most of the increase over earlier years occurring at glaciers on Greenland's west coast. We investigate changes in earthquake productivity and geometry at several individual glaciers and link patterns in glacial-earthquake production and cessation to the absence or presence of a floating ice tongue. We attribute changes in earthquake force orientations to changes in calving-front geometry, some of which occur on timescales of days

to months. Our results illustrate the utility of glacial earthquakes as a remote-sensing tool to identify the type of calving event, the grounded state of a glacier, and the orientation of an active calving front.

1.1 Introduction

Icebergs calved from marine-terminating glaciers currently account for up to half of the ∼400 Gt of ice lost annually from the Greenland ice sheet (Enderlin et al., 2014). Some large calving events (∼1 Gt of ice) cause glacial earthquakes of seismic magnitude M_{SW} ∼5 (Ekström et al., 2003). Globally detectable seismic signals are generated when icebergs that extend the full thickness of the calving front rotate and accelerate away from a near-grounded glacier terminus (Amundson et al., 2008; Nettles et al., 2008; Tsai et al., 2008; Nettles and Ekström, 2010; Veitch and Nettles, 2012; Murray et al., 2015a). The iceberg acceleration produces a horizontal force on the solid Earth in a direction approximately perpendicular to the calving face (Tsai and Ekström, 2007; Nettles and Ekström, 2010; Veitch and Nettles, 2012), while a pressure drop behind the calving iceberg produces a small upward-directed force (Murray et al., 2015a).

The glacial-earthquake record provides a uniquely long-term and year-round time series of calving at Greenland's glaciers. Many glaciers lack field observations entirely, and even field campaigns at the best-studied glaciers collect data over a limited number of seasons. Satellite images offer incomplete records of large calving events due to the low time resolution of repeat imagery and to data gaps associated with cloud cover and winter darkness. By contrast, the continuous glacial-earthquake record provides information about changes to the geometry of a glacier's terminus between satellite image acquisitions and closely constrains the timing of rotational calving events. The glacial-earthquake record also complements other types of observations by providing information on the forces that are active during rotational calving events and by iden-

tifying a glacier's grounded state.

Over the past two decades, the region over which glacial earthquakes occur has expanded northward in Greenland (Veitch and Nettles, 2012) and the number of earthquakes has increased by a factor of six (Ekström et al., 2006; Nettles and Ekström, 2010), consistent with other observations of increased calving, mass loss and glacier thinning around Greenland (Howat et al., 2007; Howat and Eddy, 2011; Moon et al., 2012; Murray et al., 2015b; Harig and Simons, 2016). Patterns at individual glaciers correspond to independently observed changes in glacier dynamics: glacial-earthquake occurrence typically increases as a glacier accelerates, thins, and retreats (Veitch and Nettles, 2012).

Glacial earthquakes can be modeled as a single force using an approach developed for seismic analysis of landslides (Kawakatsu, 1989; Ekström et al., 2003; Tsai and Ekström, 2007; Veitch and Nettles, 2012). In this study, we use the methods employed by Tsai and Ekström (2007) and Veitch and Nettles (2012) to model waveforms for 145 glacial earthquakes that occurred between 2011 and 2013 (Figure 1.1). Our results increase the glacial-earthquake catalog by 46 % and allow us to assess the recent behavior of individual glaciers and analyze regional trends. We investigate patterns in glacial-earthquake production and cessation and changes in earthquake force orientation, comparing our results with constraints from satellite remote-sensing data.

1.2 Data and Methods

1.2.1 Glacial-Earthquake Detection

We identify glacial earthquakes using the approach of Ekström (2006), which uses intermediate-period (35–150 s) Rayleigh waves to identify seismic events. The long source durations (∼50 s) of the earthquakes result in seismograms depleted in high-

frequency energy and make the events imperceptible to standard short-period body-wave detection algorithms (Ekström et al., 2003). Detections are made using seismic data recorded by the IRIS-USGS Global Seismographic Network (GSN), GEOFON, GEOSCOPE, and MedNet Networks, and the Greenland Ice Sheet Monitoring Network (GLISN). The long wavelengths of the surface waves used by the detection algorithm (a 50-s Rayleigh wave has a wavelength of ∼200 km) lead to initial detection locations with uncertainties of 50–80 km (Ekström, 2006; Veitch and Nettles, 2012). We use the detection locations and times as inputs for waveform modeling for all events.

The event detector is run in near-real time and again several months later to include delayed seismic data. All events detected using the full dataset, including those initially detected in near-real time, are labeled 'standard' detections. A few events are identified only during the initial near-real-time processing; we label these 'NRT' detections. We perform waveform analysis on both standard and NRT detections and present the solutions for both types in the interest of catalog completeness. However, because NRT detections are not available for the earliest years of the catalog, we include only the standard detections in our discussion of spatiotemporal trends, consistent with previously published results (Tsai and Ekström, 2007; Veitch and Nettles, 2012). At the beginning of 2014, changes to the event detector altered the magnitude threshold for glacial-earthquake detection. We present data in this study only through the end of 2013 in order to allow direct comparison of the numbers of glacial earthquakes in 2011–13 with the previously published catalog of events from 1993–2010.

1.2.2 Waveform Modeling

Following previous authors (Tsai and Ekström, 2007; Veitch and Nettles, 2012), we use a centroid-single-force (CSF) approach (Kawakatsu, 1989; Ekström et al., 2003) to model the forces active during glacial earthquakes. We estimate six source parameters: the

centroid time shift from the original detection time, the centroid latitude and longitude, and the three components of the force vector. A summary measure of the earthquake size, M_{CSF}, analogous to the seismic scalar moment for tectonic earthquakes, is derived by integrating the force-time history twice. Though glacial earthquakes occur at Earth's surface, previous experiments confirm that modeling results are only weakly sensitive to the choice of source depth above 15 km (Veitch and Nettles, 2012). We calculate source excitation in the preliminary reference Earth model (PREM; Dziewoński and Anderson, 1981), and fix the source depth at 4 km to take into account the 3-km-thick ocean layer in that model.

We filter the seismograms to ground velocity in the period band 50–150 s or to displacement in the period band 40–100 s. Stations within 50° epicentral distance of the events generally show the highest-quality seismograms, and we handpick ∼30 of these stations to use for each event, aiming for good azimuthal coverage. Vertical-, transverse-, and longitudinal-component seismograms are considered and all three are used when possible. We perform full-waveform inversions using the CSF approach for all events in our dataset. Consistent with previous studies (Ekström et al., 2003; Tsai and Ekström, 2007; Veitch and Nettles, 2012), we specify a force-time function with a duration of 50 s such that a constant force acts on the Earth for 25 s as the iceberg accelerates and then reverses sign for an additional 25 s as the iceberg decelerates. We evaluate our inversion results based on the fit of synthetic seismograms to the data, stability of the source parameters, and residual variance of the solution, using criteria similar to those of the Global Centroid-Moment-Tensor (GCMT) project (Ekström et al., 2012).

1.3 Results

We analyzed a total of 145 glacial earthquakes in Greenland during 2011–13: 105 standard detections (Figure 1.2), one poorer-quality standard detection, and 39 NRT detections. We obtained satisfactory solutions for all but six of the events. The source parameters are listed in Table 1 and are available electronically on our website, www.globalcmt.org. As in previous studies, our centroid locations lie systematically closer to glacier calving fronts than the initial detection locations, which allows us to identify the source glacier for each glacial earthquake. The events in our dataset have CSF amplitudes ranging from 0.13×10^{14} kg m to 1.1×10^{14} kg m with a median value of 0.31×10^{14} kg m. These amplitudes are very similar to those found by Veitch and Nettles (2012). We observe glacial-earthquake force vectors generally oriented normal to the calving front (Figure 1.3). In Table 1 and throughout the text, we present all force azimuths in degrees east of north.

The majority of the glacial earthquakes we analyze occur at twelve previously documented source glaciers around Greenland (Tsai and Ekström, 2007; Veitch and Nettles, 2012). Over 65 % of the events produced each year between 2011 and 2013 occurred at glaciers on Greenland's west coast (Figure 1.2). We document two events at Sermeq Silardleq, a glacier on Greenland's west coast where glacial earthquakes have not previously been recorded. We do not observe any events at Rolige Bræ or Daugaard-Jensen Glacier, both of which are located on Greenland's east coast and previously produced glacial earthquakes (Figure 1.1; Tsai and Ekström, 2007; Veitch and Nettles, 2012).

Noisy data prevent good solutions for two of the glacial-earthquake detections, at Tracy Glacier and Upernavik Isstrøm. We are also unable to obtain satisfactory CSF solutions for four events on the southeast coast of Greenland. For these events, we are unable to identify the source glacier confidently, though the events appear to

occur in the region bounded by Helheim Glacier and Køge Bugt. We have manually inspected the detection stacks for all six events and confirmed that the detections represent earthquake signals, very likely originating from glacial earthquakes. Detection parameters for these events are included in Table 2.

1.4 Discussion

1.4.1 Glacial-Earthquake Distribution Patterns

The annual number of glacial earthquakes has increased significantly since 1993 (Tsai and Ekström, 2007; Veitch and Nettles, 2012), and 2011–13 was the most prolific three-year period of glacial-earthquake production on record. Most of the increase in earthquake numbers is due to increased production on the west coast. The years 2011–13 produced the largest number of glacial earthquakes in western Greenland ever recorded, continuing a trend of increased production at west-coast glaciers that began in 2000. During this period, three times as many glacial earthquakes occurred on Greenland's west coast as on the east coast (Figure 1.2). Seven glaciers each produced twice as many glacial earthquakes as in the preceding three years. All of these glaciers are located in western Greenland: Jakobshavn Isbræ, Upernavik Isstrøm, Alison Glacier, Tracy Glacier, Rinks Glacier, Hayes Glacier, and Giesecke Bræer. In addition, we record two glacial earthquakes at a previously quiescent glacier on Greenland's west coast.

1.4.2 Links Between Glacier Dynamics and Glacial Earthquakes

The ongoing production of glacial earthquakes, primarily at glaciers with previously documented earthquakes, is consistent with continued retreat and calving at these glaciers (e.g., Carr et al., 2013) and ongoing mass loss from western Greenland (Velicogna

et al., 2014). In the remainder of this section, we focus on six glaciers where the glacial earthquakes show unexpected or unusual behavior that allows us to examine particular aspects of the link between glacial earthquakes and glacier dynamics. We consider changes in earthquake occurrence rate in the context of a proposed grounding-condition control on these events, motivated in part by increasing interest in determining the grounded state of a glacier terminus (e.g., Hogg et al., 2016). Previous observations have linked the occurrence of glacial earthquakes to conditions at the glacier terminus, with glacial earthquakes occurring only at glaciers with near-grounded termini (Veitch and Nettles, 2012; Murray et al., 2015c).

The association between a nearly grounded terminus and earthquake occurrence is likely explained primarily by the control the grounding condition exerts on calving style: floating termini generally calve large, tabular icebergs that do not rotate and do not generate earthquakes (Amundson and Truffer, 2010; Veitch and Nettles, 2012), and nearly grounded termini calve smaller, tall icebergs that capsize (Amundson et al., 2008; Veitch and Nettles, 2012; Murray et al., 2015c). Murray and others (2015a,c) have argued for a close link between a buoyant-flexure calving mechanism and the glacial earthquakes, with the same buoyancy force that drives formation of basal crevasses and leads to calving causing the iceberg capsize that generates the earthquake signal.

We also evaluate changes in glacial-earthquake force azimuths to assess the variability that may occur at individual glaciers. Observed force azimuths generally agree well with the normal to the section of the terminus that produced the calving iceberg (Veitch and Nettles, 2012, 2017; this study). We consider force azimuths that deviate from long-term trends at several glaciers to evaluate links to changes in glacier geometry and calving style. Figure 1.4 shows time series of glacial earthquakes at the six glaciers we examine in detail, and Figure 1.5 shows the geometries of these glaciers' calving fronts along with force azimuths of recent glacial earthquakes.

1.4.3 Jakobshavn Isbræ

Jakobshavn Isbræ, Greenland's largest outlet glacier, has alternated between years when it maintained a floating ice tongue and did not produce recorded glacial earthquakes (1993–97 and 2000–04) and years when the calving margin was near a grounding line or pinning point and the glacier produced glacial earthquakes (1998–99 and 2005–13; Veitch and Nettles, 2012; this study). From 1998 through 2012, Jakobshavn Isbræ produced no more than seven glacial earthquakes in any one year (Figure 1.4). In 2013, Jakobshavn produced sixteen events, more than 50 % of the total number of events on Greenland's west coast and 38 % of the total number of glacial earthquakes in Greenland that year.

The ice dynamics, geometry, and position of Jakobshavn's calving front in 2013 illustrate the ideal conditions for glacial-earthquake production. Increased ice velocities have previously been linked to increased glacial-earthquake production (Veitch and Nettles, 2012). Ice velocities near Jakobshavn's terminus increased by 50 % between summer 2011 and 2012, and summer velocities in 2012 and 2013 included the fastest ice speeds, up to 17 km a^{-1}, ever recorded at an outlet glacier or ice stream in Greenland (Joughin et al., 2014). In 2013, the glacier occupied the most-retreated terminus position observed there (Joughin et al., 2014). During 2013, Jakobshavn's terminus was very close to flotation, and therefore in a position favorable for buoyancy-driven calving (James et al., 2014), which produces glacial earthquakes (Murray et al., 2015a). During the three winters prior to 2013, Jakobshavn's terminus advanced less than it had during any of the preceding ten winters (Cassotto et al., 2015). Reduced readvance and a diminished floating ice tongue would be expected to hasten the onset of glacial earthquakes in the spring. We speculate that the high numbers of glacial earthquakes produced in 2013 compared to 2011 and 2012 were caused by an earlier onset of mélange breakup in 2013. In 2013, glacial-earthquake production began in March and continued

through September, in contrast to the previous two years when the summer onset of glacial earthquakes occurred in June. The presence of a strong ice mélange in contact with Jakobshavn's terminus has been observed to inhibit calving events (Amundson et al., 2010; Cassotto et al., 2015). The early onset of glacial earthquakes in 2013 suggests that Jakobshavn lacked a strong, rigid mélange that spring, possibly due to unusually warm sea-surface temperatures like those observed in the fjord during the winters of 2010, 2011, and 2012 by Cassotto and others (2015).

Most glacial-earthquake force azimuths at Jakobshavn Isbræ are consistent with calving at the glacier's southern terminus. The Jakobshavn terminus is unusually broad, being fed by two separate regions of fast-flowing ice, which now terminate in two separate calving fronts (Figure 1.5). The terminus widened to its current geometry in 2004, when it retreated beyond the confines of its rock-bounded fjord (Dietrich et al., 2007). Veitch and Nettles (2017) show that glacial-earthquake force orientations between 2005 and 2010 are consistent with sources on the southern calving front, which is associated with the faster-flowing of the two ice streams. With one exception, all glacial earthquakes between 2011 and 2013 also have force azimuths consistent with the southern calving front ($\sim$130°, Figure 1.5), suggesting that this remains the source of recent glacial earthquakes. The single earthquake with an anomalous force azimuth, of 8°, occurred in 2011. This azimuth falls within the range of calving-front-normal orientations found along the fast-flowing portion of the northern section of the calving front. No glacial earthquakes with this force orientation have previously been documented, though the northern section of the calving front is known to calve actively, and had ice velocities of $\sim$2.5 km a^{-1} from 2011–13 (Joughin et al., 2008b, 2014).

1.4.4 Alison Glacier

After 25 years with a stable terminus position, Alison Glacier on Greenland's northwest coast began a rapid retreat in the summer of 2001 (Carr et al., 2013). From 2001–06, the glacier retreated ∼8.5 km (McFadden et al., 2011; Carr et al., 2013) and produced its first glacial earthquakes: one each year in 2003, 2005, and 2006 (Veitch and Nettles, 2012). During 2007 and 2008 the terminus position stabilized again (McFadden et al., 2011). The glacier produced four earthquakes in 2007 and two earthquakes in 2008 (Veitch and Nettles, 2012). Through 2008, all glacial earthquakes at Alison had force azimuths oriented perpendicular to the northern portion of the glacier's calving margin (Veitch and Nettles, 2012; see also Figure 1.6). No glacial earthquakes occurred in 2009 or 2010, though the terminus continued to retreat (Carr et al., 2013). Landsat images from the summer calving seasons in these years show large, tabular icebergs in the fjord, consistent with the aseismic calving expected from a floating glacier tongue. The hiatus in glacial-earthquake production from 2009–10 despite continued retreat suggests that Alison Glacier may have dynamically thinned to flotation during these years.

Glacial earthquakes resumed at Alison Glacier in the summer of 2011 and we observe a distinct change in glacial-earthquake force orientation between June and July of that year. A glacial earthquake at Alison Glacier on 29 June 2011 had a force azimuth of 55°, perpendicular to the northernmost portion of the calving front and similar to all previously documented glacial-earthquake force orientations at this glacier (Fig1.6). One month later, on 27 July 2011, a glacial earthquake occurred with a force azimuth oriented 143°, nearly perpendicular to the orientation of the preceding event. Three subsequent glacial earthquakes recorded at Alison Glacier in 2012 and 2013 have force orientations similar to the July 2011 event and ∼105° from the mean orientation of all pre-2011 events. No further events with force azimuths aligned with the pre-2011 events were recorded through 2013 (Figure 1.5).

During the two weeks prior to the change in glacial-earthquake force orientation in July 2011, Landsat imagery shows the northernmost portion of Alison Glacier retreating to a rock outcrop, where it remained fixed through the end of 2013. In contrast, the central and southern portions of the terminus continued to retreat through 2013. The four events occurring from 27 July 2011 onwards all had force azimuths consistent with calving from the southern portion of the terminus. We interpret the observed change in force azimuths as reflecting a change in the portion of the calving margin responsible for seismogenic calving events, as well as reflecting the overall change in calving-front orientation that occurred between 2008 and 2011.

1.4.5 Helheim Glacier

Helheim Glacier has produced glacial earthquakes every year since 1996, but has exhibited significant year-to-year variability in the number of events produced (Figure 1.4). During the early 2000s, Helheim produced increasing numbers of glacial earthquakes (Tsai and Ekström, 2007) as it thinned, accelerated, and retreated. The glacier reached a minimum position in its fjord in summer 2005 after retreating 4 km between August 2004 and August 2005 (Howat et al., 2005). During 2006, the terminus position advanced (Joughin et al., 2008a) and re-stabilized (Bevan et al., 2012). The annual number of glacial earthquakes has been variable since that time (Veitch and Nettles, 2012; this study). During 2011, 2012, and 2013 Helheim produced one event, seven events, and nine events. The glacier maintained a relatively stable calving-front position throughout 2011, 2012, and the first half of 2013, before advancing $\sim$3 km during the end of 2013 and beginning of 2014 (Kehrl et al., 2017).

The force orientations of glacial earthquakes at Helheim have evolved over time (Veitch and Nettles, 2012, 2017; Figure 1.7). Through 2005, the mean force azimuth was 96°. After the advance and stabilization of the terminus in 2006, force azimuths

at Helheim Glacier changed markedly, with a mean of 120° for earthquakes in 2006–13. Comparison between glacial-earthquake force orientations and calving-front orientations by Veitch and Nettles (2017) suggest that the source of seismogenic calving events at Helheim Glacier shifted from the southern portion of the calving front to the northern portion in 2005. Consistent with this interpretation, observations from summer 2013 show flexion zones only on the north side of the glacier terminus (Murray et al., 2015c). Flexion zones are linked with basal crevasses and the future detachment location of capsizing icebergs, and their presence along the northern portion of the calving margin suggests that this portion of the ice experiences the forces required for buoyancy-driven rotational calving. The absence of flexion zones along the southern portion of the calving front suggests that this portion of the terminus may not calve through the same mechanism (Murray et al., 2015c), explaining a lack of glacial earthquakes on the southern side of the glacier. The mean force orientation of glacial earthquakes between 2011 and 2013 (Figure 1.5) is within two degrees of the mean value from 2006 through 2010, suggesting that the northern portion of the calving front remained the source of glacial earthquakes from 2011 through 2013. The synchronous change in force azimuths and terminus position before and after the rapid retreat in 2005 suggests that the position of the glacier's terminus within the fjord is the main control on terminus geometry and glacial-earthquake orientation (Figure 1.7).

1.4.6 Kangerdlugssuaq Glacier

Kangerdlugssuaq Glacier was one of the most active producers of glacial earthquakes from 1993 through 2012 (Veitch and Nettles, 2012; this study). No glacial earthquakes were detected during 2013, for the first time since 1993 (Figure 1.4). The glacier maintained a relatively steady mean calving-front position through 2004, before retreating ∼5 km during 2004–05 (Seale et al., 2011). By 2006, the glacier had stabilized

and resumed steady seasonal cycles of advance and retreat (Seale et al., 2011), with earthquakes occurring during the retreat phase. During the first half of 2013, Kangerdlugssuaq advanced and produced a floating ice tongue, moving the calving front ∼6 km down the fjord (Kehrl et al., 2017). Satellite imagery of Kangerdlugssuaq in 2013 indicates that, during the glacier's advance, no large icebergs of any kind were produced. When retreat began late in the year, tabular icebergs made up the largest fraction of icebergs produced by the glacier, and few non-tabular icebergs were observed (Kehrl et al., 2017). The lack of seismicity in 2013 is consistent with our understanding that a glacier's calving margin must be near its grounding line to produce the kind of non-tabular, capsizing icebergs that are responsible for glacial earthquakes, while a floating glacier tongue will not produce glacial earthquakes.

1.4.7 Kong Oscar Glacier

The terminus position at Kong Oscar Glacier has been one of the most stable in the region since 2002, when the glacier is believed to have grounded and glacial earthquakes began to occur (Figure 1.4; Veitch and Nettles, 2012). Excluding five events with unusual azimuths discussed by Veitch and Nettles (2017), the mean orientation of previously documented glacial earthquakes at Kong Oscar Glacier is ∼50°. This orientation is well aligned with the eastern portion of Kong Oscar's calving front through 2010 (Veitch and Nettles, 2017). We analyze 16 glacial earthquakes at Kong Oscar Glacier, of which six have azimuths that differ significantly from the majority of previously published force azimuths. The remaining 2011–13 events have a mean orientation of ∼30° (Figure 1.5). This azimuth is consistent with continued calving from the eastern portion of the terminus.

The events with unusual azimuths in 2011–13 have force azimuths of 101° (one event) or 166°–183° (five events). Satellite observations from 2011–13 show active

retreat at both the western and eastern edges of the calving front. During these years, the westernmost 2 km of Kong Oscar's calving front was aligned approximately east–west, consistent with production of glacial-earthquake force azimuths oriented ∼180°. We therefore attribute the five glacial earthquakes with force azimuths of 166°–183° to calving events along the western portion of the calving front. There is one previously published event at Kong Oscar with an azimuth comparable to these events (Tsai and Ekström, 2007). There is no clear explanation for the event in 2011 with a force azimuth of 101°, or for two previously published events at Kong Oscar Glacier in 2007 with similar force azimuths (Veitch and Nettles, 2017). The solutions for all three of these glacial earthquakes appear robust. We examined Landsat imagery at the times of these events in detail and are unable to identify an actively calving terminus region that would be expected to generate seismic forces with this orientation.

A set of four glacial earthquakes at Kong Oscar in late September and early October 2013 demonstrate the possibility of rapid variation in force azimuths at a single glacier. The earthquakes occurred over a nine-day period, and had orientations of 22°, 173°, 62°, and 162°, respectively (Figure 1.8). We interpret this sequence as a series of calving events alternating between the western and eastern portions of the terminus. We visually inspect three Landsat images that capture the terminus position during this calving sequence. An image taken on 27 September 2013 shows the orientation of Kong Oscar's calving front before the sequence of four earthquakes. The first earthquake in the sequence occurred on 29 September 2013 with a force orientation of 22°. A Landsat image taken less than two hours after this calving event shows ice missing from the western portion of the calving front compared to the previous image. The next glacial earthquake occurred on 3 October 2013, with a force azimuth of 173°. Comparison of this event with a Landsat image taken on 6 October 2013 shows that this event and the next calving event, on 5 October 2013, removed ice from the eastern portion of the

terminus. The final earthquake in this sequence occurred on 7 October 2013, with a force azimuth of 162°. The force azimuth of this event is consistent with calving from the western portion of the terminus.

Previous studies have documented multiple seismogenic calving events at a single glacier in close succession (Nettles et al., 2008; Walter et al., 2012; Sergeant et al., 2016), suggesting that one calving event may trigger a second, and a wide glacier terminus might calve by progressive failure along the width of the front. The close alignment of glacial-earthquake force azimuths with subsections of the calving front at Kong Oscar Glacier illustrates the utility of glacial-earthquake azimuth data in identifying the subsection of a calving margin that generated a glacial earthquake, and in tracking the progression of failure across a glacier's terminus. During 2011–13, we observe ten additional pairs of glacial earthquakes in Greenland that occurred on the same day at a single glacier. Multiple-earthquake sequences, such as the sequence of four events in late September–early October 2013 at Kong Oscar, suggest that failure of one section of the calving front may alter the local stress regime enough to influence other portions of the calving front hours to days later.

1.4.8 Sermeq Silardleq

We document two glacial earthquakes at Sermeq Silardleq (Figure 1.4; Figure 1.5), a previously quiescent glacier that terminates in Uummannaq Bay on Greenland's west coast. Sermeq Silardleq is 3.3 km wide at its terminus (Jensen et al., 2016), which makes it the smallest glacial-earthquake-producing glacier in Greenland. Between 2000 and 2010, Sermeq Silardleq experienced ∼3 km of retreat, then maintained a stable terminus position during 2011, 2012 and 2013 (York et al., 2016). The events we observe occurred in 2011 and 2013. The pattern of retreat, followed by the onset of glacial earthquakes, is consistent with that seen at numerous other glaciers around Greenland. The stable

terminus position from 2011–13, along with the onset of glacial earthquakes, suggests that the calving front was close to grounded during all three of those years. Warm Atlantic water is a possible cause of the retreat to the grounding line. This water is known to enter Uummannaq Bay along a bathymetric trough in the continental shelf (Rignot et al., 2016). Such water has been a driver of sub-glacial melting at other glaciers in Uummannaq Bay close to Sermeq Silardleq (Chauché et al., 2014) and of acceleration at nearby Jakobshavn Isbræ (Holland et al., 2008).

1.5 Conclusions

We analyzed three years of seismic data, 2011–13, and obtained source parameters for 139 glacial earthquakes. Our results extend the glacial-earthquake catalog to 21 years and increase the number of events in the catalog by nearly 50 %. Our study period is the most prolific three-year period of glacial earthquakes on record. Much of the increase in earthquake productivity is due to glaciers on Greenland's northwest coast, seven of which generated twice as many glacial earthquakes during 2011–13 as during the preceding three years. These seven glaciers accounted for 60 % of all glacial earthquakes between 2011 and 2013, compared with only 39 % of total glacial-earthquake production during 2008–10. Jakobshavn Isbræ alone was responsible for one third of the glacial earthquakes on Greenland's west coast from 2011–13. Despite the increase in glacial-earthquake activity at glaciers along Greenland's northwest coast, the seismic events remain confined to glaciers south of 78° N. We expect this geographical limitation to persist as long as the large glaciers along Greenland's north and northeast coast drain into floating ice tongues or ice shelves, which do not produce glacial earthquakes.

The expanded glacial-earthquake catalog we produce allows us to explore individual glacier behavior in detail. We identify changes in calving behavior at several glaciers and provide high-precision timing constraints on those changes. The presence

of a glacial earthquake establishes the glacier's grounded state, as these seismic events occur only when a glacier's terminus is near its grounding line. At Kangerdlugssuaq Glacier we use earthquake data to document the transition from a near-grounded terminus to a floating ice tongue in 2013. Glacial earthquakes also provide detailed information about the geometry and region of the calving front active during a calving event. Sequences of glacial earthquakes can track the timing of progressive failure across a single calving front, as we document at Kong Oscar Glacier, and the evolution of calving-front orientations, as we document at Helheim and Alison Glaciers. The seasonality of glacial earthquakes is linked to seasonal ice-front advance and retreat, including modulation by the strength of ice mélange in the proglacial fjord. At Jakobshavn Isbræ, the number of glacial earthquakes dramatically increased in 2013, following several years of unusually warm sea surface temperatures and inferred weak mélange conditions in the fjord.

Large calving events continue to contribute significantly to mass loss of the Greenland ice sheet. Glacial earthquakes are an increasingly effective remote-observation tool for understanding dynamic processes and ice-ocean interactions at glacier margins. Continued documentation and analysis of these events will be a valuable addition to our understanding of the behavior of the Greenland Ice Sheet, as will future work to understand better the physics of the glacial-earthquake source.

1.6 Acknowledgements

This work was supported by NSF grants EAR–1249167 and ARC–1304346 and an NSF Graduate Research Fellowship to K. Olsen. We acknowledge the use of seismic data from the IRIS–USGS Global Seismographic Network, GEOSCOPE, GEOFON, MedNet, and the Greenland Ice Sheet Monitoring Network, retrieved from the archive at the IRIS DMC. We thank S. Bevan and A. Luckman for providing terminus-position

data for Helheim Glacier. Comments from two anonymous reviewers and Scientific Editor H. Fricker improved the manuscript.

Table 1: Centroid–single-force solutions for 139 earthquakes in this study. Columns give event number; centroid time with standard error; centroid time shift from detection time (δt_0); centroid latitude with standard error (error of .00 means error is smaller than two decimal places); shift in latitude from detection location ($\delta\lambda_0$); centroid longitude with standard error (error of .00 means error is smaller than two decimal places); shift in longitude from detection location ($\delta\phi_0$); scaling exponent for CSF amplitude and vector; CSF amplitude M_{CSF}, in units of kg m, to be scaled by exponent given in the previous column (for event 1, M_{CSF} = 3.3 x 10^{13} kg m); CSF vector in geographic coordinates r, θ, ϕ (up, south, east), with standard errors, to be scaled by the Scale Factor; plunge of CSF vector with respect to horizontal; azimuth of CSF vector with respect to north; and source glacier. Source glacier identifiers are consistent with Veitch and Nettles (2012) with the addition of glacier 9: 1: Kangerdlugssuaq Glacier; 2: Helheim Glacier; 3: Southeast Greenland; 4a: Tracy Glacier; 4b: Kong Oscar Glacier; 4c: Sverdrup Glacier; 4d: Hayes Glacier; 4e: Alison Glacier; 5a: Giesecke Bræer; 5b: Upernavik Isstrøm; 6: Rink Isbræ; 7: Jakobshavn Isbræ; 9: Sermeq Silardleq. Circles beside event numbers denote NRT detections. ⋆ denotes a poorer-quality standard detection.

No.	Centroid Parameters											Scale Factor	M	CSF Vector					
	Date			Time			Latitude		Longitude										
	Y	M	D	h	m	sec	δt_0	λ	$\delta\lambda_0$	ϕ	$\delta\phi_0$	10^{ex}	CSF	V_r	V_θ	V_ϕ	pl.	azim.	reg.
1	2011	1	2	4	47	59.4±0.5	15.4	71.79±.04	-0.46	-51.57±.09	2.68	13	3.3	0.61±0.22	-2.59±0.16	1.87±0.19	-11	36	6
2	2011	1	5	21	5	31.3±0.3	11.3	68.74±.02	-0.51	-33.18±.04	-0.43	13	6.0	0.53±0.23	-5.91±0.20	-1.11±0.23	-5	349	1
3	2011	1	6	12	16	12.7±0.6	4.7	73.10±.02	-0.15	-54.10±.13	0.65	13	3.1	0.12±0.22	-0.97±0.24	2.92±0.19	-2	72	5b
4	2011	1	14	3	29	11.8±0.5	-32.2	76.11±.04	0.61	-59.51±.10	0.99	13	5.3	1.04±0.37	4.82±0.30	-1.90±0.36	-11	202	4b
5	2011	1	21	8	31	51.4±0.5	-8.6	69.23±.02	-0.27	-49.33±.08	1.17	13	2.3	0.10±0.15	-0.77±0.15	-2.16±0.12	-2	290	7
6	2011	3	24	7	48	18.1±0.4	18.1	76.12±.02	0.37	-59.49±.07	0.76	13	5.0	-0.83±0.22	-4.30±0.21	2.32±0.23	10	28	4b
7	2011	4	1	5	45	26.7±0.5	6.7	73.00±.00	0.00	-54.31±.08	0.69	13	4.3	0.42±0.25	-1.08±0.28	4.19±0.22	-5	76	5b
8	2011	5	26	20	13	28.2±0.6	16.2	73.10±.03	0.35	-54.07±.03	-0.32	13	1.5	0.17±0.09	-1.34±0.10	0.66±0.11	-7	26	5b
○ 9	2011	6	21	14	9	33.9±0.5	5.9	66.44±.03	-0.31	-38.30±.09	-1.55	13	2.3	-0.68±0.17	1.00±0.18	2.01±0.14	17	116	2
10	2011	6	22	15	17	35.4±0.5	31.4	73.02±.01	0.02	-54.60±.13	-5.60	13	3.5	-0.45±0.22	1.72±0.24	-3.03±0.21	7	240	5b
11	2011	6	25	13	17	28.5±0.4	0.5	66.49±.00	-0.01	-38.26±.04	0.24	13	1.7	0.35±0.07	-0.82±0.11	-1.47±0.08	-12	299	2
○ 12	2011	6	26	10	31	34.4±0.5	6.4	69.24±.03	-0.26	-49.64±.02	-0.14	13	1.7	-0.37±0.07	-0.50±0.09	-1.59±0.09	13	287	7
13	2011	6	26	17	53	35.2±0.3	7.2	76.01±.01	-0.24	-59.77±.03	0.48	13	6.2	0.96±0.23	1.17±0.30	6.06±0.21	-9	101	4b
14	2011	6	29	1	50	15.0±0.4	-1.0	74.66±.01	-0.09	-56.22±.01	0.03	13	1.9	0.10±0.07	1.12±0.10	-1.58±0.11	-3	235	4e
15	2011	7	12	21	1	33.4±0.5	13.4	69.24±.04	-0.51	-49.89±.07	2.86	13	5.0	0.10±0.46	-4.96±0.27	0.70±0.42	-1	8	7
○ 16	2011	7	19	14	42	41.8±0.5	-6.2	77.67±.02	0.17	-65.85±.11	0.65	13	2.7	-0.50±0.17	0.34±0.21	-2.63±0.15	11	263	4a
17	2011	7	21	4	25	35.0±0.5	-9.0	72.90±.02	-0.35	-54.47±.08	-0.22	13	6.5	1.56±0.32	-3.23±0.35	5.42±0.34	-14	59	5b
18	2011	7	27	15	14	37.6±0.6	5.6	74.64±.01	0.14	-55.94±.11	-1.44	13	3.3	0.42±0.18	2.61±0.19	1.95±0.22	-7	143	4e
19	2011	8	4	9	5	10.7±0.6	6.7	73.58±.01	0.33	-55.66±.09	-2.41	13	4.2	0.77±0.21	4.08±0.22	0.14±0.25	-11	178	5a
20	2011	8	6	23	10	38.3±0.6	-1.7	71.69±.04	-0.81	-51.84±.16	-0.34	13	2.4	-0.23±0.24	0.73±0.20	-2.27±0.17	6	252	6
21	2011	8	10	7	32	35.2±0.6	11.1	73.07±.02	-0.43	-54.14±.09	2.36	13	4.5	0.57±0.20	-2.72±0.27	3.53±0.26	-7	52	5b
22	2011	8	18	12	32	6.4±0.8	6.4	69.25±.03	0.25	-49.53±.12	1.47	13	2.1	0.56±0.17	1.63±0.18	1.26±0.20	-15	142	7
23	2011	8	26	18	21	5.0±0.7	17.0	76.16±.01	-0.09	-59.80±.13	0.95	13	4.3	-1.95±0.25	-3.78±0.28	0.22±0.33	27	3	4b
24	2011	8	26	18	31	13.3±1.1	-6.7	75.96±.05	-0.79	-59.50±.16	1.25	13	2.7	-0.25±0.24	2.04±0.29	-1.78±0.25	5	221	4b
25	2011	9	14	23	20	47.8±0.5	7.8	70.79±.02	-0.21	-50.73±.08	0.27	13	2.1	0.21±0.12	-0.61±0.11	2.03±0.10	-6	73	9
26	2011	9	19	13	51	51.5±0.5	7.5	68.55±.03	0.55	-32.94±.09	1.06	13	1.5	-0.26±0.10	0.46±0.10	1.45±0.09	10	108	1
○ 27	2011	10	10	16	22	0.3±0.9	-7.7	72.83±.04	-0.67	-54.19±.20	1.31	13	2.4	-0.47±0.21	0.81±0.21	-2.23±0.20	11	250	5b
28	2011	10	21	7	26	45.1±0.6	5.1	75.73±.01	-0.02	-57.96±.07	0.29	13	1.7	-0.26±0.10	0.88±0.13	-1.43±0.11	9	238	4c
29	2011	10	27	9	39	19.4±0.6	-8.6	73.13±.02	-0.12	-54.56±.05	-0.31	13	3.7	0.99±0.21	-0.97±0.25	3.41±0.24	-16	74	5b
30	2011	11	24	2	21	3.8±0.6	-8.2	76.13±.04	0.13	-59.20±.14	2.80	13	4.2	1.17±0.28	3.75±0.26	-1.58±0.29	-16	203	4b
31	2011	11	30	9	58	15.7±0.9	15.7	72.98±.02	-0.27	-54.23±.17	2.52	13	4.4	0.31±0.42	0.34±0.43	4.33±0.35	-4	95	5b
○ 32	2011	12	4	4	1	21.9±0.6	-6.1	66.42±.03	0.17	-38.16±.07	0.59	13	2.1	-0.71±0.13	1.14±0.16	1.66±0.15	19	124	2
○ 33	2011	12	5	7	25	44.0±0.5	8.0	68.73±.03	0.48	-33.45±.09	-0.20	13	2.3	0.17±0.16	0.68±0.14	-2.19±0.11	-4	253	1
○ 34	2011	12	7	22	8	58.8±0.6	2.8	73.54±.02	0.54	-55.21±.14	3.79	13	2.2	-0.40±0.14	-0.91±0.17	-1.91±0.14	11	296	5a
35	2011	12	21	15	40	19.9±0.5	11.9	69.23±.00	-0.02	-49.34±.07	0.41	13	2.6	-0.65±0.16	-0.88±0.18	-2.34±0.15	15	291	7
36	2012	1	3	11	11	41.7±0.7	13.7	73.03±.03	0.28	-54.38±.09	0.37	13	5.0	0.34±0.38	0.08±0.46	4.94±0.37	-4	91	5b
37	2012	1	17	1	54	34.6±0.3	10.6	66.41±.01	-0.34	-38.24±.03	-0.99	13	3.7	1.09±0.11	-1.71±0.14	-3.09±0.12	-17	299	2
38	2012	1	29	11	9	35.9±0.9	-24.1	72.94±.03	0.19	-54.44±.27	4.81	13	2.7	-0.11±0.43	-0.38±0.42	2.70±0.24	2	82	5b
○ 39	2012	2	12	13	44	48.8±0.6	16.8	69.18±.02	0.18	-49.52±.10	-0.52	13	1.4	0.13±0.12	0.25±0.15	1.33±0.10	-6	101	7
40	2012	2	12	16	16	20.4±0.3	-11.6	69.10±.01	-0.15	-49.25±.04	-0.50	13	2.4	0.06±0.08	-1.24±0.09	-2.01±0.08	-1	302	7
41	2012	3	18	18	21	34.5±0.6	-1.5	76.12±.03	0.62	-59.69±.06	-1.19	13	2.7	0.56±0.15	2.32±0.16	-1.34±0.18	-12	210	4b
○ 42	2012	3	31	8	55	40.0±0.3	-4.0	73.04±.01	-0.21	-54.38±.07	0.37	13	2.8	-0.42±0.12	0.56±0.12	-2.74±0.09	9	258	5b
43	2012	4	9	10	11	39.8±0.3	11.8	66.35±.01	0.10	-38.28±.01	-0.03	13	3.5	-1.03±0.09	1.00±0.13	3.20±0.10	17	107	2
44	2012	4	14	1	48	42.1±0.3	-5.9	66.43±.02	0.68	-38.33±.04	-0.08	13	2.5	-0.53±0.10	1.02±0.11	2.18±0.08	12	115	2
45	2012	4	24	4	46	21.6±0.2	-2.4	75.94±.01	0.19	-59.29±.00	-0.04	13	6.1	-0.66±0.16	6.03±0.14	-0.16±0.17	6	182	4b
46	2012	5	3	8	27	54.5±0.5	10.5	73.01±.02	-0.24	-54.45±.07	-0.70	13	2.2	0.65±0.12	-1.06±0.15	1.85±0.13	-17	60	5b
47	2012	6	15	9	16	8.2±0.7	8.2	72.99±.03	-0.76	-54.56±.14	5.69	13	3.3	1.02±0.19	-2.07±0.20	2.37±0.19	-18	49	5b
○ 48	2012	6	26	3	1	57.0±0.5	-11.0	69.33±.01	-0.17	-49.93±.09	-1.43	13	1.3	-0.37±0.09	-0.16±0.08	-1.22±0.08	17	277	7
○ 49	2012	6	30	14	44	18.6±0.6	10.6	73.11±.02	-0.14	-54.30±.11	0.45	13	2.8	-0.06±0.15	1.47±0.16	-2.35±0.15	1	238	5b
○ 50	2012	7	7	20	37	22.3±0.7	-13.7	66.38±.04	-0.37	-38.39±.07	-0.64	13	1.3	-0.31±0.09	1.02±0.10	0.74±0.11	14	144	2

Table 1 (continued)

No.	Centroid Parameters											Scale Factor	M	CSF Vector					
	Date			Time				Latitude		Longitude									
	Y	M	D	h	m	sec	δt_0	λ	$\delta\lambda_0$	ϕ	$\delta\phi_0$	$10^{\rm ex}$	CSF	V_r	V_θ	V_ϕ	pl.	azim.	reg.
51	2012	7	7	20	44	22.8±0.4	6.8	66.39±.02	0.64	-38.21±.02	0.04	13	3.3	1.02±0.12	-1.40±0.18	-2.76±0.13	-18	297	2
52	2012	7	8	20	22	1.9±0.4	9.9	69.15±.03	-0.60	-49.58±.06	0.17	13	2.6	-0.35±0.15	-1.95±0.14	-1.75±0.14	8	318	7
53	2012	7	8	20	46	24.2±0.3	0.2	69.26±.02	0.51	-49.83±.03	0.92	13	2.8	-1.05±0.09	-2.25±0.10	-1.26±0.12	22	331	7
○ 54	2012	7	8	21	5	14.1±0.6	2.1	69.18±.02	-0.57	-49.84±.13	1.41	13	1.5	0.27±0.12	-0.49±0.12	1.35±0.11	-11	70	7
55	2012	7	18	1	27	8.5±0.4	12.5	73.10±.01	-0.15	-55.18±.04	-0.43	13	5.4	1.23±0.22	-2.87±0.25	4.39±0.24	-13	57	5b
56	2012	7	20	18	1	13.6±0.5	-6.4	77.61±.01	0.11	-66.03±.07	0.47	13	1.6	-0.28±0.09	-0.24±0.10	-1.55±0.08	10	279	4a
○ 57	2012	7	25	5	3	31.0±0.5	10.9	66.43±.01	-0.07	-38.68±.08	0.82	13	2.6	0.10±0.17	1.71±0.15	1.97±0.14	-2	131	2
58	2012	7	31	9	30	6.2±0.3	-1.8	76.06±.02	-0.44	-59.23±.07	3.27	13	3.4	0.52±0.11	2.62±0.11	-2.14±0.11	-9	219	4b
○ 59	2012	8	2	23	10	26.6±0.3	2.6	69.17±.02	0.17	-49.42±.07	1.58	13	1.9	-0.06±0.09	-0.95±0.08	-1.68±0.07	2	299	7
60	2012	8	5	0	23	27.9±0.3	15.9	75.91±.02	0.16	-59.58±.02	0.17	13	3.0	-0.51±0.12	2.60±0.11	-1.36±0.14	10	208	4b
61	2012	8	8	0	54	24.6±0.8	8.6	73.14±.03	-0.36	-54.44±.20	1.06	13	2.5	0.12±0.30	-0.88±0.28	2.37±0.17	-3	70	5b
62	2012	8	11	3	27	32.9±0.4	4.9	73.48±.01	0.23	-55.22±.04	-0.47	13	3.3	-0.01±0.13	-0.27±0.16	3.24±0.12	0	85	5a
○ 63	2012	8	11	3	44	32.6±1.0	16.6	73.62±.03	-0.13	-54.94±.19	2.31	13	1.3	0.20±0.12	0.82±0.11	-1.02±0.13	-9	231	5a
○ 64	2012	8	12	16	21	19.7±0.5	-16.3	71.81±.03	0.81	-51.66±.05	-0.66	13	2.0	-0.36±0.10	1.19±0.14	-1.53±0.12	10	232	6
65	2012	8	19	6	32	4.9±0.6	-3.1	73.03±.02	0.28	-54.42±.13	1.33	13	7.3	-1.23±0.58	1.86±0.55	-6.91±0.40	10	255	5b
○ 66	2012	8	23	18	56	44.6±0.4	-3.4	66.40±.01	-0.10	-38.38±.07	1.12	13	1.6	-0.33±0.09	0.94±0.09	1.22±0.08	12	127	2
67	2012	8	23	19	20	12.2±0.2	20.2	66.36±.01	-0.39	-38.29±.03	-1.04	13	5.6	1.40±0.15	-1.45±0.21	-5.27±0.14	-14	285	2
68	2012	8	24	4	1	7.7±0.3	-4.3	77.72±.01	0.22	-66.27±.07	1.23	13	2.4	-0.52±0.09	0.39±0.10	-2.28±0.08	13	260	4a
69	2012	9	2	8	20	17.8±0.3	1.8	69.17±.02	0.42	-49.69±.05	0.56	13	6.8	-1.75±0.27	-4.61±0.24	-4.70±0.25	15	314	7
70	2012	9	7	9	15	28.6±0.3	0.6	69.11±.02	-0.14	-49.59±.05	0.66	13	3.9	-0.37±0.18	-3.62±0.15	-1.51±0.18	5	337	7
○ 71	2012	9	22	14	46	55.0±0.4	-1.0	69.06±.02	0.31	-49.79±.09	-1.04	13	1.9	-0.53±0.12	-1.13±0.12	-1.48±0.11	16	307	7
72	2012	9	24	12	53	23.0±0.5	-5.0	69.19±.01	-0.06	-49.51±.07	0.74	13	2.0	-0.84±0.11	-1.75±0.11	-0.55±0.15	25	342	7
73	2012	9	27	18	29	25.5±0.3	-2.5	66.34±.01	0.09	-38.52±.02	0.23	13	3.3	-0.52±0.08	1.00±0.14	3.06±0.10	9	108	2
74	2012	9	27	23	47	30.5±0.2	2.5	66.40±.01	-0.85	-38.38±.04	-0.13	13	5.6	-0.97±0.17	2.09±0.17	5.11±0.13	10	112	2
○ 75	2012	10	11	19	31	20.8±0.7	-15.2	73.04±.04	2.54	-54.65±.20	0.85	13	6.5	-0.62±0.62	-0.07±0.57	-6.44±0.39	6	271	5b
○ 76	2012	10	26	19	4	54.8±0.5	-9.2	65.27±.03	0.52	-41.00±.05	0.75	13	2.0	-0.59±0.09	1.48±0.11	1.20±0.10	17	141	3
77	2012	11	4	4	9	42.0±0.4	-10.0	74.58±.01	0.08	-56.18±.05	-0.68	13	4.1	-0.78±0.16	-2.56±0.17	-3.13±0.19	11	309	4e
78	2012	11	7	7	15	40.2±0.5	12.2	71.73±.03	-0.52	-51.83±.11	1.42	13	3.2	1.03±0.22	-1.84±0.19	2.41±0.20	-19	53	6
○ 79	2012	11	21	1	53	44.1±0.6	-7.9	77.69±.03	0.44	-65.84±.16	-0.09	13	2.0	-0.27±0.12	-0.09±0.12	-1.97±0.08	8	273	4a
80	2012	11	24	16	6	31.3±0.5	15.3	69.15±.01	-0.10	-49.46±.08	0.79	13	6.2	0.85±0.34	4.15±0.32	4.53±0.32	-8	132	7
81	2012	12	5	16	27	8.1±0.3	4.1	68.57±.01	0.32	-33.16±.05	1.59	13	3.3	0.92±0.11	-2.10±0.15	-2.39±0.13	-16	311	1
82	2012	12	15	2	38	35.8±0.3	11.8	68.70±.02	-0.55	-33.01±.05	1.74	13	2.5	0.66±0.12	-1.76±0.13	-1.69±0.11	-15	316	1
83	2012	12	25	10	21	47.7±0.4	3.7	71.75±.03	-0.50	-51.80±.08	0.45	13	3.1	0.56±0.17	0.09±0.19	3.06±0.14	-10	92	6
84	2013	1	1	10	13	23.7±0.5	3.7	75.02±.03	0.52	-56.55±.13	0.95	13	2.4	0.50±0.16	0.53±0.16	-2.25±0.12	-12	257	4d
85	2013	1	12	9	17	38.5±0.2	10.5	69.10±.01	0.35	-49.32±.00	-0.07	13	7.1	-0.70±0.12	-3.38±0.15	-6.25±0.14	6	298	7
○ 86	2013	1	23	9	53	6.7±0.4	-21.3	74.52±.02	0.27	-55.84±.04	-0.09	13	3.6	0.03±0.18	-2.48±0.19	-2.58±0.20	-1	314	4e
○ 87	2013	2	21	11	13	6.8±0.5	-5.2	71.59±.00	-0.91	-51.64±.08	1.86	13	2.4	-0.95±0.12	1.96±0.12	-0.94±0.14	24	206	6
88	2013	3	4	11	41	29.3±0.2	1.3	66.48±.01	-0.27	-38.41±.02	-0.66	13	6.0	0.89±0.14	-2.26±0.20	-5.49±0.16	-9	292	2
89	2013	3	14	3	47	4.3±0.3	8.3	66.44±.02	0.69	-38.37±.04	0.38	13	2.4	-0.49±0.08	1.15±0.08	2.08±0.07	12	119	2
90	2013	3	29	9	6	1.1±0.3	9.1	69.25±.00	0.00	-49.74±.00	0.01	13	2.9	-0.99±0.08	-1.34±0.10	-2.38±0.10	20	299	7
○ 91	2013	4	3	3	8	1.0±0.4	1.0	73.00±.02	-0.50	-54.49±.12	0.01	13	2.2	-0.34±0.16	0.81±0.15	-2.05±0.11	9	248	5b
92	2013	4	6	2	59	2.5±0.3	14.5	69.13±.02	-0.37	-49.54±.04	0.96	13	4.8	0.20±0.19	4.54±0.16	1.50±0.19	-2	162	7
93	2013	4	8	23	38	34.0±0.4	18.0	77.59±.01	-0.16	-66.27±.09	1.98	13	2.7	-0.76±0.10	0.31±0.11	-2.58±0.09	16	263	4a
○ 94	2013	4	13	11	40	12.6±0.5	12.6	66.40±.04	1.15	-38.10±.06	-1.85	13	1.6	-0.40±0.09	1.43±0.08	0.51±0.09	15	160	2
○ 95	2013	4	27	13	48	35.8±0.3	-4.2	66.32±.01	-0.93	-38.27±.07	-0.52	13	1.7	-0.54±0.09	0.24±0.10	1.58±0.08	19	99	2
96	2013	4	28	7	26	29.5±0.4	5.5	66.46±.01	-0.04	-38.39±.04	0.11	13	1.8	-0.32±0.07	0.89±0.10	1.52±0.09	10	120	2
97	2013	5	23	12	45	46.1±0.2	10.1	69.20±.01	0.20	-49.40±.04	1.60	13	5.4	-0.91±0.15	-2.43±0.15	-4.76±0.15	10	297	7
98	2013	6	14	17	16	30.1±0.3	-17.9	76.06±.02	0.31	-59.67±.07	-1.92	13	4.5	-0.19±0.18	4.06±0.15	-2.00±0.17	2	206	4b
99	2013	6	17	3	49	20.5±0.2	-7.5	69.28±.00	0.03	-49.77±.00	-0.02	13	5.6	-2.23±0.12	-4.37±0.13	-2.79±0.16	23	327	7
100	2013	6	21	6	30	41.4±0.3	1.4	69.11±.02	0.36	-49.59±.02	-0.34	13	2.0	-0.27±0.10	-1.51±0.10	-1.32±0.09	8	319	7

Table 1 (continued)

No.	Centroid Parameters											Scale Factor	M	CSF Vector					
	Date			Time				Latitude		Longitude									
	Y	M	D	h	m	sec	δt_0	λ	$\delta\lambda_0$	ϕ	$\delta\phi_0$	10^{ex}	CSF	V_r	V_θ	V_ϕ	pl.	azim.	reg.
101	2013	6	23	14	35	11.5±0.3	7.5	66.40±.01	0.15	-38.40±.01	-0.15	13	5.9	-0.99±0.17	2.51±0.22	5.24±0.18	10	116	2
○ 102	2013	6	24	17	49	53.6±0.3	-6.4	69.17±.02	0.42	-49.47±.03	0.78	13	1.9	-0.46±0.06	-0.60±0.07	-1.71±0.06	14	289	7
103	2013	6	27	20	11	41.2±0.2	5.2	69.15±.01	0.40	-49.52±.03	0.23	13	5.6	-0.83±0.14	-4.34±0.14	-3.39±0.15	9	322	7
104	2013	7	1	2	2	34.3±0.2	-5.7	76.08±.02	0.58	-59.49±.03	0.01	13	5.6	-1.03±0.15	-5.53±0.14	0.17±0.16	11	2	4b
105	2013	7	1	4	5	38.8±0.4	10.8	69.09±.03	-0.41	-49.29±.03	0.21	13	2.9	0.11±0.14	1.57±0.13	2.43±0.13	-2	123	7
106	2013	7	3	8	19	28.3±0.2	-7.7	69.09±.01	-0.16	-49.11±.02	-0.36	13	4.8	-0.26±0.11	-1.07±0.17	-4.67±0.13	3	283	7
○ 107	2013	7	4	2	9	37.6±0.4	9.6	69.14±.03	-0.36	-49.51±.07	-1.01	13	1.9	0.18±0.12	1.39±0.09	1.25±0.11	-5	138	7
108	2013	7	16	23	41	14.2±0.2	-5.8	69.30±.00	0.30	-49.62±.03	1.38	14	1.1	-0.28±0.02	-0.79±0.02	-0.67±0.02	15	320	7
109	2013	7	25	3	13	47.5±0.2	11.5	66.49±.00	-0.01	-38.42±.01	0.08	13	2.4	0.41±0.06	-1.18±0.09	-2.05±0.07	-10	300	2
110	2013	7	25	12	56	33.7±0.2	1.7	66.48±.00	-0.02	-38.31±.02	0.19	13	3.8	-0.94±0.08	1.94±0.12	3.10±0.11	14	122	2
111	2013	7	30	20	1	23.1±0.2	-4.9	66.43±.01	0.18	-38.36±.01	-0.11	13	3.4	-0.71±0.08	1.50±0.12	2.91±0.09	12	117	2
112	2013	7	31	14	59	39.5±0.4	11.5	65.22±.02	-0.28	-41.18±.07	0.32	13	1.7	0.19±0.10	-0.65±0.10	-1.58±0.08	-6	292	3
113	2013	7	31	19	21	18.5±0.3	6.6	66.34±.02	-0.41	-38.29±.05	0.46	13	1.8	0.49±0.07	-0.54±0.10	-1.60±0.07	-16	289	2
114	2013	8	4	22	5	29.2±0.4	17.2	70.94±.01	-0.06	-50.46±.05	0.54	13	2.8	-0.04±0.11	-0.63±0.13	2.73±0.12	1	77	9
115	2013	8	4	23	0	52.3±0.3	4.3	73.04±.02	1.54	-54.43±.06	4.07	13	6.0	-0.38±0.25	2.23±0.25	-5.52±0.19	4	248	5b
○ 116	2013	8	8	6	50	6.8±0.5	14.8	66.44±.03	0.94	-38.86±.03	-0.36	13	1.7	-0.28±0.09	-0.78±0.12	-1.53±0.10	9	297	2
○ 117	2013	8	9	15	17	14.1±0.3	18.1	69.13±.02	-0.12	-49.40±.03	-0.15	13	2.1	0.35±0.10	1.68±0.10	1.14±0.11	-10	146	7
118	2013	8	11	11	25	59.0±0.3	-1.0	69.24±.00	-0.01	-49.44±.04	-0.69	13	5.4	-0.53±0.18	-5.08±0.19	-1.64±0.27	6	342	7
119	2013	8	11	11	49	40.4±0.3	-3.6	69.06±.00	0.06	-49.56±.04	-0.56	13	3.1	-0.80±0.09	-0.60±0.12	-2.95±0.11	15	282	7
120	2013	8	14	23	41	28.1±0.2	-7.9	66.44±.01	-0.81	-38.34±.04	-0.59	13	3.1	-0.73±0.09	1.46±0.09	2.68±0.08	13	119	2
○ 121	2013	8	14	23	50	53.9±0.3	21.9	66.39±.02	0.64	-38.34±.04	0.41	13	1.8	0.28±0.07	-1.12±0.07	-1.43±0.06	-9	308	2
122	2013	8	19	12	17	1.0±0.3	5.0	73.01±.00	0.01	-54.27±.05	0.73	13	5.9	0.07±0.22	-2.10±0.29	5.50±0.18	-1	69	5b
123	2013	8	24	7	25	59.0±0.3	7.0	74.95±.00	-0.05	-57.09±.01	-0.09	13	5.4	0.09±0.16	-4.49±0.20	3.03±0.26	-1	34	4d
124	2013	9	9	8	59	56.2±0.3	-3.8	69.15±.02	-1.35	-49.57±.04	-1.07	13	4.6	0.69±0.17	3.93±0.15	2.31±0.16	-9	150	7
125	2013	9	10	18	59	42.5±0.5	14.4	69.25±.03	0.00	-49.44±.08	-1.69	13	3.4	-0.72±0.21	-2.90±0.18	-1.52±0.22	12	332	7
126	2013	9	11	3	4	23.1±0.3	7.1	69.36±.01	1.36	-49.84±.05	0.16	13	7.3	-2.88±0.26	-1.48±0.24	-6.49±0.26	23	283	7
127	2013	9	15	14	8	48.0±0.6	16.0	73.09±.03	-1.91	-54.07±.17	-5.07	13	4.9	0.04±0.45	-0.12±0.43	4.93±0.29	0	89	5b
128	2013	9	19	10	34	54.5±0.3	14.6	74.72±.02	0.22	-56.42±.07	-0.92	13	3.5	0.75±0.13	1.23±0.15	3.17±0.14	-12	111	4e
129	2013	9	29	14	37	14.1±0.7	2.1	75.95±.03	0.20	-59.84±.15	2.41	13	2.2	-0.72±0.14	1.93±0.14	-0.79±0.14	19	202	4b
130	2013	10	3	3	35	6.5±0.4	2.5	75.89±.02	0.14	-59.57±.02	0.18	13	4.2	-0.60±0.19	4.08±0.19	0.49±0.24	8	173	4b
131	2013	10	5	23	29	9.2±0.2	13.2	76.13±.01	-0.12	-59.58±.05	0.17	13	6.2	-0.40±0.20	-2.95±0.24	5.47±0.17	4	62	4b
○ 132	2013	10	7	18	16	27.7±0.4	19.7	75.99±.02	0.49	-59.62±.09	2.88	13	2.8	-0.04±0.13	2.67±0.13	0.84±0.15	1	162	4b
133	2013	10	14	2	3	37.4±0.6	9.4	72.98±.04	0.98	-54.06±.16	-0.06	13	3.3	-0.49±0.33	-1.20±0.27	3.02±0.22	9	68	5b
○ 134	2013	11	7	11	2	20.7±0.5	20.7	72.99±.01	-0.01	-53.78±.11	1.22	13	2.9	-0.49±0.18	-0.99±0.20	2.69±0.16	10	70	5b
○ 135	2013	11	22	7	26	15.6±0.4	-0.4	69.20±.01	-0.05	-49.77±.01	-0.02	13	3.0	-0.78±0.11	-0.94±0.15	-2.71±0.13	15	289	7
136	2013	11	23	22	11	14.1±0.4	-5.9	74.99±.03	0.24	-56.70±.07	0.55	13	2.6	0.25±0.15	1.84±0.14	-1.80±0.14	-6	224	4d
137	2013	12	5	9	54	28.2±0.3	12.2	69.12±.02	0.37	-49.53±.04	0.22	13	3.3	-0.48±0.16	-3.08±0.15	-1.18±0.16	8	339	7
⋆ 138	2013	12	10	3	38	13.1±0.4	29.1	73.01±.02	-0.24	-54.48±.02	0.27	13	4.6	0.44±0.18	-1.05±0.28	4.41±0.21	-5	77	5b
139	2013	12	27	10	4	17.1±0.3	1.1	75.96±.02	0.46	-59.58±.07	4.92	13	6.3	0.52±0.27	-6.13±0.20	-1.48±0.25	-5	346	4b

Table 2: Detection parameters for the six earthquakes for which we were unable to obtain robust CSF solutions. Columns give detection time; detection location; and source glacier (where known). Source glacier identifiers are as in Table 1: 4a: Tracy Glacier; 5b: Upernavik Isstrøm. The four events listed without source glaciers have detection locations along Greenland's southeast coast. Circles denote NRT detections.

	Y	M	D	h	m	sec	Lat	Lon	reg.
	2011	3	8	6	52	48.0	65.75	-40.25	
○	2011	7	21	4	43	36.0	72.75	-55.25	5b
○	2011	12	28	16	16	32.0	62.25	-39.75	
	2012	1	20	4	37	20.0	65.50	-39.50	
○	2013	8	6	17	39	28.0	77.50	-67.50	4a
○	2013	11	24	4	41	28.0	65.00	-37.00	

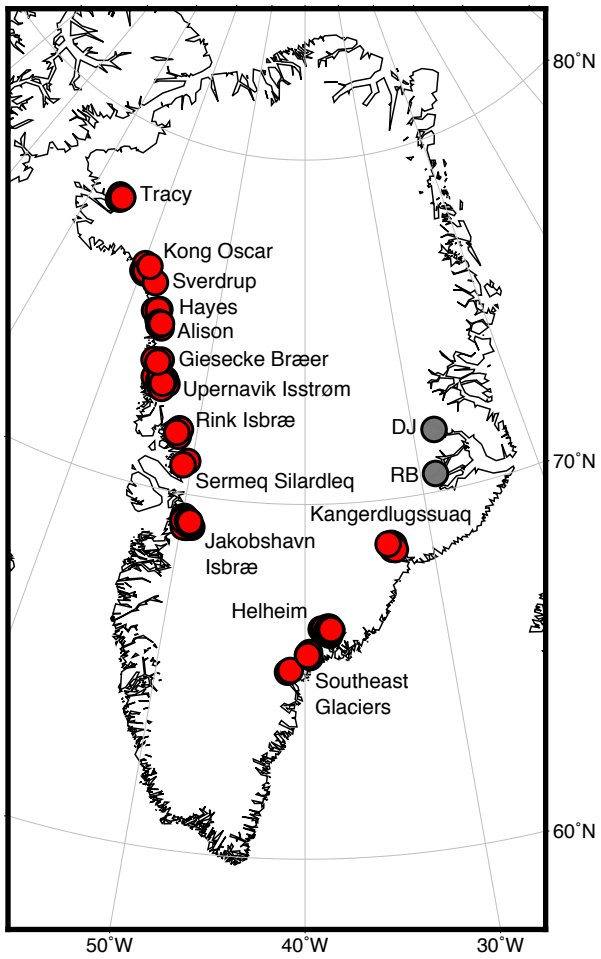

Figure 1.1: Map showing locations of glacial earthquakes in Greenland between 2011 and 2013 (red dots). Grey dots show locations of two glaciers that previously produced glacial earthquakes (Tsai and Ekström, 2007; Veitch and Nettles, 2012) but did not produce events in 2011–13: Daugaard-Jensen Glacier (DJ) and Rolige Bræ (RB).

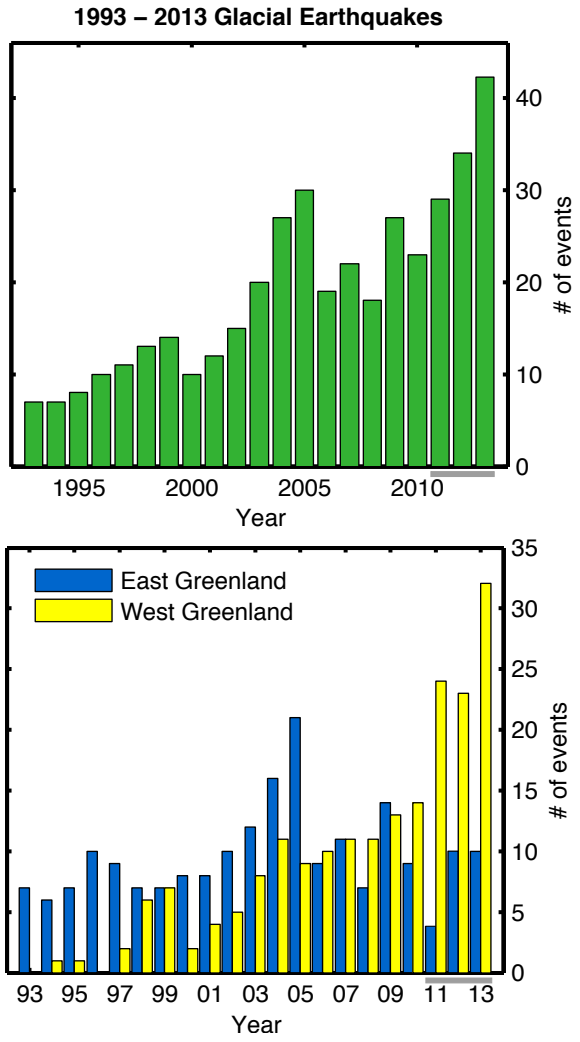

Figure 1.2: Glacial-earthquake occurrence in Greenland, 1993–2013. Top: Number of glacial earthquakes detected annually. Bottom: Annual earthquake detections by region. Grey bars identify the three years of new data analyzed in this study.

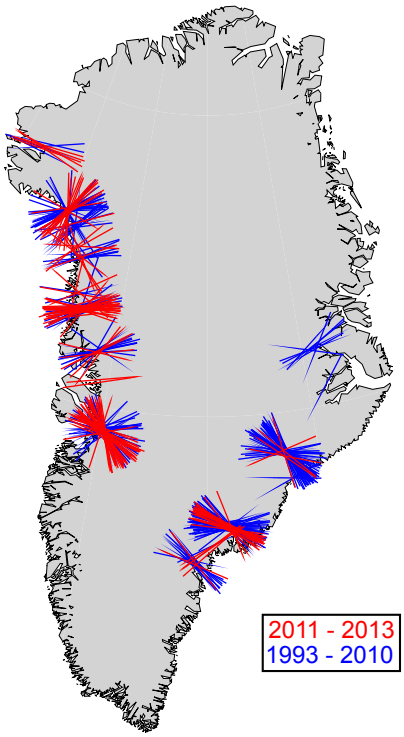

Figure 1.3: Glacial-earthquake force azimuths for the complete catalog, 1993–2013. Red sticks show events from this study, and blue sticks show published solutions from Tsai and Ekström (2007) and Veitch and Nettles (2012). Names of glaciers are given in Fig. 1.

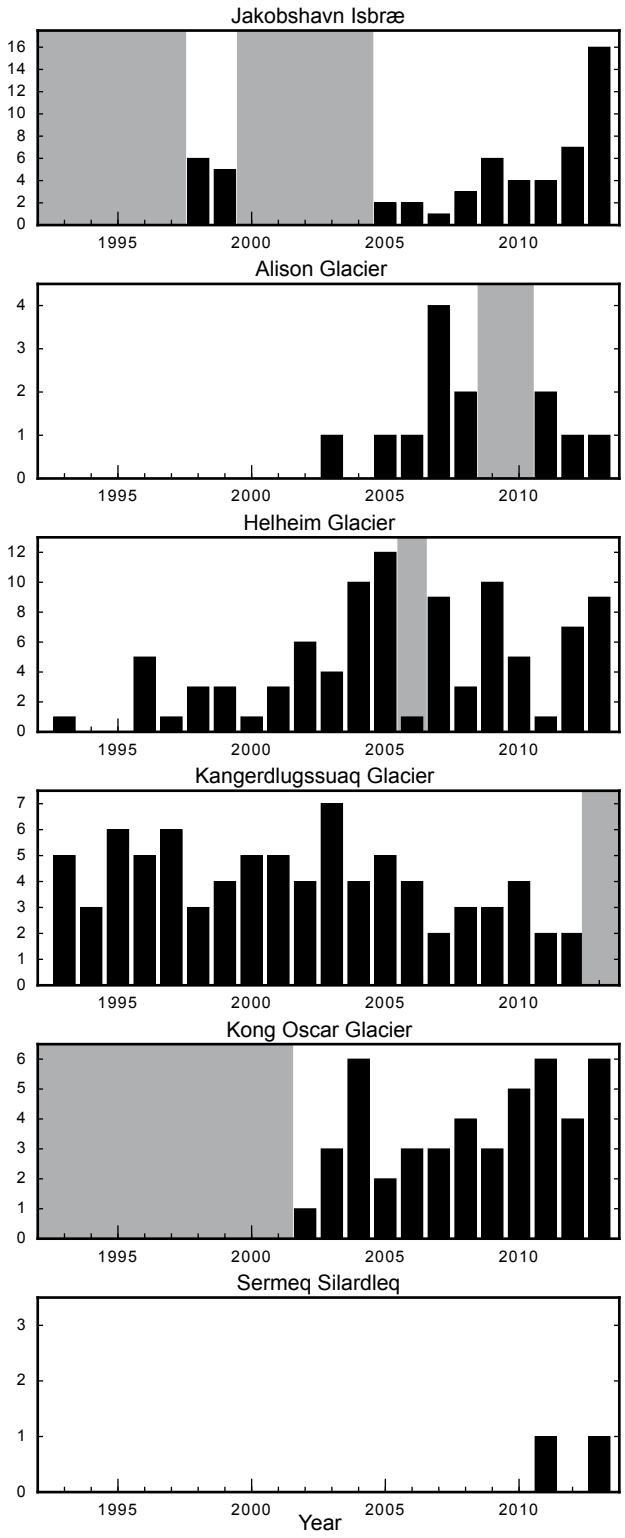

Figure 1.4: Number of glacial earthquakes detected at the six glaciers discussed in detail in the text. Grey shading identifies years when a glacier is known to have maintained a floating ice tongue. In 2006, Helheim Glacier maintained a floating ice tongue for most of the year and its single glacial earthquake occurred on 23 August 2006. Floating condition is unknown for years shown with neither glacial earthquake counts nor grey shading.

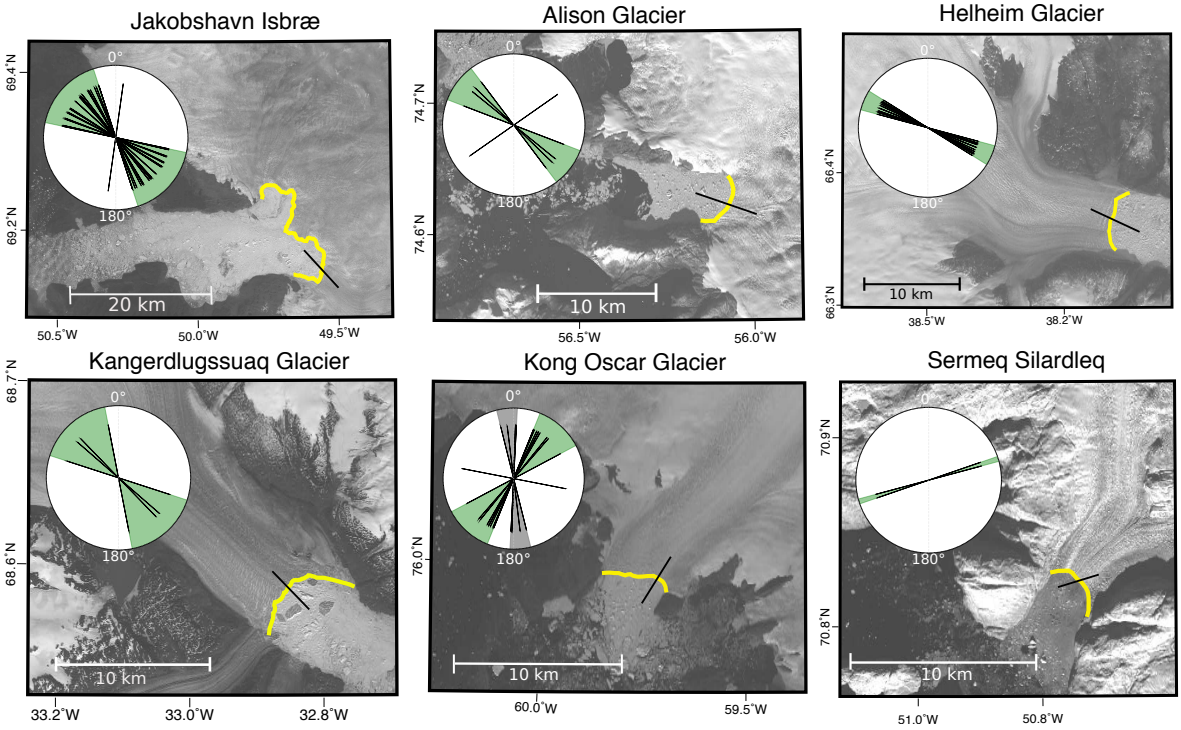

Figure 1.5: Geometry of calving fronts and glacial-earthquake force azimuths for the six glaciers discussed in detail in the text. Yellow lines show glacier terminus positions digitized from background Landsat images, all from 2015. Circular inset shows force azimuths for glacial earthquakes at each glacier from 2011–13. Black stick placed on each calving front represents the mean azimuth of the events at each glacier that fall within the green shading. A detailed plot of variation in azimuth at Alison Glacier is shown in Fig. 6. The variation in azimuths at Kong Oscar Glacier is discussed in the text and a subset of events is shown in more detail in Fig. 8.

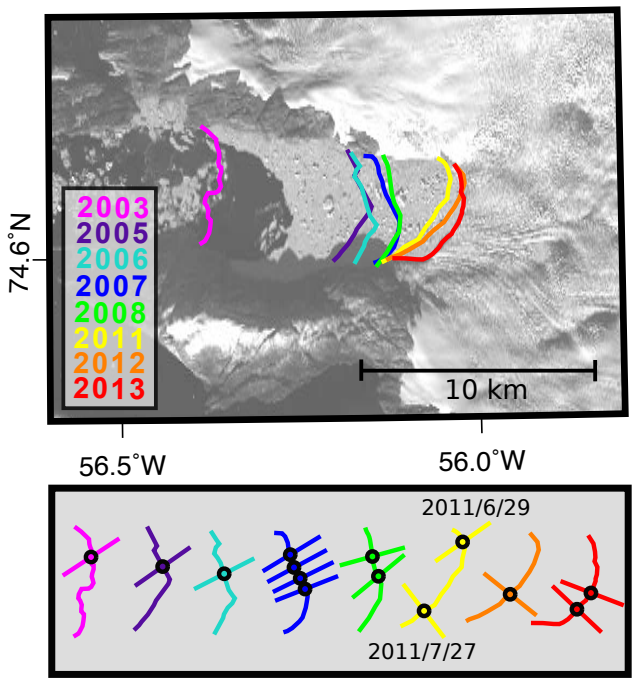

Figure 1.6: Calving-front locations and glacial-earthquake force azimuths at Alison Glacier. Top: Colored calving fronts show summer terminus positions digitized from Landsat images during years when glacial earthquakes occurred. Background image is from 1 October 2013. Bottom: Colored lines show calving fronts as in top figure, but with an arbitrary separation in the horizontal direction. Colored sticks show the force azimuths of glacial earthquakes. Force azimuths are plotted on the calving front at the location where they are most nearly perpendicular to the calving front. Dates are given for the two events that occurred in the summer of 2011.

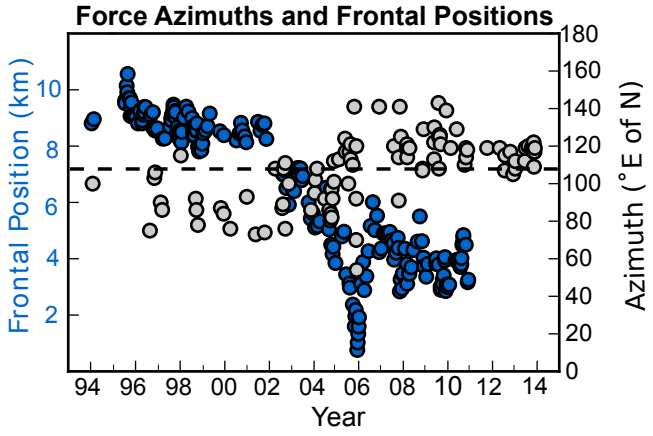

Figure 1.7: Force azimuths and terminus positions at Helheim Glacier. Grey dots show force azimuths for all glacial earthquakes at Helheim Glacier, 1993–2013. Dashed line shows mean force azimuth. Blue dots show terminus position, from Bevan and others (2012). Inspection of Landsat images shows that terminus positions remained within the 2008–10 range during 2011–13.

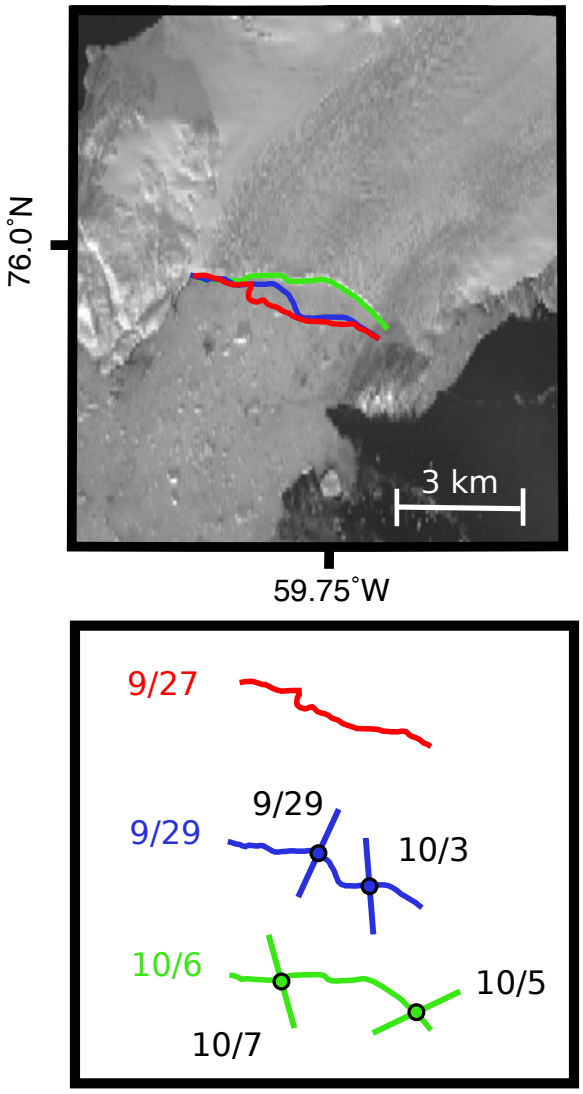

Figure 1.8: Force azimuths at Kong Oscar Glacier. Top: Colored calving fronts show terminus positions digitized from Landsat images in September and October, 2013; colors are as in bottom figure. Background image is from 6 October 2013. Bottom: Colored lines show the calving fronts as in top figure, but with an arbitrary separation in the vertical direction; dates at left give time of image. Colored sticks show glacial-earthquake force azimuths, plotted on the calving front at the location where they are most nearly perpendicular to the calving front. The normal to the 27 September 2013 front is approximately 30°. Dates of each earthquake in 2013 are given in black.

Chapter 2

Constraints on Terminus Dynamics at Greenland Glaciers From Small Glacial Earthquakes

This chapter has been previously published as:

Olsen, K. G., and M. Nettles (2019), Constraints on Terminus Dynamics at Greenland Glaciers From Small Glacial Earthquakes, *Journal of Geophysical Research: Earth Surface*, *7*(124), 1899–1918, 10.1029/2019JF005054.

Abstract

Many large calving events at Greenland's marine-terminating glaciers generate globally detectable glacial earthquakes. We perform a cross-correlation analysis using regional seismic data to identify events below the teleseismic detection threshold, focusing on the 24 hours surrounding known glacial earthquakes at Greenland's three largest glaciers. We detect additional seismic events in the minutes prior to more than half of the glacial earthquakes we study, and following one third of them. Waveform modeling shows source mechanisms like those of previously known glacial earthquakes, a result consistent with available imagery. The seismic events thus do not represent a failure of the high subaerial ice cliff like that expected to trigger large-scale calving and a marine ice-cliff instability; but rather, rotational, buoyancy-driven calving events, likely of the full glacier thickness. A limited investigation of the prevalence of smaller seismic events at times

outside glacial-earthquake windows identifies several additional events. However, we find that calving at the three glaciers we study — Jakobshavn Isbræ, Helheim Glacier, and Kangerdlugssuaq Glacier — often occurs as sequences of discrete buoyancy-driven events in which multiple icebergs ranging in size over as much as three orders of magnitude are all lost within ∼30 minutes. We demonstrate a correlation between glacial-earthquake magnitude and iceberg size for events with well-constrained iceberg-area estimates. Our results suggest that at least 10-30% more dynamic mass loss occurs through buoyancy-driven calving at Greenland's glaciers than previously appreciated.

2.1 Introduction

Iceberg calving plays an important role in glacier evolution in Greenland and Antarctica, both because of the large volumes of ice discharged, and because of significant ice-velocity increases that accompany calving events at marine-terminating glaciers (Amundson et al., 2008; Nettles et al., 2008; Rosenau et al., 2013). However, many aspects of the calving process remain poorly understood. This lack of understanding leads to simplified treatment of calving in ice-sheet models, and an acknowledgment of the clear need for more observational constraints on the details of the calving process (e.g., Nick et al., 2010; Benn et al., 2017).

Many of the largest icebergs calved from near-grounded tidewater glaciers in Greenland are lost through buoyancy-driven calving (Murray et al., 2015c), which generates globally detectable, M_{SW} ∼5 glacial earthquakes (Ekström et al., 2003; Nettles and Ekström, 2010). Buoyancy-driven calving occurs when the tongue of a glacier is driven below floatation as it enters fjord waters. Buoyancy forces act to resolve the isostatic disequilibrium by deflecting the glacier terminus upwards in the water column. This promotes basal crevassing upstream from the terminus and applies a torque to the por-

tion of the glacier downstream of the basal-crevasse location (James et al., 2014; Murray et al., 2015c). When the calving front is near the grounding line, crevasse propagation leads to detachment of a narrow, unstable iceberg that subsequently capsizes against the glacier terminus. During capsize, the newly formed iceberg accelerates away from the glacier, exerting a force on the glacier calving face and the solid Earth. This force is recorded as a glacial earthquake (Nettles and Ekström, 2010; Murray et al., 2015a).

Study of glacial earthquakes has informed our understanding of many aspects of the calving process, including placing constraints on the grounding state of a glacier (Veitch and Nettles, 2012; Olsen and Nettles, 2017), the forces acting on the glacier during calving (Murray et al., 2015a), and the observation that, at times, multiple icebergs are lost from a glacier in rapid succession (e.g., Amundson et al., 2010; Walter et al., 2012; Olsen and Nettles, 2017). Visual documentation of calving events is generally poor, owing to a lack of permanent camera installations at glacier termini, frequent low-visibility conditions, and winter darkness. Seismic data offer a continuous, year-round record of activity, making seismic observations a valuable complement to satellite and ground-based imagery. Seismic observation of large-scale calving processes at Greenland's glaciers has relied mostly on teleseismic recordings from the Global Seismographic Network (GSN). Glacial-earthquake events are identified using these data and a surface-wave detection algorithm developed by Ekström (2006), and analysis of glacial-earthquake source characteristics has, until recently, also been performed using primarily the GSN data (Tsai and Ekström, 2007; Veitch and Nettles, 2012). The Greenland Ice Sheet Monitoring Network (GLISN; Clinton et al., 2014) now provides regional broadband seismic coverage, allowing more detailed investigation of the earthquake source (Walter et al., 2013; Olsen and Nettles, 2017; Sergeant et al., 2018).

Although the buoyancy-driven calving mechanism appears to be responsible for many of the calving events at Greenland's tidewater glaciers (Murray et al., 2015c), the

volume of ice lost in each event is poorly known. Seismic observations are consistent in order of magnitude with icebergs of $\sim$1 km^3 ($\sim$1 Gt) accelerating away from the glacier terminus during capsize (Nettles and Ekström, 2010). Direct observations of individual calving events generating glacial earthquakes at Jakobshavn Isbræ and Helheim Glacier have yielded iceberg-volume estimates between 0.32 km^3 and 1.2 km^3 (Amundson et al., 2008; Walter et al., 2012; James et al., 2014; Murray et al., 2015a). In recent years, 30–50 glacial earthquakes have been detected in Greenland annually (Olsen and Nettles, 2017), suggesting that roughly 25–50 Gt of Greenland's annual dynamic ice loss may be through buoyancy-driven calving events; Sergeant et al. (2019) calculate a similar annual discharge rate (15-50 Gt). However, the size distribution of icebergs lost through buoyancy-driven calving is not known, hindering assessment of the importance of this calving mechanism within the total calving budget.

The true distribution of glacial-earthquake magnitudes is also poorly known. The observed magnitude distribution for some glaciers shows a peak well above the detection threshold, but at others is peaked near that threshold, suggesting that some events are missed by teleseismic approaches (Nettles and Ekström, 2010). Glacial earthquakes smaller than those detected by the automated glacial-earthquake detection algorithm (Ekström, 2006) have been observed previously (Nettles et al., 2008; Walter et al., 2012; Murray et al., 2015c), but no systematic study of these events has been undertaken.

Similarly, the relationship between glacial-earthquake size and iceberg size is not well known, and the lower size limit of icebergs susceptible to buoyancy-driven calving remains an open question. Questions also persist about glacier behavior in the run-up to calving of gigaton-sized icebergs, and whether a triggering mechanism precedes calving. The yield strength of ice is likely to dictate a maximum height for subaerial ice cliffs at glacier termini, above which height ($\sim$100 m) brittle failure will occur (Bassis and Walker, 2012; Ma et al., 2017). Such failure could take the form of ice slumping down

the calving face, which would promote buoyancy-driven calving by further pushing the submerged ice at the calving front out of isostatic equilibrium. This hypothetical ice-slump mechanism would expand the range of glacial conditions where buoyancy-driven calving occurs, perhaps even to include grounded ice. When maximum cliff heights are included in numerical models of Antarctic ice-sheet evolution, ice-sheet collapse is accelerated (Pollard et al., 2015; DeConto and Pollard, 2016). However, few 100-m tall ice cliffs exist at either pole, and large ice slumps are not routinely observed.

In this study, we investigate iceberg calving at Greenland's three largest glaciers: Jakobshavn Isbræ, Helheim Glacier, and Kangerdlugssuaq Glacier, all of which have high ice cliffs; those at Jakobshavn Isbræ and Helheim Glacier are reported to be among the tallest in the world (DeConto and Pollard, 2016). These are also the three most productive glacial-earthquake-generating glaciers in Greenland; together, they have produced the majority of glacial earthquakes recorded since the beginning of the observational catalog in 1993. In 2009, 2010, and 2011, permanent seismic stations were installed within 100 km of each of these three glacier termini as part of the GLISN network. Using local and regional data, we explore evidence for buoyancy-driven calving of smaller icebergs than previously studied, and investigate seismic indications of ice-cliff failure. We then combine our seismological results with evidence from ground-based imagery to reassess the relationship between iceberg size and glacial-earthquake magnitude.

2.2 Data

We focus our analysis on data recorded by the GLISN stations closest to three glaciers: station ILULI, deployed in 2009 and located 62 km from Jakobshavn Isbræ; station ANGG, deployed in 2010 and located 84 km from Helheim Glacier; and station SOEG, deployed in 2011 and located 70 km from Kangerdlugssuaq Glacier (Figure 2.1). We

treat data from temporary station SOE (Dahl-Jensen et al., 2003), which operated from 2000–2002 in the location of the future SOEG station, in the same manner as data from SOEG. We also consider data recorded on as many as ten additional seismic stations located at distances up to 600 km from each glacier terminus (Figure 2.1). Whenever possible, we include data from short-term temporary seismic networks operated near the glaciers of interest, as well as from more distant stations of the GSN.

Jakobshavn Isbræ, Helheim Glacier, and Kangerdlugssuaq Glacier have all been observed to generate multiple glacial earthquakes over the course of a single day (Tsai and Ekström, 2007; Veitch and Nettles, 2012; Olsen and Nettles, 2017), and successive icebergs lost from adjacent portions of a calving terminus have been documented at glaciers around Greenland (Amundson et al., 2008; Walter et al., 2012; Murray et al., 2015c; Olsen and Nettles, 2017), suggesting that the hours surrounding known glacial earthquakes may be a good target for the identification of additional events. Further, any precursory ice slump or other trigger for iceberg calving is likely to occur within the hours prior to calving. We therefore focus our study on the 24 hours of seismic data surrounding known glacial earthquakes to maximize the chance of identifying small seismic events and to assess the possible role of precursory events preceding glacial earthquakes.

We use the published catalog of glacial earthquakes (Tsai and Ekström, 2007; Veitch and Nettles, 2012; Olsen and Nettles, 2017), which includes events occurring between 1993 and 2013, to identify time periods of interest. We consider data recorded from the time of GLISN station deployment at each glacier through the end of 2013, as well as data recorded by station SOE during 2000–2002. These constraints lead to a dataset of 84 glacial earthquakes generated by the three glaciers and recorded by the GLISN station closest to each glacier. During two of these events, noise levels at the nearest station were high enough to obscure the glacial-earthquake signal,

preventing analysis of any smaller signals. We exclude these two events and analyze seismograms for the 12 hours preceding and following the remaining 82 earthquakes: 46 at Jakobshavn Isbræ, 25 at Helheim Glacier, and 11 at Kangerdlugssuaq Glacier.

2.3 Methods

We deconvolve the broadband seismic data to velocity and filter it to 35–100 s, an intermediate-period band similar to that used glacial-earthquake analysis (Tsai and Ekström, 2007; Veitch and Nettles, 2012; Olsen and Nettles, 2017), and selected because it contains the majority of the glacial-earthquake signal. We apply a cross-correlation technique to the vertical-component data to identify previously unknown, small seismic signals associated with glacial earthquakes. For each glacier, we select a template event to use in the cross-correlation analysis. At Jakobshavn Isbræ, we use a signal described in previous studies (Walter et al., 2012; Sergeant et al., 2016) that occurred on 21 August 2009 five minutes before a large calving event that generated a glacial earthquake. This small seismic signal has a peak amplitude approximately 25% that of the following glacial earthquake. High-frame-rate imagery from the glacier terminus (Walter et al., 2012) shows this small seismic signal to coincide with a loss of ice significantly smaller than that associated with the subsequent glacial earthquake. No such well-documented small ice-loss events are known at Helheim or Kangerdlugssuaq Glaciers. At those glaciers, we perform an initial visual inspection of the data, and select a template event recorded at the nearest station (ANGG, SOEG, or SOE). The template waveforms have durations of 72–84 s.

We cross correlate 12-hour-long seismograms preceding the glacial-earthquake events in our catalog with the small template signals recorded at the same station. We then visually review all sections of record that have cross-correlation coefficients with absolute values ≥ 0.85 and discard sections with extremely low amplitude. We inspect

record sections for each small event identified, considering seismic stations to distances of 600 km. We require each small event to be identifiable on two or more stations and to show a moveout across the stations consistent with expected Rayleigh wave group velocities; we compare our observations with speeds of ∼3.6 km/s observed 35-s Rayleigh waves in Greenland (Darbyshire et al., 2017). We perform a similar analysis on hour-long seismograms following each glacial earthquake in our dataset. For a subset of events, we extend the cross-correlation analysis to the full 12 hours following the glacial earthquakes.

In addition, we visually inspect record sections for the 15 minutes before and the 15 minutes after each of the 82 glacial earthquakes in the dataset in an attempt to identify any signals with a likely origin at the glacier that may be missed by the correlation detector. We require any small event identified using this method to be visible on two or more seismic stations within 600 km of the glacier front.

We model the best-recorded small seismic events using a centroid-single-force (CSF) technique like that used in analysis of mass movements such as landslides and glacial earthquakes (Kawakatsu, 1989; Ekström et al., 2003). This allows us to estimate source parameters for each event, including the orientation and amplitude of the force acting at the source, as well as a centroid-single-force magnitude value, M_{CSF}, derived by twice integrating the force history. We follow the modeling approach described by Olsen and Nettles (2017), including specifying the shape and duration of the force-time function as well as specifying the depth of each event. As in Olsen and Nettles (2017) and previous studies (Tsai and Ekström, 2007; Veitch and Nettles, 2012), we use a boxcar-shaped time function with a total duration of 50 s. For each small event we model, we fix the location to the published location of the associated glacial earthquake and deconvolve the seismograms to ground displacement. We analyze data within the period bands 40–100 s or 35–75 s and, when necessary due to the small amplitude of

the signal, within the period band 25–75 s.

We also investigate data from the 24 hours surrounding all glacial earthquakes in our dataset using a range of filters above 1 Hz, and find the most visually coherent high-frequency signal in the range 3–10 Hz (Figure 2.2). We measure the duration of high-frequency energy surrounding each glacial earthquake by hand, picking the onset of high-frequency energy and its end time based on the observed deviation from background noise levels.

2.4 Results

We identify 80 new intermediate-period seismic events associated with the glacial earthquakes we study. These seismic events precede 52% of the glacial earthquakes and follow 37%. In total, we find one or more small event temporally associated with 66% of the glacial earthquakes: 32 of 46 glacial earthquakes at Jakobshavn Isbræ, 13 of 25 glacial earthquakes at Helheim Glacier, and nine of eleven glacial earthquakes at Kangerdlugssuaq Glacier. The majority of the small events (58) are identified using the cross-correlation detector, and we label these type 'A' detections. Our systematic visual inspection identifies an additional 22 events, which we label type 'B' detections. The correlation coefficients for type-B events range from 0.5 to 0.8, with the lower correlation coefficients reflecting increased waveform complexity.

The 80 new signals occur predominantly within the hour surrounding a glacial earthquake: 94% of the small type-A events occur within 15 minutes of a glacial earthquake and 98% occur within 35 minutes. By definition, all of the type-B events occur within 15 minutes of a glacial earthquake. In the majority of cases, we find no more than one small event preceding the glacial earthquakes, and no more than one event following the earthquake. However, six of the glacial earthquakes show two small preceding events, and one of the glacial earthquakes shows two small following events.

We refer to both type-A and type-B detections as 'small events' in the following discussion to distinguish them from the previously known glacial earthquakes, which show larger waveform amplitudes than these newly identified signals.

The peak amplitudes of the vertical-component seismograms recorded at the nearest station during the small events range from 10–90% of the peak amplitude of the associated glacial earthquake, with the majority of small events having amplitudes between 10% and 40% that of the associated glacial earthquake. The small events that occur after glacial earthquakes have slightly larger mean amplitudes than those that occur before, which may be because coda energy arriving from the main glacial earthquake obscures the smallest events. All of the small signals we identify are listed in Table 1; those that occur within 15 minutes of a glacial earthquake are shown in Figure 2.3. Additional examples of the seismograms for the small events are shown in Figures 2.4a, 2.5a and 2.6. The small seismic signals show a moveout of $\sim$3.6 km/s across stations of the GLISN network (Figures 2.4a, 2.5a), consistent with event occurrence at the glacier front and 35-second Rayleigh wave group velocities observed in Greenland (Darbyshire et al., 2017). Significant Love wave energy is also recorded for each small event (e.g., Figure 2.6) and the amplitude ratios between the small events and associated glacial earthquakes are typically similar for Love and Rayleigh waves.

We successfully model the forces associated with 26 of the 80 small seismic events that occur before and after glacial earthquakes (Table 1). Low signal-to-noise ratios or a small number of nearby recording stations hindered analysis of the remaining small events. Despite the low amplitudes of the signals, each small event for which we obtain acceptable results was recorded on 10–15 seismic stations around Greenland. These stations represent a subset of the 30–40 seismic stations typically used in the glacial-earthquake analysis of Olsen and Nettles (2017). To verify the robustness of our results, we use the same subset of stations to reanalyze glacial earthquakes with published CSF

solutions. This analysis returns force orientations and M_{CSF} values very similar to those obtained using the larger dataset. Previous work (Veitch and Nettles, 2012; Olsen and Nettles, 2017) has shown that errors in estimated force azimuths are likely $\sim$5° or less. Errors in CSF amplitude are less well known, and are likely most strongly affected by assumptions about the source duration. Veitch and Nettles (2012) found variability in retrieved M_{CSF} of 20–30% for a 20% change in assumed source duration. We have used the same assumptions about source duration as in earlier studies (Tsai and Ekström, 2007; Veitch and Nettles, 2012; Olsen and Nettles, 2017) for consistency.

For a single small event, there often exist two similarly well-fit solutions for the force orientation, one rotated 180° and shifted 25 s from the second. This 180° ambiguity also occurs in CSF analysis of glacial earthquakes, and arises from the band-limited nature of the seismic data and the need to analyze the signal at periods near the source duration (Veitch and Nettles, 2012). We report the inversion result for each event in Table 1; for ease of event comparison in the following text, we discuss force orientations for most events in terms of azimuth between 0° and 180° E of N.

The force orientations we retrieve for the small events are approximately perpendicular to the calving fronts of the glaciers where they occur, and are similar to the force orientations for known glacial earthquakes at those glaciers (Figure 2.7). At Jakobshavn Isbræ, 95% of published glacial-earthquake azimuths lie between 53° and 162° E of N. All but one of the small events for which we obtain solutions at Jakobshavn Isbræ have force azimuths within this range. The event with an orientation outside this range follows a calving event on 21 August 2009, and is discussed in section 5.1. At Helheim Glacier, 95% of published glacial-earthquake azimuths lie between 76° and 144° E of N. The force azimuths of all small events for which we obtain solutions at Helheim Glacier lie within this range with the exception of one force azimuth at 146° E of N. At Kangerdlugssuaq Glacier, 95% of published glacial-earthquake azimuths lie

between 94° and 169° E of N. The small event at Kangerdlugssuaq Glacier that we are able to model successfully has a force orientation 100° E of N, within this range. All small seismic events at the three glaciers for which we are able to obtain solutions show forces within 29° of horizontal. Like the force azimuths, the range of plunge angles for the small events is similar to that observed for glacial earthquakes.

The CSF amplitude values for the small events (Figure 2.8) range from 0.27–3.68 $\times 10^{13}$ kg m. The mean value for the small events (1.1×10^{13} kg m) is below that of the smallest glacial earthquake reported in the published catalog (1.2×10^{13} kg m), and all but three of the new events have M_{CSF} values smaller than 99% of glacial earthquakes in the published catalog (Figure 2.8).

We observe elevated high-frequency seismic energy (3–10 Hz) lasting 5–32 minutes surrounding all 82 glacial earthquakes in our dataset, including the subset of earthquakes (∼35%) for which we do not detect any new small seismic signals. High-frequency energy is also elevated at the time of all of the small intermediate-period seismic signals we identify. The character of the high-frequency signal is varied, but commonly involves both sharp high-amplitude peaks and emergent, lower-amplitude signal, as illustrated in Figure 2.2. The average duration of elevated high-frequency signal recorded at the nearest station during events at Helheim Glacier is slightly longer (20 minutes) than that recorded at Kangerdlugssuaq Glacier (16 minutes) or Jakobshavn Isbræ (13 minutes). For both the glacial earthquakes and the newly identified, small seismic signals, we observe a weak correlation (R^2 value between 0.2 and 0.5) between the amplitudes of the high-frequency and intermediate-period signals. The high-frequency energy recorded at the times of both glacial earthquakes and the small intermediate-period signals exhibits a smaller excursion above background levels than does the intermediate-period signal, consistent with the depletion in high-frequency energy previously observed for glacial earthquakes (e.g., Ekström et al. 2003).

2.5 Discussion

We have identified small, intermediate-period seismic events preceding or following 66% of the glacial earthquakes in our dataset. Because, in some cases, multiple small events are associated with a single glacial earthquake, the total number of new events identified nearly doubles the number of events in the original dataset. Our seismic results indicate that, like the glacial earthquakes, these events occur at the calving terminus of the glaciers. In this section, we argue that the small events we have detected represent small glacial earthquakes, and we consider the rate of occurrence of such events. We assess seismic evidence for ice-cliff failure in our dataset, and we explore empirical evidence for a relationship between seismic observations and iceberg size.

2.5.1 Evidence for a Buoyancy-Driven-Calving Source

We interpret the small seismic signals that we detect prior to and following known glacial earthquakes to be the result of buoyancy-driven calving: that is, as small glacial earthquakes produced by the same physical process as the larger, previously known glacial earthquakes. Although our analysis makes no assumption about the mechanism or geometry of the source, the small events demonstrate all of the defining characteristics of glacial earthquakes. Like glacial earthquakes, the small signals are depleted in high-frequency energy with respect to long-period energy, indicative of a slow source and consistent with the non-detection of the events using standard, high-frequency seismological approaches. As for the glacial earthquakes, the seismograms of the small events are explained well by a CSF source. Though our analysis favors no particular orientation, the retrieved force orientations are nearly horizontal and are perpendicular to the central portion of the calving terminus in nearly every case. At each glacier studied, the geometry of the forces retrieved for the small events is very similar to that of the previously reported force orientations for glacial earthquakes at the same glacier.

An additional characteristic of known glacial earthquakes is that, whenever appropriate ground- or satellite-based imagery is available, the imagery shows ice loss at the calving front at the times of the earthquakes (Nettles et al., 2008; Joughin et al., 2008a; Amundson et al., 2010; Nettles and Ekström, 2010; Veitch and Nettles, 2012; Murray et al., 2015c,a; Olsen and Nettles, 2017). Veitch and Nettles (2017) also demonstrated good agreement between changes over time in glacial-earthquake force orientations and calving-front geometry. Comparison of the small events we identify here with imagery of the calving front is challenging because nearly all of the small events occur within an hour of large, glacial-earthquake ice-loss events, while satellite imagery provides temporal resolution no better than one day. However, high-rate time-lapse imagery of the terminus of Jakobshavn Isbræ exists at the times of three of the small seismic events we report in association with glacial earthquakes. In each case, the glacier calved a small iceberg at the time of the seismic signal, and the section of the terminus where the iceberg originated can be resolved in the imagery. Our seismic analysis of these three events yields CSF orientations for each event aligned perpendicular to the section of the glacier terminus that calved (Figures 2.4b and 2.5b).

A small seismic event on 2 August 2012 at 23:04 (Figure 2.5) preceded a glacial earthquake at Jakobshavn Isbræ by six minutes. The events were captured by time-lapse imagery during a field campaign that observed the terminus of the glacier using terrestrial radar interferometry (Xie et al., 2018). During the period of the observing campaign surrounding the glacial earthquake, images of the calving front were captured every six minutes. The imagery shows two calving events, one coincident with the small event and one with the glacial earthquake. The seismically determined force azimuth for the small event is 97°, approximately normal to the section of the terminus involved in calving, as shown in Figure 2.5. The orientation of the force for the glacial earthquake that follows is very similar (119°; Olsen and Nettles, 2017).

The other two small events recorded by high-rate imagery occurred on 21 August 2009, one before and one after a glacial earthquake that has been widely studied (Walter et al., 2012; Veitch and Nettles, 2012; Sergeant et al., 2016; Veitch and Nettles, 2017). Seismograms for the two small events and the associated glacial earthquake are shown in Figure 2.4a, and the terminus geometry in Figure 2.4b. The force azimuth for the main glacial earthquake, at 07:02, was reported as 119° by Veitch and Nettles (2012), consistent with the normal to the central section of the calving front, estimated from satellite data as 116° (Veitch and Nettles, 2017). The force orientation we determine seismically for the first small seismic event, at 06:57, has an azimuth of 106°, only 13° different from the glacial earthquake. The force we retrieve for the small seismic event that occurred after the glacial earthquake, at 07:07, has an azimuth of 191°, nearly orthogonal to the forces of both the glacial earthquake and the first small seismic signal (Figure 2.4b). High-frame-rate (10 s) visual imagery taken from the side of the glacier within five kilometers of the terminus (Walter et al., 2012) allows us to assess the validity of our results and interpretation. The image sequence shows three ice-loss events, with timing matching that of the seismic signals. The approximate locations from which the icebergs calved, as determined by the high-rate imagery, are shown in Figure 2.4b by the bases of the arrows labeled 1, 2, and 3. The first two icebergs are lost against the main portion of the calving front, and the third iceberg against the southern side of the terminus. The motion of the icebergs away from the calving front is thus slightly north of west for the first small event and the glacial earthquake, and close to north for the small event following the glacial earthquake. The geometry of the forces estimated from our seismic analysis is consistent with the iceberg motion documented visually, including the change in force direction from approximately east-west to north-south observed between the first two events and the final event.

This sequence of calving events was also analyzed by Walter et al. (2012) and

Sergeant et al. (2016). The force azimuth we obtain for the first small calving event is similar to the average value reported by Sergeant and others (2016; azimuth 127°) for that event; no value for this event was obtained by Walter et al. (2012). For the main glacial earthquake, Sergeant et al. (2016) found an average force orientation of 122°, similar to the 119° reported by Veitch and Nettles (2012). Walter et al. (2012) found an azimuth of 149°; the difference between this estimate and those of Veitch and Nettles (2012) and Sergeant et al. (2016) has been attributed to data limitations and frequency-band selection in the Walter et al. (2012) study (Sergeant et al., 2016; Veitch and Nettles, 2017).

The force azimuth we calculate for the small seismic event occurring five minutes after the glacial earthquake (azimuth 191°) differs significantly from that found in previous studies for the same event: Walter et al. (2012) found an azimuth of 154°; Sergeant et al. (2016) found an azimuth of 135°. However, the terminus imagery discussed above (Walter et al., 2012) confirms the occurrence of a rotational calving event consistent with the orientation and timing obtained from our analysis. In addition, independent of any inversion procedure, the amplitudes of seismic surface waves recorded at station ILULI, and other nearby seismic stations, are consistent with the radiation patterns expected for the force orientations we estimate. Station ILULI is located 62 km west of the calving front, at a source-to-station azimuth of 275°. This places the station within a Rayleigh wave maximum for energy radiated from an east-west oriented force, but within a Love wave maximum for energy radiated from a north-south oriented force. The peak seismogram amplitudes show a ratio of about 4:1 for the main glacial earthquake (Figure 2.6) compared with the two smaller events on both the vertical and the radial components, which record the Rayleigh waves. However, the transverse-component amplitude for the small event at 07:07 is larger than that of the main glacial earthquake, consistent with the station lying near a Love wave node for

the glacial earthquake but a Love wave maximum for the later, smaller event. These observations support the results of our formal inversions, which find similar force azimuths for the 06:57 event and the main event, but an orientation rotated nearly 90°, to an approximately north-south orientation, for the event at 07:07. The imagery and seismic evidence support an interpretation in which the first small event and the glacial earthquake on 21 August 2009 were generated by buoyancy-driven iceberg calving from the central part of the terminus, and the subsequent small event by buoyancy-driven calving from the slower-flowing ice at the southern margin of the glacier, with the iceberg discharged nearly perpendicular to the flow direction. This latter, third calving event may have been enabled by the removal of ice from the central section during the first two calving events.

Our seismic analysis and the available imagery thus strongly suggest that the small intermediate-period seismic events we observe prior to and immediately following glacial earthquakes are themselves small glacial earthquakes, generated by buoyancy-driven calving. Though we are not able to obtain waveform-inversion results for all of the small events, the characteristics of the seismic signals from all of the events are similar, and we interpret all of the small events to arise from the same physical mechanism.

2.5.2 Source of the High-Frequency Signal

In addition to the discrete, intermediate-period, small seismic events generated by iceberg calving, we observe elevated high-frequency energy (3–10 Hz) throughout the duration of each calving sequence, often lasting for up to 30 minutes. The high-frequency signal is varied, and, though the high-frequency amplitudes show peaks at the times of the small seismic events and the main glacial earthquakes, we also observe high-frequency amplitude peaks at other times during the calving sequence, not coincident

in time with the intermediate-period peaks. An example is shown in Figure 2.2. We measure similar durations of high-frequency energy at stations within 100 km of the source and at stations as far as 500 km from the source, suggesting that the long duration of the signal is due to source processes related to the calving sequence, rather than to the effects of wave propagation.

High-frequency seismic signals associated with glaciated environments have been recorded in Greenland, Antarctica, and Alaska, and are known to be complex (e.g., Anandakrishnan and Bentley, 1993; O'Neel et al., 2007; MacAyeal et al., 2008; Rial et al., 2009; Amundson et al., 2010). High-frequency seismic signals originate from stick-slip motion at the ice-bed interface in Western Greenland (Röösli et al., 2016a), but generate higher frequencies (20–200 Hz) than we observe and appear to be observable only at very short distances. Signals generated by individual crevassing events are also typically characterized by higher-frequency energy ($\geq$ 10 Hz) and shorter durations ($\leq$ 10 seconds; Walter et al., 2009; Röösli et al., 2014) than we observe. Seismic tremor caused by water movement into moulins or through subglacial channels generates energy with a similar frequency content to that we observe (Röösli et al., 2014; Bartholomaus et al., 2015; Röösli et al., 2016b), but moulin tremor typically lasts for multiple hours and is most frequently documented in the afternoon, when surface drainage into moulins peaks (Röösli et al., 2014; Röösli et al., 2016b). Tremor signals generated by turbulent water flow through a subglacial conduit show peak frequencies between 1.5 and 10 Hz (Bartholomaus et al., 2015), but are nearly continuous, with amplitudes varying diurnally and seasonally. In contrast, the signals we observe have durations of only $\sim$30 minutes, limited to the time period immediately surrounding the glacial earthquake and smaller intermediate-period events we document, regardless of time of day or season.

We consider it likely that the high-frequency signal we observe is generated by multiple processes associated with ice deformation and ice and water motion during the

calving process. Some of the high-frequency signal is likely generated by high levels of crevassing, fracturing, and shearing of the ice in the near-terminus region as the icebergs detach from the glacier, and as ice near the calving margin responds to a new, post-calving stress state. Deformation of the ice mélange almost certainly contributes to the high-frequency signal (Amundson et al., 2010), and motion of water within the glacier and at the bed in response to iceberg motion and terminus deformation may provide additional contributions. Results from GPS observations at Helheim Glacier and analog tank experiments (Murray et al., 2015a) highlight the long (>5 minute) total durations of buoyancy-driven calving events, from initiation to completion of iceberg rotation. Our observations of the extended duration of high-frequency energy associated with such calving events are consistent with the glacier and mélange undergoing an extended period of deformation, likely distributed across the terminus region, as it responds to the changing geometry and stress state at the terminus region during buoyancy-driven calving events.

2.5.3 Occurrence Frequency of Buoyancy-Driven Calving Events

The small, intermediate-period seismic events we identify occur predominantly within one hour of a large glacial earthquake (98% of small events), with few additional small events in our 24-hour search window, suggesting a possible causal linkage between the small and the large events. To assess whether additional, similar events occur at other times, we (1) expand our search for small seismic events to include two additional time periods, and (2) experiment with modification to our detection parameters.

The first additional time period we consider is defined by available imagery. Using the same template waveform for Jakobshavn Isbræ as previously, we perform cross-correlation analysis on vertical-component seismic data from station ILULI for the full

time period during which Xie et al. (2018) collected radar-interferometry observations. Their observations were made at the terminus of Jakobshavn Isbræ for a total of 32 days over the summers of 2012, 2015, and 2016. In addition to the glacial earthquake on 2 August 2012 discussed in section 5.1 (the only glacial earthquake during these 32 days) and the newly identified small seismic event that precedes it, we identify 14 other small seismic events at Jakobshavn Isbræ during the 32-day time window (Table 2). Each seismic event is recorded by multiple seismic stations and accompanied by ice loss visible in the imagery, and every visible ice-loss event generates a coincident, detectable seismic signal. Seven of the small events show high enough signal-to-noise ratios at multiple GLISN stations to allow waveform modeling; the results are given in Table 2. The forces we resolve for each event are perpendicular to the region of mass loss at the terminus, and high-frequency signals are elevated at the times of these events, just as they are for the small, intermediate-period seismic events preceding or following glacial earthquakes and for the earthquakes themselves. We interpret these small events as additional, small glacial earthquakes generated by buoyancy-driven calving. Nine of the 14 events occur within 24 hours of another event, and the record includes periods as long as a week when no calving occurs, suggesting that the small events are temporally clustered, even in the absence of a larger glacial earthquake.

The second additional time period we consider spans a full season of calving at Jakobshavn Isbræ. During this time period, we search for small seismic events not associated with known glacial earthquakes. We apply our cross-correlation method to continuous seismic data recorded at station ILULI from June–August, 2013, a time period during which eleven glacial earthquakes at Jakobshavn Isbræ were identified using GSN data (Olsen and Nettles, 2017). Beyond the seven small events associated with glacial earthquakes discussed earlier, the cross-correlation detector identifies only four additional small events in the 92-day time period examined. The events are listed

in Table 2.

In our earthquake-detection approach, we have chosen fairly strict criteria for acceptance of candidate signals as true seismic sources at the calving front. In our effort to avoid false detections, we almost certainly reject some true sources, and the catalog of small seismicity presented here is likely to be incomplete. When we reduce the signal amplitude required to declare a detection (assessed visually as described in Methods), we identify as many as 22 additional small events in the 12 hours prior to the 82 glacial earthquakes considered here, and as many as eight additional small events in the full calving season we consider at Jakobshavn Isbræ. These small events share frequency-content characteristics with the small events we present in Table 1 and show the same signal moveout across the seismic network, consistent with an origin at the calving front. We favor the simple interpretation that these small events are generated by the same buoyancy-driven-calving source as the events in Table 1. The temporal clustering of these small signals around glacial earthquakes is similar to that of the A- and B-type events in Table 1. This suggests that the temporal patterns we observe in the events presented in Table 1 will hold even if the detection threshold for small events is modified. Future work towards constructing a more complete catalog or identifying a seismic magnitude of completeness will require development of a more sophisticated detection algorithm, and is beyond the scope of this study.

We conclude that small iceberg-calving events of the size reported here (surface areas down to $\sim$0.05 km^2) occur preferentially, though not exclusively, in association with the large calving events that generate teleseismically detectable glacial earthquakes. This result suggests that buoyancy-driven calving occurs primarily as discrete calving sequences, in which several significant icebergs are lost in a time period that is often $\leq$1 hour; in some cases two such sequences are observed to occur within 24 hours. Typically, these sequences are separated by days- to weeks-long periods of terminus

quiescence. The close temporal association of the calving events, and particularly the common occurrence of a precursor to the largest calving event, suggests that the events within a sequence are causally linked, with all events occurring in response to terminus conditions, or with one event triggering the next, an idea we explore further in section 5.4.

2.5.4 Small Seismic Events and the Marine Ice-Cliff Instability

Bassis and Walker (2012) calculated a thickness limit for marine-terminating glaciers that depends on water depth, but reaches a maximum of 900–1100 m, depending on the extent of crevassing and reasonable assumptions of the yield strength in ice. This maximum occurs at the glacier floatation level, such that the maximum height of the subaerial cliff face reaches roughly 90–110 m. It has been argued that, in circumstances where structural failure of thick ice and its rapid evacuation expose even thicker ice, a positive feedback leading to very rapid ice-front retreat may occur. As currently implemented in ice-sheet models, this 'marine ice-cliff instability' (MICI) leads to accelerated retreat of ice margins in Antarctica and increases the rate of projected sea-level rise (Pollard et al., 2015; DeConto and Pollard, 2016).

Jakobshavn Isbræ is about 1 km thick at its calving margin, with an ice cliff of ∼100 m extending above the waterline (e.g., Joughin et al., 2012); the corresponding thickness at Helheim Glacier has varied from ∼650 m to more than 800 m over time, with subaerial ice cliffs of ∼70–100 m (Howat et al., 2005; James et al., 2014; Kehrl et al., 2017). The terminus thickness at Kangerdlugssuaq Glacier is less well known, but the height of the subaerial cliff at the terminus was ∼100 m from 2001–2012. Ice at the terminus appears to have been close to floatation throughout this time (Kehrl et al., 2017), suggesting a total thickness similar to that of Jakobshavn Isbræ and Helheim

Glacier. The thickness of Jakobshavn Isbræ, Helheim Glacier, and Kangerdluggsuaq Glacier, similar to the calculated maximum thickness identified by Bassis and Walker (2012), suggests they may experience ice-cliff failure, and such a suggestion is implicit in the work of Pollard et al. (2015). In this section, we evaluate the relation of the small, precursory events we identify to the MICI hypothesis.

Because the Bassis and Walker (2012) model uses a depth-averaged formulation for deviatoric stress, it need not address which modes of failure are most likely to occur in order to keep an ice front at or below its maximum allowed thickness. However, the stress distribution in the ice is likely to favor particular failure modes. Failure at or near the waterline may be promoted by the concentration of stresses there due to the difference in density of air and water (e.g., Reeh, 1968; Benn et al., 2007). It has long been observed that failure of, and calving from, the subaerial portion of a marine terminus leads to a buoyancy imbalance, triggering calving of the submarine ice left behind (Motyka, 1997; O'Neel et al., 2007). Such two-part failure might also occur from well-grounded ice, leading to rapid ice-margin retreat even in thick, grounded ice like that present in some parts of Antarctica. Observations from the LeConte and Columbia glaciers in Alaska (Motyka, 1997; O'Neel et al., 2007) suggest that the triggering subaerial failure most often occurs minutes before the submarine failure. In the case of such two-stage failure, we would expect to observe seismic signals from both failure events. We therefore evaluate whether the small events we observe prior to large, glacial-earthquake calving events may represent a triggering failure of the subaerial ice cliff.

Catastrophic failure of an ice cliff due to high overburden is analogous to other mass-wasting events acting on a vertical free surface, such as a rock fall from a canyon wall. A similar set of forces is expected whether the failure occurs in ice or in rock. Collapse of a vertical rock face produces a set of seismically resolvable forces, dominated

by the vertical force generated as the mass first accelerates downward and then decelerates on impact with the ground (Gualtieri and Ekström, 2016). In direct contrast, the forces we resolve for each of the small seismic events studied here, occurring at the glacier terminus prior to major buoyancy-driven calving events, are subhorizontal, and hence inconsistent with subaerial cliff failure.

We perform a further test for the possibility of a vertical source for the small glacial events by performing the force inversion with the requirement that the retrieved force be vertical. The resulting model seismograms provide very poor fits to our data. Furthermore, the significant Love wave energy we observe for each small event is inconsistent with a vertical force. A purely vertical source would generate azimuthally uniform Rayleigh wave amplitudes, and would not excite Love waves. By contrast, a horizontal force would generate maximum Rayleigh wave energy in the direction aligned with the force, and maximum Love wave energy perpendicular to the force. We consistently observe the latter pattern of Love and Rayleigh waves generated by the small events in this study (e.g., Figure 2.6).

Alternatively, a block of ice might be detached from the subaerial cliff face along a listric fault or arcuate surface like that observed at the base of some landslides, in which the failure surface is near vertical at the uphill edge of the sliding mass, becoming near horizontal as it soles out at the downhill edge of the mass (in this case, at the waterline). We consider the minimum plunge for a force produced by such an ice slump, which would be produced by a block of ice detaching from the uppermost portion of the calving face and translating horizontally seaward on a low-angle surface within the ice and landing in the water. Given a 100-m-tall ice cliff and assuming a block measuring 50–100 m in the along-flow direction (consistent with the iceberg dimensions measured in this study for the small, precursory events), the mass movement would result in plunge angles between 40° and 60°; the center of mass must descend 90 m as the block

enters the water. These minimum plunge angles are notably higher than those we obtain for events in our dataset, all of which are less than 30° and 70% of which are <20° (Table 1).

To confirm our ability to detect an ice slump, if present, we consider the force generated by a block of ice accelerating due to gravity, and compare it to the maximum amplitude of the force active during the events we record seismically. Assuming the range of surface-area dimensions estimated by Walter et al. (2012) for the small block of ice observed to detach from Jakobshavn Isbræ five minutes before the glacial earthquake on 21 August 2009, and a thickness equal to the height of the ice above the water line (90 m), the amplitude of the vertical force generated due to gravitational acceleration of this block would be 2.4–3.6 $\times$ 10^{10} N. This range of values is at the upper end of the force amplitudes we observe for the small seismic events in this study (0.43–4.2 $\times$ 10^{10} N), and such a vertical force should therefore be clearly resolvable in our analysis, if present. This is particularly true since Rayleigh waves are recorded on the quieter, vertical component of the seismograph, rather than only on the noisier, horizontal components, as is the case for Love waves. None of the 33 small events we analyze have large vertical-force components. We therefore conclude that the small events we have identified prior to major calving events do not represent ice slumps or failure of the subaerial ice cliff, and thus do not act as a trigger for the subsequent, larger events through enhancement of super-buoyancy. Clearly, our result does not preclude the possibility of such failure in Antarctica or elsewhere; but we find no evidence for this manifestation of the marine-ice-cliff instability at Jakobshavn Isbræ, Helheim Glacier, or Kangerdlugssuaq Glacier.

We note that Pollard et al. (2015) argue that the dramatic calving events at Jakobshavn Isbræ and Helheim Glacier documented by Amundson et al. (2010) and James et al. (2014), respectively, may represent examples of individual calving events caused

by structural ice-cliff failure. Pollard et al. (2015) and DeConto and Pollard (2016) base their horizontal wastage rates on those observed for the recent, rapid retreat of the ice front at Jakobshavn Isbræ. The calving events referred to by Pollard et al. (2015) are of the type that we describe in this study as 'buoyancy driven', and, like other such events, produced glacial earthquakes. Available evidence suggests that all glacial earthquakes represent calving of the type shown in the video footage of Amundson et al. (2010) and James et al. (2014): the calving of full-thickness icebergs that overturn as they move away from the calving front. To the extent that failure through the full glacier thickness provides evidence that ice thickness is a primary control on calving rates at some Greenland glaciers, our full dataset of glacial-earthquake events would constitute evidence for the importance of structural, 'ice-cliff', failure. In that scenario, all of the events we discuss in this study — the glacial earthquakes and the small events preceding and following the glacial earthquakes — would represent evidence of marine ice-cliff failure, and, possibly, instability. This possibility merits closer examination, but we do not pursue it further here.

2.5.5 Iceberg Size and Relationship to M_{CSF}

The centroid-single-force inversions we conduct result in an estimate of the size of each seismic event, referred to as the CSF amplitude, or M_{CSF} (Table 1 and Table 2). The M_{CSF} values for the majority of the small seismic events we analyze are at or below the previously reported lower limit for glacial earthquakes (Figure 2.8). We hypothesize that these newly detected seismic events have lower M_{CSF} values primarily because they are generated by icebergs smaller than those that generate the large, globally detectable glacial earthquakes previously reported. To investigate this hypothesis, we compile estimates of iceberg size for both calving events that generated glacial earthquakes and those that generated the newly discovered small seismic signals.

The most reliable volume estimates for glacial-earthquake-producing icebergs come from ground-based, high-frame-rate imagery acquired at calving fronts. Published estimates of iceberg surface area from such data are available for five events occurring at Helheim Glacier and Jakobshavn Isbræ (Walter et al., 2012; Rosenau et al., 2013; James et al., 2014; Murray et al., 2015a). The estimates range from 0.35 km^2 to 1.8 km^2 (Figure 2.9), and correspond to map-view surface area prior to iceberg overturn. The thickness of the three glaciers we study ranges from 0.7–1 km. Because constraints on glacier thickness at the calving front are sparse, we consider the surface areas of the icebergs, rather than estimates of volume.

To obtain estimates of iceberg area for the small events we report, as well as for one additional glacial earthquake, we difference terminus positions digitized from the time series collected by Xie et al. (2018). The pairs of images are separated by 3–27 minutes. We find an iceberg surface area of 0.08 km^2 for the calving event that generated the glacial earthquake, which occurred on 2 August 2012, and areas ranging from 0.045–0.330 km^2 for the calving events that generated eight small seismic events.

We compare the estimates of iceberg size with the corresponding M_{CSF} values in Figure 2.9 (colored symbols). We find a broad correlation between iceberg area and M_{CSF}, confirming that the smaller seismic events – small glacial earthquakes – are indeed caused by calving of smaller icebergs. This relationship provides additional support for the interpretation that the small events are caused by the same physical process as the larger, previously reported events. We note that we do not expect a unique relationship between the M_{CSF} values and the iceberg mass (or area). The mass and distance terms that contribute to the CSF amplitude cannot be independently estimated from the long-period seismic data, and contributions from hydrodynamics and iceberg shape are likely to cause additional scatter in the relationship.

As an initial step towards interpretation of the observed relationship between ice-

berg size and seismic amplitude, we calculate predictions for a simple model of iceberg overturn. For a CSF source in which the accelerating mass does not change over the duration of the seismic event, the CSF amplitude can be represented as $M_{CSF} = m \times d$, where m is the mass and d the distance over which the center of mass is translated during the event. For a model in which an iceberg of rectangular cross section rotates through 90°, coming to rest with its long axis horizontal and the previous top surface of the berg flush against the calving face, d can be taken as one-half the difference in the iceberg thickness and its width. The shading in Figure 2.9 shows the range of possible M_{CSF} values given iceberg heights of either 1000 m (dark grey: estimate for thickness of Jakobshavn Isbræ; e.g., Joughin et al., 2012), or 700 m (light grey: approximate thickness of Helheim Glacier; James et al., 2014) and along-flow iceberg widths up to 100 m less than iceberg height.

Despite the highly simplified nature of the model, both the predicted range of M_{CSF} values for a given iceberg surface area and the predicted trend are similar to those observed. However, the tendency of the observations to follow the right-hand side of the predicted range of values highlights a failure of the simple model: the large-area bound of the model range corresponds to icebergs with larger aspect ratios ($\sim$0.75–0.9) than those typically observed to capsize based on limited field observations. The model does not include any contribution from calving style (e.g., bottom-out vs. top-out calving; Amundson et al., 2010; Sergeant et al., 2018), hydrodynamic contributions to the force system (Amundson et al., 2012; Murray et al., 2015a), the extent of ice mélange in the fjord system (Tsai et al., 2008), or other factors. Interpreting the observed relationship between iceberg area and M_{CSF} will require a more sophisticated model, and may require improvements in estimation of the seismological observables. For example, our M_{CSF} estimates rely on a simple assumption about the time history of the forces acting during each calving event, in which the event duration is held fixed to the same value

for all events. The retrieved value of M_{CSF} is affected by this choice, likely at the level of 10–40% (Veitch and Nettles, 2012).

Clearly, more work is needed to interpret the relationship illustrated in Figure 2.9. However, the demonstration of an empirical relationship between iceberg size and a basic seismological observable, M_{CSF}, is encouraging, and suggests the possibility of establishing geophysically useful scaling relationships between mass lost in iceberg calving events and remotely observable seismic signals. Such relationships are routinely used to aid in understanding tectonic earthquakes and, increasingly, landslides (e.g., Ekström and Stark, 2013).

Previous attempts to demonstrate any relationship between iceberg size and M_{CSF} failed in part because multiple calving events often occur between satellite image acquisitions, and in part because the previously available distribution of earthquakes sizes was very narrow. We illustrate this problem with the open circles in Figure 2.9, which show estimates of calved area obtained by differencing terminus locations digitized from Landsat 7 and 8 images taken within nine days of each other, and for which only one glacial earthquake is known to have occurred, based on records from the GSN. These estimates agree poorly with the trend defined by the suite of events with robust single-event calving-area estimates. The most likely explanation for the poor agreement is that more than one calving event occurred during the interval between Landsat images. Progress in establishing a robust observational relationship between iceberg size and seismic observables would clearly benefit from a larger dataset of well-constrained iceberg-size estimates; from improved estimates of M_{CSF} and other seismic observables for large and small events; and from improved detection capability for small events.

2.5.6 A Larger Mass-Loss Contribution from Buoyancy-Driven Calving

Our findings suggest that buoyancy-driven calving is a more frequent occurrence than previously recognized at Greenland's tidewater glaciers. The number of newly detected events is large, nearly doubling the number of known glacial-earthquake-type events for the dataset we study. The results we present here also suggest that buoyancy-driven calving is not limited to icebergs of cubic-km scale, but extends to icebergs of smaller dimensions.

We do not have direct constraints on the thickness of the small icebergs we investigate here, but the simplest interpretation is that they represent calving of the full glacier thickness. Icebergs that generate the large, previously known glacial earthquakes are observed to extend the full glacier thickness, as evidenced by sediment-laden basal ice exposed during capsize (Amundson et al., 2008; Walter et al., 2012; James et al., 2014). Although terminus undercutting due to submarine melting has been observed at several west Greenland glaciers (Fried et al., 2015; Rignot et al., 2015), such undercutting would reduce the super-buoyancy that leads to buoyancy-driven calving; and in the extreme case where the ice sits higher than its equilibrium position, would lead to vertical iceberg motion and seismic forces similar to that discussed earlier for failure of the subaerial cliff face. We do not observe this behavior.

Assuming full-thickness calving (terminus heights of 900–1000 m) for the small events we report leads to iceberg volume estimates of $\sim$0.04–0.33 km^3. These volumes are up to two orders of magnitude smaller than calved icebergs associated with previously detected glacial earthquakes (e.g., James et al., 2014), but, because the number of events is large, represent ice loss totaling an additional 10–30% of that accounted for by the existing glacial-earthquake catalog for the dataset we study.

Where continuous observational time series of the termini of these large Greenland

tidewater glaciers exist, they show that most visible ice loss occurs during calving sequences; in between, the geometry changes little. Our findings support and extend this notion. The increase in mass loss and buoyancy-driven calving suggested by our findings results primarily from additional, smaller events surrounding large events, not from additional, temporally isolated events distributed throughout the calving season. Temporal clustering of calving has previously been observed in the glacial-earthquake catalog: Jakobshavn Isbræ, Helheim Glacier, Kangerdlugssuaq Glacier, and other Greenland glaciers have all generated multiple glacial earthquakes within a 24-hour period (Tsai and Ekström, 2007; Veitch and Nettles, 2012; Olsen and Nettles, 2017). The results we present here extend our understanding of calving sequences to include icebergs across a range of sizes spanning three orders of magnitude, and to events more closely linked in time. Seismic evidence indicates that all of these icebergs are lost through buoyancy-driven calving, suggesting that such calving is more prevalent than previously recognized, and that buoyancy-driven calving is likely to dominate dynamic mass loss at near-grounded tidewater glaciers, as suggested by James et al. (2014) and Murray et al. (2015c).

2.6 Conclusions

We employ seismic data recorded at regional distances to identify previously undetected seismic signals associated with glacier calving at Greenland's three largest glaciers. Waveform-modeling results demonstrate that the small seismic events we detect are generated by near-horizontal forces, and we interpret them as small glacial earthquakes caused by buoyancy-driven calving of icebergs with volumes 0.04–0.33 km^3, much smaller than the cubic-km-scale icebergs known to cause previously reported glacial earthquakes. Our results increase the number of known glacial earthquakes for the time period and glaciers we study by ∼98%. Using well-constrained estimates of

iceberg size obtained in this study and from published sources, we demonstrate an empirical relationship between the size of the glacial-earthquake seismic signal and the size of the calved iceberg. The relationship agrees broadly with a simple model relating iceberg surface area and the glacial-earthquake CSF amplitude. This result, along with progress in understanding seismic signals using numerical and analog models of calving (e.g., Murray et al., 2015a; Sergeant et al., 2018, 2019), increases the utility of the seismic data as a remote-sensing tool for interrogating calving processes and glacier dynamics at large tidewater glaciers.

Although the new events we detect occasionally occur in isolation, they occur most often in close temporal association with large glacial-earthquake events. The frequent occurrence of small seismic events in the minutes preceding large, buoyancy-driven calving events leads us to explore whether the precursory signals might represent failure of the subaerial cliff face, triggering the subsequent, large calving events in a version of the marine-ice-cliff instability mechanism. We find no evidence for such a mechanism. However, it is likely that the calving sequences occur at a time favored by background conditions at the terminus, and that the loss of a small or large iceberg from one section of the terminus changes the stress state in a manner that promotes failure on adjacent, uncalved sections. Changes in the strength of the proglacial ice mélange resulting from large calving events may also promote event clustering like that we observe.

Between buoyancy-driven seismogenic calving events, the calving front appears largely quiescent. High-rate imagery constraints from Jakobshavn Isbræ confirm that no significant calving occurs during periods without seismic activity. Our results suggest that the amount of ice lost due to buoyancy-driven calving at Greenland's glaciers is larger by ∼10–30% than previously known, and that the buoyancy-driven calving mechanism dominates ice loss at glaciers where the calving terminus is near the grounding

line.

2.7 Acknowledgements

This work was supported by NSF grants EAR–1639131 and ARC–1304346 and an NSF Graduate Research Fellowship to K. Olsen (DGE–1644869). We acknowledge the use of seismic data from the Greenland Ice Sheet Monitoring Network and the Global Seismographic Network. All seismic data are publicly available from the IRIS DMC. Full glacial-earthquake parameters for all cataloged events are available at www.globalcmt.org, as are CSF results for the new events presented here. Landsat imagery is available at www.earthexplorer.usgs.gov. High-frame-rate ground-based imagery from Jakobshavn Isbræ collected by Xie et al. (2018) are available in the supplement of that paper. We thank Göran Ekström and Jonathan Kingslake for productive discussions, and Mark Fahnestock for sharing time-lapse imagery of calving events. We appreciate constructive comments from reviewers J. Carmichael, B. Lipovsky, and A. Sergeant, and Associate Editor O. Sergienko. We declare no conflicts of interest.

Table 1: Timing and centroid-single-force solutions for the small seismic events of this study. Columns give glacier name; event number; parameters for small events before a glacial earthquake: azimuth of CSF vector in degrees east of north; plunge of CSF vector in degrees with respect to horizontal; CSF amplitude M_{CSF}, in units of kg m, to be scaled by 10^{13} (for event 1, M_{CSF} = 0.69 x 10^{13} kg m); time of small event; number of minutes small event occurred before glacial earthquake; glacial earthquake event name; parameters for small events after a glacial earthquake: number of minutes small event occurred after glacial earthquake; time of small event; azimuth of CSF vector in degrees east of north; plunge of CSF vector in degrees with respect to horizontal; CSF amplitude M_{CSF}, in units of kg m, to be scaled by 10^{13}. Type-B small events are listed in bold, all other small events listed are type A.

	Small Event Before							Small Event After				
	No.	Az.	Pl.	M_{CSF}	Time	Minutes Before	Glacial Earthquake	Minutes After	Time	Az.	Pl.	M_{CSF}
Jakobshavn Isbræ												
	1	112	–29	0.69	20:09	3	200908112012A	6	20:18			
	2	106	–8	0.44	6:57	5	200908210702A	5	7:07	191	–10	1.23
	3				1:06	6	201003190112A	–	–			
	4				–	–	201004141410A	4	14:14	293	6	0.39
	5				–	–	201005210356A	6	4:02	90	–2	0.44
	6				9:20	3	201006170923A	–	–			
	7				4:32	408	201007151120A	–	–			
					11:17	**3**	201007151120A	**4**	**11:24**	**99**	**–8**	**1.30**
	8				15:54	6	201008191600A	–	–			
	9				**13:42**	**2**	201202121344A	6	13:50	302	15	0.37
	10				–	–	201202121616A	17	16:33			
	11				20:16	405	201206260301A	–	–			
		296	18	0.69	2:58	3	201206260301A	5	3:06	110	–21	0.48
	12	139	–7	1.12	20:12	10	201207082022A	–	–			
	13	277	5	0.40	23:04	6	201208022310A	–	–			
	14				**8:18**	**2**	201209020820A	–	–			
					8:10	10	201209020820A	–	–			
	15				9:05	10	201209070915A	–	–			
					9:12	**3**	201209070915A	–	–			
	16				**14:44**	**2**	201209221446A	–	–			
	17	131	–17	0.66	12:50	3	201209241253A	–	–			
	18				16:04	2	201211241606A	–	–			
	19				9:04	13	201301120917A	–	–			
	20				9:01	4	201303290905A	**7**	**9:12**	**285**	**22**	**0.88**
	21				2:47	11	201304060258A	**4**	**3:02**	**282**	**19**	**1.17**
	22				**12:37**	**8**	201305231245A	–	–			
	23				–	–	201306170349A	7	3:56			
	24				17:47	2	201306241749A	–	–			
	25				20:05	6	201306272011A	–	–			
					20:09	**2**	201306272011A	–	–			
	26				4:01	4	201307010405A	–	–			
	27				–	–	201307030819A	6	8:25			
	28				**23:39**	**2**	201307162341B	6	23:47	314	23	1.42
	29	112	–18	1.01	8:56	4	201309090900A	23	9:23	331	0	1.71
					–	–	201309090900A	35	9:35			
	30				**18:44**	**15**	201309101859A	–	–			
		338	5	0.80	18:48	11	201309101859A	**15**	**19:14**			
	31				**3:01**	**3**	201309110304A	8	3:12			
	32				–	–	201312050954A	7	10:01			
Helheim Glacier												
	33	292	1	0.52	14:04	5	201106211409A	–	–			
	34				–	–	201106251317A	**9**	**13:26**	**129**	**5**	**1.38**
	35	313	–25	1.02	3:47	14	201112040401A	–	–			
	36	268	–27	1.22	1:48	6	201201170154A	–	–			
	37				–	–	201204140148A	14	2:02			
	38	**326**	**–11**		**19:15**	**4**	201208231919A	10	19:29			
	39	**304**	**–8**	**2.78**	**18:18**	**11**	201209271829A	–	–			
	40				11:36	5	201303041141A	**4**	**11:45**	**310**	**–6**	**2.64**
	41				–	–	201303140346A	9	3:55			
	42				11:30	10	201304131140A	–	–			
	43				19:49	12	201307302001A	–	–			
	44				23:36	5	201308142341A	–	–			
	45				–	–	201308142350A	10	00:00			
Kangerdlugssuaq Glacier												
	46				12:58	3	200109031301	**7**	**13:08**			
	47				16:34	3	200110011637	**9**	**16:46**			
	48				2:43	3	200111290246	**12**	**2:58**			
	49				7:23	4	200112200727	15	7:42			
	50				17:16	3	200112281719	–	–			
	51				**13:49**	**2**	201109191351A	5	13:56			
	52				7:23	2	201112050725A	7	7:32			
	53				–	–	201212051626A	8	16:34			
	54	280	1	0.27	2:34	4	201212150238A	–	–			

Table 2: Seismic signals coincident with ice-loss events observable in imagery of Xie et al. [2018] (first 14 events listed) or observable in the June-August, 2013 seismic record at Jakobshavn Isbræ (last four events listed). Columns give date and time of small event; azimuth of CSF vector in degrees east of north; plunge of CSF vector in degrees with respect to horizontal; CSF amplitude M_{CSF}, in units of kg m, to be scaled by 10^{13}. Observing periods of Xie et al. [2018] were 31 July – 12 August, 2012; 6 June – 10 June, 2015; and 7 June – 20 June, 2016. Type-B small events are listed in bold, all other small events listed are type A.

Y	M	D	h	m	Az.	Pl.	M_{CSF}
2012	7	31	18	29	288	1	0.44
2012	**8**	**1**	**19**	**4**			
2012	8	2	8	7			
2012	8	2	10	28			
2012	**8**	**3**	**4**	**15**	**5**	**–1**	**0.73**
2012	8	3	8	38			
2012	8	4	10	11	119	–9	1.00
2012	**8**	**5**	**1**	**47**	**133**	**–11**	**1.07**
2012	8	5	1	50	218	24	0.40
2012	8	5	3	7	358	8	0.78
2015	6	9	6	30			
2015	6	9	8	35			
2015	6	10	13	25	296	22	1.13
2016	6	10	9	14			
2013	7	8	9	9			
2013	7	14	7	4			
2013	7	22	18	3			
2013	8	10	11	36			

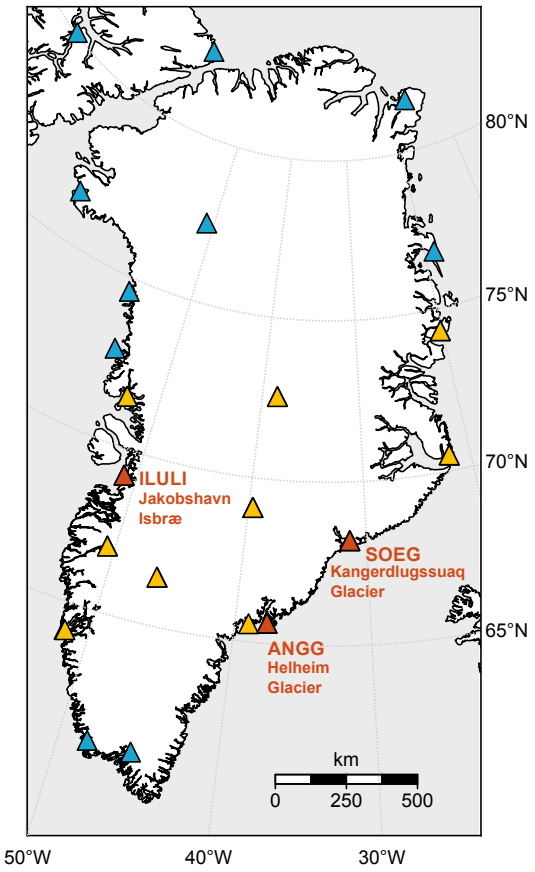

Figure 2.1: Locations of glaciers investigated in this study, and (triangles) seismic stations around Greenland. Red triangles show the stations closest to the three focus glaciers. Yellow triangles show other GLISN stations used in this study. Blue triangles show additional GLISN stations not used in this work.

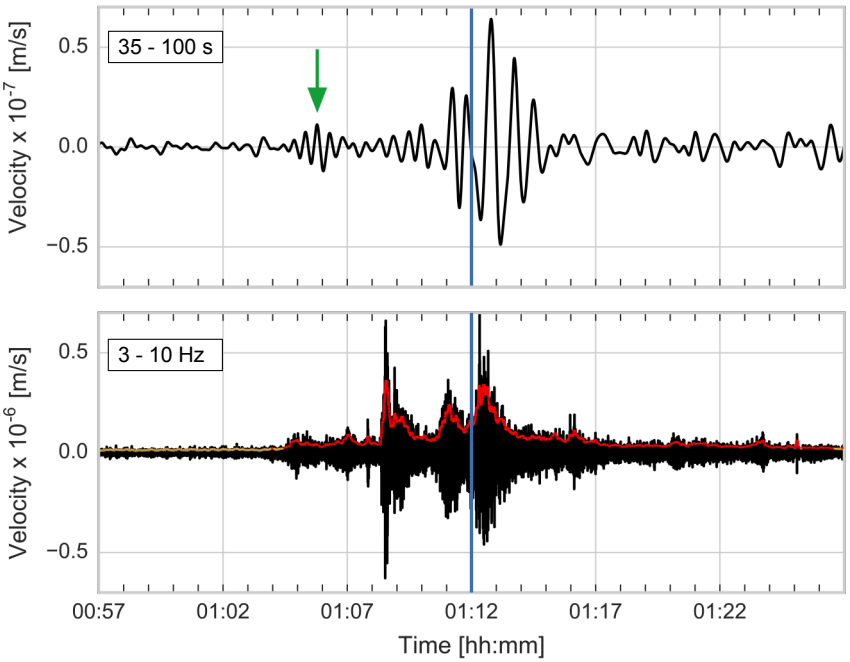

Figure 2.2: Vertical-component seismic data recorded at GLISN station ILULI. Largest-amplitude signal is a glacial earthquake at Jakobshavn Isbræ on 19 March 2010. Blue line indicates centroid time of the glacial earthquake (Veitch and Nettles, 2012). Data are filtered to 35–100 s (top panel) and 3–10 Hz (bottom panel). Green arrow identifies small seismic signal in intermediate-period data. Colored trace in bottom panel shows envelope of the data. Red denotes signal exceeding three times the standard deviation of the background signal; yellow denotes signal below this threshold.

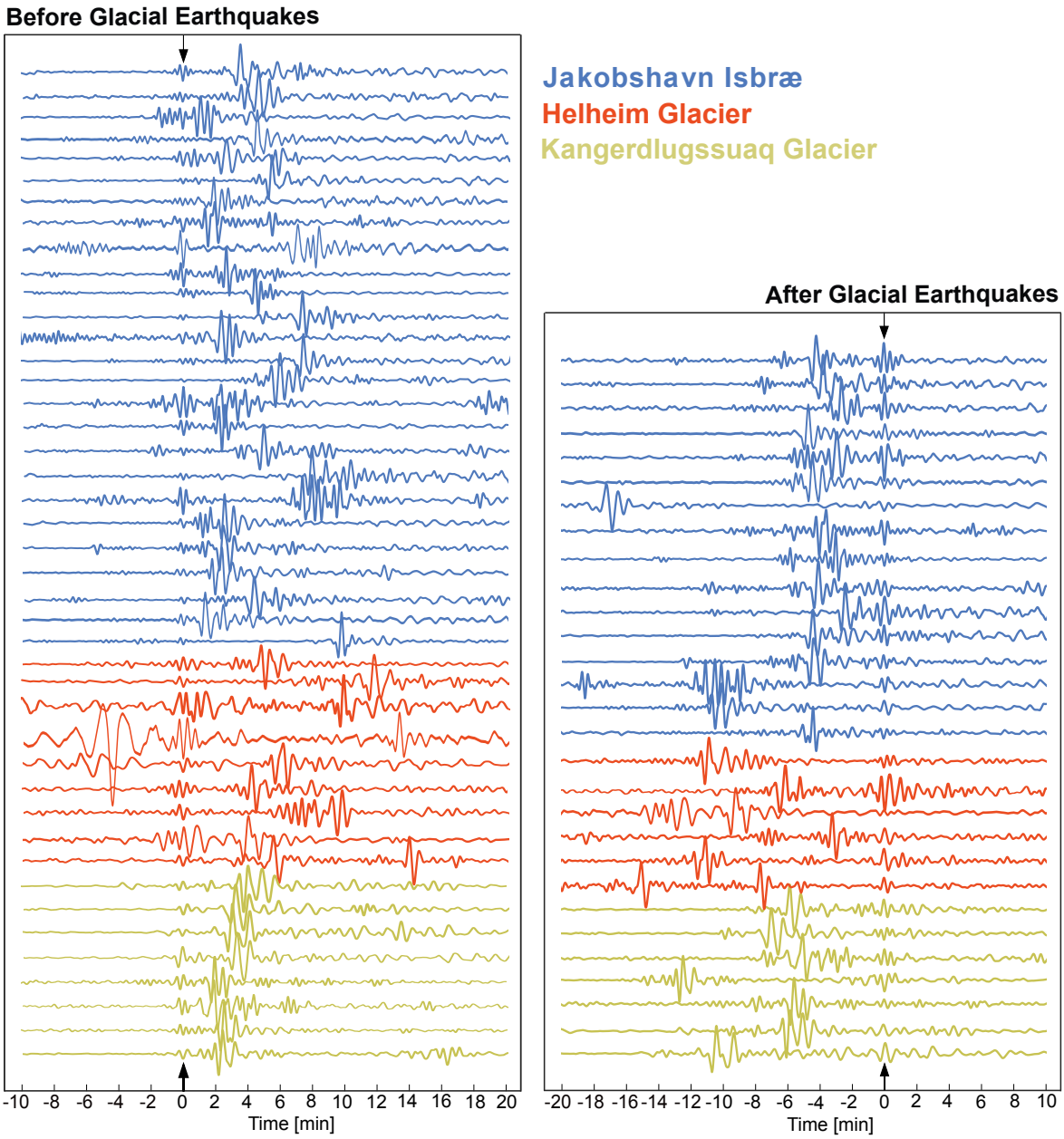

Figure 2.3: Velocity seismograms filtered to 35–100 s and aligned on newly identified small seismic signals occurring (left panel) before or (right panel) after a glacial earthquake. Each line shows a seismogram for a single glacial earthquake, recorded by the closest seismic station, and normalized by the amplitude of the glacial earthquake.

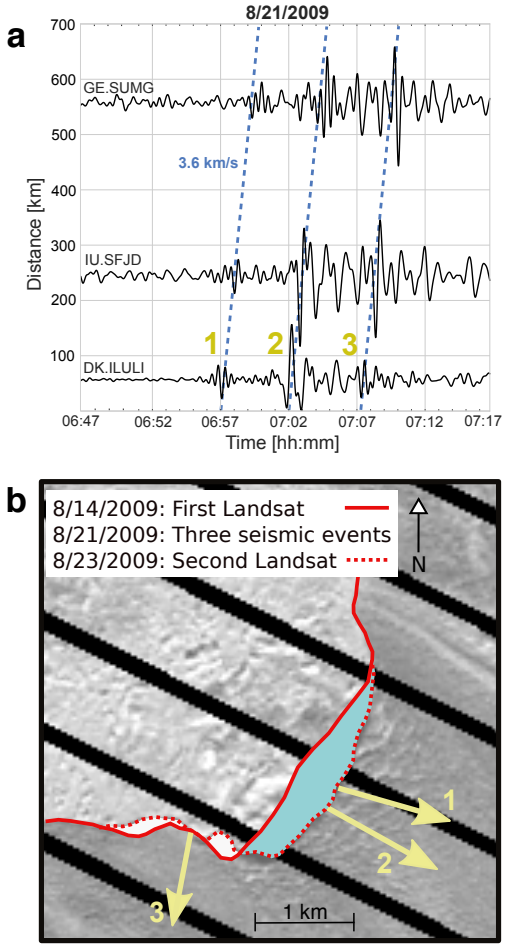

Figure 2.4: Ice-loss events on 21 August 2009 at Jakobshavn Isbræ. a) Record section for the glacial earthquake on 21 August 2009 and the small seismic events surrounding it. Yellow numbers indicate seismic events that generated the forces shown by arrows in panel b. Blue dashed lines show 3.6 km/s velocity moveout. b) Landsat 7 image of the glacier terminus. Solid red line indicates terminus position on 14 August 2009, before calving activity began. Dashed red line indicates terminus position on 23 August 2009. Blue area shows total area lost in seismic events 1 and 2 (panel a). White areas identify ice advance between the two Landsat images. Black lines are unimaged sections due to failure of the Landsat 7 scan-line corrector. Yellow arrows indicate force orientations for each seismic event, obtained from waveform modeling. Seismic event 2 is a known glacial earthquake; force azimuth for this event is from Veitch and Nettles (2012). Seismic event 1 at station ILULI is the template event used for cross correlation of seismic data recorded at that station.

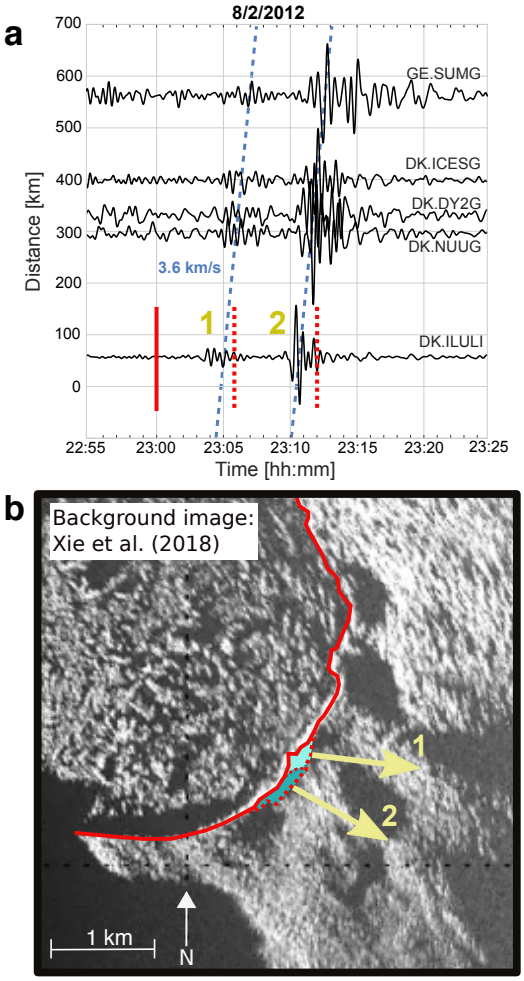

Figure 2.5: Ice-loss events on 2 August 2012 at Jakobshavn Isbræ. a) Record section for the glacial earthquake on 2 August 2012 and the small seismic event preceding it. Solid and dashed red bars indicate timing of images showing terminus positions identified in the bottom panel. Yellow numbers indicate seismic events that generated the forces shown by arrows in panel b. Blue dashed lines show 3.6 km/s velocity moveout. b) Image from Xie et al. (2018) showing calving front on 2 August 2012. Solid red line indicates terminus position at 23:00, before calving activity began. Light blue area identifies area lost in first calving event. Dark blue area identifies area lost in second calving event, which generated a glacial earthquake. Yellow arrows indicate force orientations for each event, obtained from waveform modeling. Force azimuth for event 2 is from Olsen and Nettles (2017).

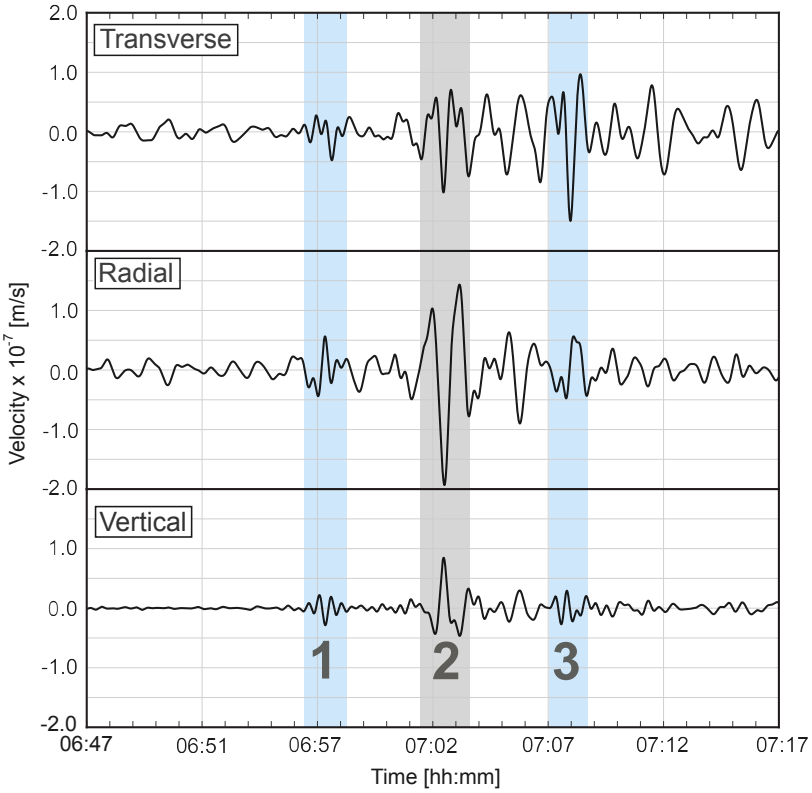

Figure 2.6: Three-component seismic data for the seismic events at Jakobshavn Isbræ on 21 August 2009, recorded at GLISN station ILULI. Glacial earthquake occurs at 07:02 (grey shading). Two of the small seismic events analyzed in this study (blue shading) can be seen at 06:57 (event 1) and at 07:07 (event 3). The three numbered events are the same as those identified in Figure 2.4. Love waves are observed on the transverse component, and Rayleigh waves on the radial and vertical components.

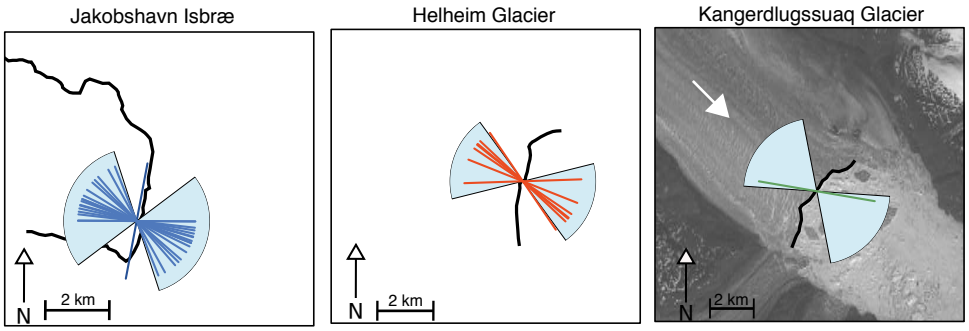

Figure 2.7: Landsat images from summer 2013 showing each glacier terminus (black line). White arrows indicate direction of glacier flow. Light-blue wedges show the orientation of 95% of published glacial-earthquake force azimuths at each glacier. Colored bars show the orientations of forces we obtain for the small events of this study. The outlying event at Jakobshavn Isbræ corresponds to event 3 in Figure 2.4, and is discussed in Section 5.1.

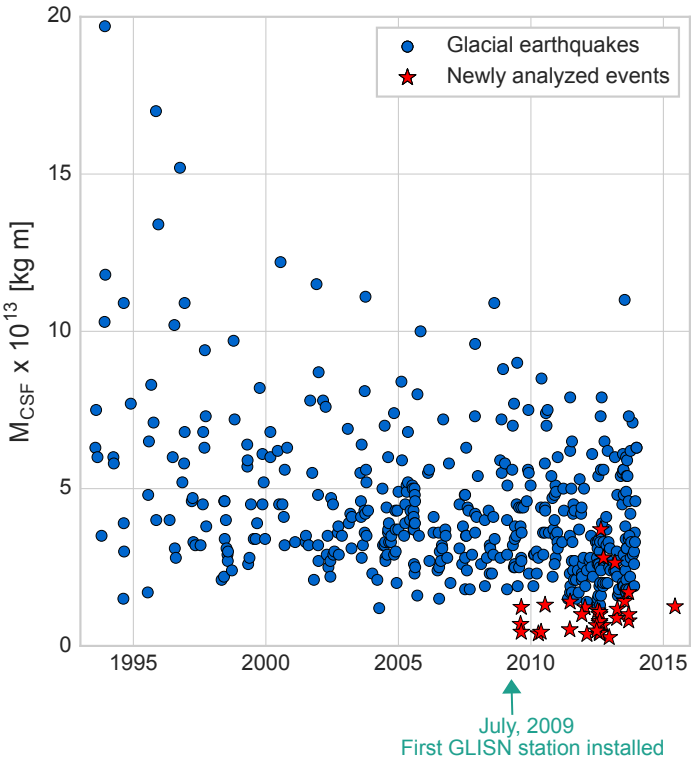

Figure 2.8: Seismically determined M_{CSF} values for all (blue circles) glacial earthquakes in the published catalog and for (red stars) newly analyzed events presented in this study.

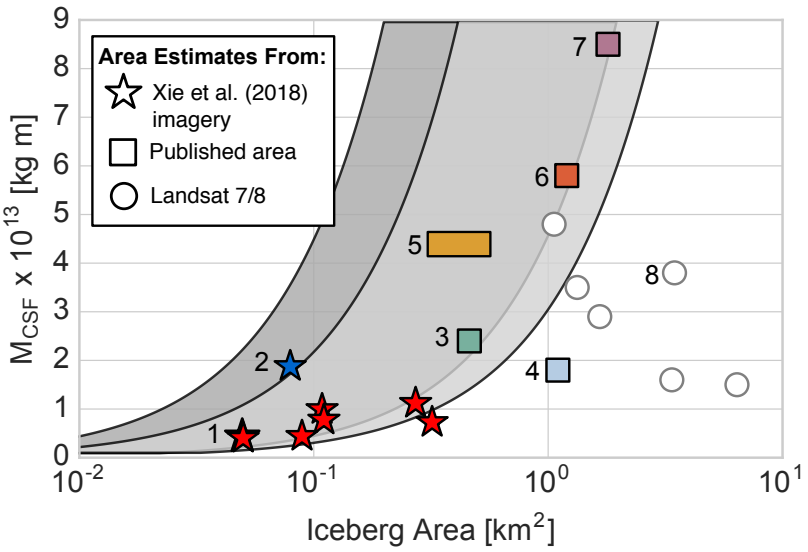

Figure 2.9: Comparison between M_{CSF} and iceberg surface area. 1. Red stars: small seismic events at Jakobshavn Isbræ with iceberg areas estimated in this study from imagery of Xie et al. (2018). 2. Blue star: glacial earthquake at Jakobshavn Isbræ on 2 August 2012; area estimated in this study from imagery of Xie et al. (2018). 3. Glacial earthquake at Helheim Glacier on 25 July 2013; area estimated by Murray et al. (2015c) from ground-based imagery. 4. Glacial earthquake at Helheim Glacier on 31 July 2013; area estimated by Murray et al. (2015c) from ground-based imagery. 5. Glacial earthquake at Jakobshavn Isbræ on 21 August 2009; rectangle shows range of surface areas estimated by Walter et al. (2012). 6. Glacial earthquake at Helheim Glacier on 12 July 2010, area estimated by James et al. (2014) from ground-based imagery. 7. Glacial earthquake at Jakobshavn Isbræ on 27 May 2010; area estimated by Rosenau et al. (2013) from ground-based imagery. 8. White circles: glacial earthquakes with area estimates from Landsat 7 and 8 images (this study). Grey shading represents values expected from a simple model of the relationship between iceberg area and M_{CSF} in which iceberg height is fixed either at 1000 m (dark grey) or 700 m (light grey). See section 5.5 for further details.

Chapter 3

Improved Estimation of Glacial-Earthquake Size Through New Modeling of the Seismic Source

Abstract

The number of gigaton-sized iceberg-calving events occurring annually at Greenland glaciers is increasing, part of a larger trend of accelerating mass loss from the Greenland ice sheet. Though visual observation of large calving events is rare, up to 50 glacial earthquakes generated by these calving events are recorded teleseismically each year. Both glacial-earthquake magnitudes and the size of the icebergs that generate them span approximately an order of magnitude, but the relationship between these two parameters has not been well understood. The first demonstration of an empirical relationship between iceberg size and a summary measure of glacial-earthquake magnitude, M_{CSF}, was recently presented based on a subset of well-studied calving events (Olsen and Nettles, 2019). However, a known limitation of the M_{CSF} metric is its sensitivity to choices made about the representation of the seismic source. Compared to tectonic earthquakes, relatively little is known about the shape and duration of the glacial-earthquake source time function.

In this study, we evaluate whether the use of more-sophisticated source models would improve the accuracy of estimated source parameters. We incorporate

constraints on the character of the seismic source from field and laboratory studies of calving (Murray et al., 2015a; Cathles et al., 2015) and numerical models (Sergeant et al., 2018), and test a variety of source functions using both synthetic and observed glacial-earthquake waveforms. We demonstrate a three-fold improvement in recovery of maximum-force values using source models informed by laboratory and field data. Because the maximum-force values recovered through waveform modeling have significantly less dependence on model duration than does M_{CSF}, we prefer maximum force as a measure of glacial-earthquake size. We demonstrate a correlation between maximum-force values recovered using our newly developed models and iceberg mass. Though a one-to-one relationship is not expected between glacial-earthquake magnitude and iceberg size, our results suggest the possibility of developing a useful scaling relationship between these two parameters.

3.1 Introduction

Ice loss from the Greenland ice sheet has accelerated in recent years, and up to half of that mass loss results from iceberg calving. More than 200 glaciers around Greenland advect ice from the interior of the ice sheet to the ocean (Moon et al., 2012), and during the summer months, multiple large iceberg-calving events can occur at a single glacier over the course of a day (e.g., Olsen and Nettles, 2019). Some of the largest calving events involve icebergs up to $\sim$1 km^3 in scale that are driven to capsize against the glacier terminus by buoyancy forces. These rotational calving events generate glacial earthquakes, magnitude $\sim$5 seismic events that can be detected using the broadband stations of the Global Seismographic Network (GSN) and the Greenland Ice Sheet Monitoring Network (GLISN). During calving, the motion of the iceberg and the water it displaces exert a time-varying force upon the earth. The seismic waves generated by these forces contain information about the physics of the calving process, and about

the iceberg that was lost.

Study of glacial earthquakes allows retrieval of source parameters for each event. Approximately 450 events from 1993–2013 have been cataloged and analyzed systematically (Tsai and Ekström, 2007; Veitch and Nettles, 2012; Olsen and Nettles, 2017, 2019), using a centroid-single-force (CSF) approach (Kawakatsu, 1989; Ekström et al., 2003). All events were analyzed using a fixed depth and a double-boxcar-shaped model of the force history. Parameters estimated include event timing, location, force orientation, and a summary measure of glacial-earthquake size, M_{CSF}. Glacial-earthquake locations are accurate to about 15 km and track the evolution of glacier-terminus position (Veitch and Nettles, 2012, 2017). Seismically determined force orientations have been shown to be accurate to within $\sim 10^{\circ}$ by comparison with ground-truth data (Veitch and Nettles, 2017; Olsen and Nettles, 2017, 2019).

In a recent study (Olsen and Nettles, 2019), we provided the first demonstration of a correlation between iceberg size and M_{CSF}. Analysis of an additional nine calving events shows them to be in close agreement with the previously reported trend (Figure 3.1). Further, the relationship between seismic magnitude and iceberg size follows the general trend of a very simple geometric model constructed by assuming that the seismic magnitude of a glacial earthquake depends solely on iceberg mass and the distance required for the iceberg to capsize. However, the seismically estimated M_{CSF} values are systematically smaller than the predicted values for icebergs of typically observed width-to-height aspect ratios. Given the observed dimensions of each iceberg, the simple model predicts M_{CSF} values approximately an order of magnitude larger than observed. Model predictions for M_{CSF} are shown in Figure 3.1 with white symbols. The empirical demonstration of a clear relationship between seismic magnitude and iceberg size, combined with the unexpected relationship with the simple model, suggests that a more detailed investigation is merited.

The disagreement between model predictions and observed glacial-earthquake parameters is unlikely to come from errors in the estimates of iceberg size, which are on the order of 0.01 km^2 (Timothy James, personal communication). Formal errors in M_{CSF} values likewise do not account for the differences, as they are approximately 10% of reported M_{CSF} values. However, the formal errors likely underestimate the true errors, since they do not take into account systematic errors, or error introduced due to incorrect assumptions in the forward model.

The modeling assumption most likely to affect estimates of earthquake size is the specified force-time function. Tsai et al. (2008) considered a range of force models and found that glacial-earthquake waveforms could be modeled well using a 50-s, symmetric, double-boxcar force model like that shown in Figure 3.2a and used in the studies of Tsai and Ekström (2007), Veitch and Nettles (2012) and Olsen and Nettles (2017), or using asymmetric boxcar models of varying durations. However, the M_{CSF} values obtained are known to be sensitive to the duration of the source model used in the analysis. Veitch and Nettles (2012) demonstrated that retaining the boxcar shape but varying the duration of the force function by 20% changed the estimated M_{CSF} value by 20-30%. Extending this analysis, we find that doubling the source-model duration can increase the estimated M_{CSF} value by a factor of 4 or more (Figure 3.3), though estimates of force geometry change very little.

Earthquakes the size of the glacial earthquakes (M_{SW} ∼4.6–5.2) generate surface waves most easily analyzed in the period band from ∼40–150 s, where signal strength is high, Earth noise is relatively low, and the Earth's lateral velocity heterogeneity is well described. For this reason, CMT and CSF analysis use seismograms in this frequency band as primary data constraints. Tectonic earthquakes of these magnitudes have durations of a few seconds, such that estimates of scalar moment, M_0, are only weakly sensitive to the choice of the moment-rate function used for analysis. However,

the duration of the glacial earthquakes is long, and similar to the period band used in CSF analysis, making estimates of M_{CSF} sensitive to the choice of force-time history. A key limitation in the estimation of the M_{CSF} parameter is thus our lack of knowledge of the true force-time history for the glacial earthquake. Because of this lack of knowledge, all glacial earthquakes in the catalog have been modeled using the same simple source model with a fixed duration and shape (Tsai and Ekström, 2007; Veitch and Nettles, 2012; Olsen and Nettles, 2017, 2019).

Ideally, a description of the force-time history for glacial earthquakes could be extracted directly from the seismic waveforms. However, the slow source process of the glacial earthquakes (10s of s) results in seismic waves that are depleted in high-frequency energy at periods shorter than ∼30–50 s. The high-frequency depletion of glacial-earthquake events has long been recognized (Ekström et al., 2003), and is the reason glacial earthquakes go undetected by short-period body-wave detectors. Olsen and Nettles (2019) employed data recorded by GLISN seismometers located within 100 km of glacier termini and confirmed the lack of coherent signal at short periods. Glacial-earthquake energy is also limited at long periods because of the relatively small sizes of even the largest glacial earthquakes (M_{SW} ∼5). Even at quiet, nearby seismic stations glacial-earthquake energy is below noise levels at periods above 100–150 s.

In recent years, field observations (Murray et al., 2015a), laboratory experiments (Cathles et al., 2015; Amundson et al., 2012; Burton et al., 2012), and numerical modeling (Sergeant et al., 2018) have advanced our understanding of the iceberg calving that generates glacial earthquakes. These studies have begun to place constraints on the character of the force history associated with the glacial-earthquake source. In this study, we test the feasibility of incorporating such observations into an improved description of the glacial-earthquake force history. We assess the ability of more-sophisticated models to return improved estimates of source parameters, includ-

ing metrics of glacial-earthquake size. Using both observed and synthetic seismograms, we also assess the relationship between alternative metrics of seismic magnitude, such as peak force, and iceberg mass.

3.2 Background

3.2.1 Glacial Earthquakes

Glacial earthquakes are generated by a style of mass loss known as buoyancy-driven calving, which occurs when a tidewater glacier terminates close to its grounding line, and icebergs are lost from a short ($\sim\leq$1 km) floating ice tongue. If the glacier terminus is driven below isostatic equilibrium as it flows into the water, buoyancy forces will push upwards on the short floating ice tongue, driving basal crevassing and subsequent iceberg calving. Icebergs lost through buoyancy-driven calving extend the full glacier thickness (up to $\sim$1 km) and have been observed to have width-to-height ratios of $\sim$0.1 - 0.5 (Murray et al., 2015a; Olsen and Nettles, 2019; Walter et al., 2012; James et al., 2014; Amundson et al., 2010). This tall, narrow geometry is unstable and leads the iceberg to capsize against the terminus. The majority of these calving events involve bottom-out iceberg rotation, where the top of the iceberg remains pinned against the terminus during the first stages of rotation while the lower portion of the iceberg rotates up in the water column and away from the terminus. A limited number of top-out calving events have also been observed (e.g., Walter et al., 2012), but this calving geometry is rare.

During iceberg capsize, time-varying horizontal and vertical forces are applied to the Earth, which generate the seismic waves recorded as a glacial earthquake. The largest-amplitude force is horizontal, generated by the iceberg accelerating into the fjord and away from the glacier terminus during capsize (Nettles and Ekström, 2010;

Murray et al., 2015a). A small vertical force is simultaneously generated behind the rotating iceberg by a pressure drop in the water column (Murray et al., 2015a). The sum of these forces is a subhorizontal force acting on the glacier terminus perpendicular to the calving face. In the majority of glacial earthquakes this force has been found to be initially oriented upglacier and between 0 – 30° uphill, reversing direction as the iceberg decelerates (Veitch and Nettles, 2012, 2017; Olsen and Nettles, 2017, 2019). For a minority of events, the force orientation estimated by the best-fit solution is instead initially oriented downglacier and downhill. For this smaller subset of events, a second acceptable solution with an upglacier-uphill orientation can be obtained by shifting the centroid time by 25 s. This trade-off between orientation and centroid time arises from the fact that the glacial-earthquake signal must be analyzed at periods close to the source duration, along with the band-limited nature of the seismic data.

3.2.2 Estimation of the Seismic Source

The time-varying force exerted by a calving iceberg in the direction opposite its acceleration is similar in both geometry and frequency content to the forces generated by a landslide mass accelerating downhill. Because of these similarities, glacial earthquakes are modeled using a technique developed for the seismic analysis of landslides, known as a centroid-single-force (CSF) approach (Kawakatsu, 1989; Ekström et al., 2003). The CSF technique is closely related to the centroid-moment-tensor (CMT) technique (e.g., Dziewoński et al., 1981) used to model the source of tectonic earthquakes.

Ground motion recorded at a seismic station depends on the source that generates the waves and on the Earth structure through which the waves travel. Ground motion u in direction k recorded at a seismic station at location $\mathbf{r}$ can be written

$$u_k(\mathbf{r}, t) = \sum_{i=1}^{3} \Psi_{ik}(\mathbf{r}, \mathbf{r}_s, t) * S(t) \cdot f_i$$

where the Green function Ψ describes the predicted seismogram generated by a point force $\mathbf{f}$ in direction i, acting at location $\mathbf{r}_s$, for a given model for Earth structure. The time history of the seismic source is represented by the function $S(t)$. The $*$ denotes convolution.

In the CMT approach, the vector f_i contains the amplitudes of the six elements of the moment tensor. In CSF analysis of both landslides and glacial earthquakes, the elements of vector f_i describe the amplitudes of the three orthogonal components of the active single force. Thus, the formulation of the ground-motion equation is similar for CMT and CSF analysis and accurate ground-motion prediction relies upon both a robust model of Earth structure and model of the source time function. A point-source approximation in space is adequate for long-period data (if the wavelength is much greater than the spatial extent of the source). $S(t)$ is specified in both CSF and CMT analysis due to the fact that in both cases the data used have little sensitivity to the shape of the source function.

With models for both structure and source defined, the inverse problem can be solved for f_i. In practice the source time and location of an event are not precisely known upon event detection. Therefore, inversion for the elements of the source as well as the event time and location is conducted simultaneously, using an iterative approach developed by Dziewoński et al. (1981), and following the implementation of Ekström et al. (2012).

Whereas in teleseismic studies of tectonic earthquakes the moment-rate function describes the source variation with time, in CSF analysis the force history or its integral is used as the source-time function, $S(t)$. A simple double boxcar force model of the seismic source of glacial earthquakes (Figure 3.2a) has been used in analysis of all events in the glacial-earthquake catalog to date (Tsai and Ekström, 2007; Veitch and Nettles, 2012; Olsen and Nettles, 2017). This model specifies a 50-s-long, anti-symmetric source

function that represents a constant force applied to the glacier terminus for 25 s as the iceberg accelerates away from the terminus, followed by a 25-s deceleration phase that applies a force of equal amplitude and opposite sign (Figure 3.2a). The model satisfies the requirement that momentum be conserved and that the system be at rest before and after a calving event. This model has been found to produce good fits to data. Given a constant mass, the first integral of the CSF force history with respect to time represents the momentum history of the sliding mass, also known as the impulse (Figure 3.2b), and the twice-integrated force history can be interpreted as the product of mass and distance. The value to which the mass x distance product converges (the zero-frequency value) has been termed the centroid-single-force magnitude, M_{CSF} (Figure 3.2c). The M_{CSF} value is analogous to the measure of seismic moment for a tectonic earthquake, in the sense that it is a summary measure of earthquake size obtained when the event has terminated. As with tectonic-earthquake studies, zero-frequency data are not necessary to retrieve an estimate of seismic magnitude for glacial earthquakes. Instead, in both tectonic- and glacial-earthquake studies, an accurate model of the seismic source allows for accurate retrieval of event size.

3.2.3 Constraints on the Shape of the Glacial-Earthquake Force History

GPS Observations and Analog Laboratory Experiments of Iceberg Calving

Though field observations of buoyancy-driven calving are sparse, insight has been gained through analog studies simulating iceberg calving with a plastic block within a water-filled tank (Burton et al., 2012; Amundson et al., 2012; Cathles et al., 2015). During capsize of an analog iceberg, sensors located within the tank wall record time series describing the force and pressure changes generated by iceberg rotation and hydrodynamic effects (Figure 3.4; Cathles et al. 2015); an example of the tank setup is shown

in Figure 3.5. Gravitational energy released during calving is related to iceberg height, and force and pressure histories recorded in the lab can be scaled up to glacier dimensions using known relationships between the height of the analog iceberg used in the experiment and the height of icebergs observed in the field using high-frame-rate imagery (Burton et al., 2012; Amundson et al., 2012). Scaled-up laboratory force and pressure records predict well direct GPS observations of glacier deflection during iceberg calving (Figure 3.5A; Murray et al. 2015a). The experimental data thus appear to provide a robust analog with which to investigate details of the time-varying force generated during iceberg capsize, as well as the relationship between iceberg size and force magnitude.

The first ∼600 s of each horizontal-force history recorded during tank experiments consists of a gradual increase in up-glacier force amplitude followed by a more rapid decrease (grey-shaded portions of panels in Figure 3.4). This part of the force history is interpreted as the glacier response to seaward iceberg acceleration during capsize (Murray et al., 2015a).

Following the acceleration phase of the force history, each of the laboratory-derived horizontal-force histories contain a rapid force reversal to a down-glacier force lasting approximately 20 s ('b' in the upper left panel of Figure 3.4). We interpret this part of the force history as the glacier's response to rapid iceberg deceleration. This deceleration is likely driven by a combination of both reduced buoyancy force, as the iceberg nears horizontal and no longer has significant mass out of isostatic equilibrium in the water column, and the resisting force generated by water in the fjord slowing the iceberg's forward motion.

The force history seen in all laboratory experiments is evident in GPS data recorded at the calving front as well (Murray et al., 2015a). GPS instruments deployed on Helheim Glacier in East Greenland captured glacier motion during multiple buoyancy-

driven calving events in 2013 (Murray et al., 2015a). During each calving event, instruments located on ice within ∼1 km of the terminus recorded the front of the glacier being displaced ∼10 cm up-glacier for ∼300 s during the first stages of iceberg calving (Murray et al., 2015a). The glacier front then moves through and forward of its pre-event position before returning to equilibrium. The shape of these displacement records is in close agreement with the shape of horizontal-force records from the laboratory experiments (Figure 3.5A).

During the first ∼600 s of the tank time series, the pressure records are out of phase with the horizontal forces (grey-shaded portions of panels in Figure 3.4). After the horizontal force crosses zero, the pressure records become generally in phase with the horizontal force (Figure 3.4). A pressure decrease results in a vertical force on the solid Earth, oriented upwards. During the acceleration phase of the force history ('a' in the upper left panel of Figure 3.4), the up-glacier horizontal force combined with the negative pressure values result in an up-glacier, upward force acting on the glacier. This geometry is consistent with that estimated for the majority of the 450 glacial earthquakes that have occurred at 15 glaciers around Greenland over the last three decades. This suggests that this part of the tank force histories accurately represents the forces that generate the seismic signal. Following the up-glacier portion of the force history, the force and pressure histories transition to being in phase for the iceberg-deceleration portion of the time histories ('b' in the upper left panel of Figure 3.4).

In the ten laboratory force records we analyze in this study (Murray et al., 2015a; Cathles et al., 2015), as well as in GPS records from several calving events (Murray et al., 2015a), an up-glacier force is observed following the force reversal ('c' in the upper left panel of Figure 3.4). This up-glacier force is ∼10-s long and reaches between ∼30% and 100% of the amplitude of the preceding up-glacier force. During this time, laboratory force and pressure histories are in phase (white portion of panels in Figure

3.4), representing a force oriented upglacier and downward. Based on videos from the tank experiments (Cathles et al., 2015; Burton et al., 2012), we hypothesize that this part of the force history is generated by the iceberg rotating past horizontal so that the face of the iceberg that previously formed the iceberg's top surface is driven below the water surface, potentially coming in contact with the glacier's calving face. Such over rotation is also observed in some high-frame-rate images of buoyancy driven calving in the field (e.g., James et al., 2014). During this portion of the force history the laboratory experiments describe an up-glacier, downward force ('c' in the upper left panel of Figure 3.4). This force orientation is very rarely observed in CSF analysis of glacial-earthquake data, suggesting that this is not the part of the source that generates the main seismic signal.

The remainder of the horizontal force and pressure time series for a given tank experiment are in phase, and are not coherent between experiments. This final part of the time series is attributed to water waves oscillating in the experimental tank (Cathles et al., 2015; Burton et al., 2012). In the experimental set-up, measures are taken to damp seiche modes following iceberg capsize (e.g., Murray et al., 2015a), but waves are not fully eliminated. In glacier fjords, ice mélange serves to partially damp water waves (e.g., Amundson et al., 2010), and corresponding oscillations are not observed in glacier GPS data (Murray et al., 2015a).

In the following text we refer to the first ∼600 s of the source as the left-hand side, from first signal onset around $t = -600$ s to the time of the first zero crossing of the horizontal force (grey-shaded portions of panels in Figure 3.4). We refer to the time period beginning at the first force zero crossing and including the ∼20 s down-glacier force as well as the lower-amplitude up-glacier force that follows as the right-hand side of the source (white portions of panels in Figure 3.4).

Numerical-Modeling Results

Numerical simulations of iceberg capsize by Sergeant et al. (2018) produce horizontal force histories that share characteristics with both laboratory and field observations (Figure 3.5B). The model of Sergeant et al. (2018) is constructed using a 2D finite-element approach and includes an approximation of hydrodynamic drag forces. The model predicts the horizontal contact force between an iceberg and a glacier terminus from the time of rotation onset through the time the iceberg loses contact with the calving face. This is the portion of the seismic source understood to be generated by iceberg acceleration as an iceberg's center of mass moves away from the terminus during rotation. The duration of the iceberg-acceleration phase predicted by Sergeant et al. (2018) ranges from 100 – 200 s, and is controlled by both iceberg height and aspect ratio. The modeled force histories have similar characteristics to those of both laboratory and field observations, and consist of a gradual force increase followed by a rapid decrease to zero as the iceberg loses contact with the terminus. The force histories display a steeper slope as they approach peak force as aspect ratio increases (Figure 3.5B), an effect also seen in laboratory results (Figure 3.4). Because the model of Sergeant et al. (2018) describes force values only during the time the iceberg is in contact with the terminus, it does not capture the iceberg-deceleration phase of the source that is captured in laboratory and field observations. It therefore does not predict any down-glacier force and captures only the first half of the rapid force reversal seen in field and laboratory observations (Figure 3.5).

Limitations in Knowledge

While GPS observations, modeling results, and laboratory experiments provide important constraints on our understanding of iceberg calving, there are limitations to each. Laboratory experiments measure force and pressure only on the wall of the experimen-

tal tank that represents the calving face, and do not record data directly on the calving iceberg. GPS observations are limited to the glacier surface close to the terminus, but do not include data directly from the calving face. Numerical experiments only detail iceberg rotation through the time of loss of contact, and so do not describe forces active during the full rotation of the iceberg. No observations exist from the rest of the system (e.g., fjord walls, ice mélange, etc.) which hinders comprehensive understanding of calving.

Details of the force history after the time of force reversal (e.g., the 'right-hand side' of the force history) are particularly poorly constrained, which makes description of the right-hand side of the source function challenging. Glacier displacement records recorded by on-ice GPS (Murray et al., 2015a) become difficult to interpret after the rapid force reversal, in part due to glacier acceleration immediately following buoyancy-driven calving (Nettles et al., 2008). Laboratory records become less coherent after the iceberg first reaches horizontal due to water waves in the tank. It is likely that momentum is transferred to the tsunami that propagates away from the calving front following glacial earthquakes, but investigation of that phenomenon is beyond the scope of this study.

3.3 Methods

3.3.1 Construction of Synthetic Seismograms

We generate synthetic seismograms using force and pressure histories recorded during a set of ten analog experiments of bottom-out iceberg capsize performed by Cathles et al. (2015) and Murray et al. (2015a) (Figure 3.4). Bottom-out iceberg capsize is the most commonly observed geometry for buoyancy-driven calving, and the only kind of calving for which robust on-ice displacement records exist (Murray et al., 2015a). In

analog tank experiments, bottom-out capsize occurs spontaneously when a tall, narrow plastic iceberg is placed vertically within the water against one end of the tank. By contrast, top-out capsize occurs in the laboratory only when an initial angle of rotation for the iceberg is enforced. We consider only bottom-out calving events in this study.

We investigate calving of icebergs with aspect ratios of 0.22, 0.28, 0.43, and 0.54. Laboratory results were scaled up to glacier dimensions (Burton et al., 2012; Murray et al., 2015a) to achieve iceberg dimensions consistent with field observations of buoyancy-driven calving in Greenland. The scaled-up heights of the icebergs range from 741 - 1000 m, cross-glacier lengths range from 2360 - 3000 m, and along-glacier widths range from $\sim$160 – 430 m, consistent with observed dimensions of icebergs from Jakobshavn Isbræ and Helheim Glacier (e.g., Murray et al., 2015c; James et al., 2014; Walter et al., 2012). Two to four different iceberg sizes are considered for each aspect ratio.

We smooth the force and pressure data collected in the laboratory experiments using a 5-s moving average to remove high-frequency instrument noise, and remove the mean background signal using 350 s of each record before signal onset. To convert pressure records to vertical-force values we multiply each pressure time series by the basal area of the unrotated iceberg used for each experiment. Clearly, this conversion will represent a simplification compared to the true ice-water-rock system.

In all experiments, $t = 0$ is defined as the time at which the capsizing iceberg first reaches horizontal. To generate each seismic source we trim the records to begin at $t = -600$ s, which is the approximate time at which the signal first deviates from zero. Following iceberg capsize, water waves oscillate in the tank and dominate both force and pressure records to an extent not expected in the field due to damping from ice mélange (e.g., Amundson et al., 2010). We trim the right side of each record to $t = +50$ s, which allows us to include source signal consistent in character across experiments,

while omitting the majority of later water-driven oscillations.

To construct the synthetic seismograms, we parameterize the shape of each horizontal and vertical input force independently using a set of isosceles triangles with durations of 10 s, fixed to overlap one another by 50%. We specify an initial westward orientation for all horizontal forces, and an initial upwards orientation for all vertical forces, consistent with the typical orientation of observed glacial-earthquake forces at Helheim Glacier. Seismograms are calculated using normal-mode summation in the preliminary reference Earth model (PREM; Dziewoński and Anderson, 1981) to a minimum period of 30 s. The horizontal and vertical force functions are included as the term $S(t)$ in the ground-motion equation. Seismograms are calculated for a synthetic array of eleven stations located at epicentral distances between 10 and 70° from the source and equally spaced 30° apart in azimuth. The station distribution is chosen to represent the limited range of observing distances and azimuths available for analysis of glacial earthquakes at Greenland glaciers. In this proof-of-concept study, we restrict our analysis to noise-free synthetic seismograms.

3.3.2 Construction of Force-History Models

We construct a set of models of the earthquake force history of varying degrees of complexity. We construct boxcar-shaped models by specifying the duration of the source and that the force histories integrate to zero, the same technique employed in previous glacial-earthquake analysis (Tsai and Ekström, 2007; Veitch and Nettles, 2012; Olsen and Nettles, 2017). We perform experiments using boxcar models with 50-s durations like those employed in previous studies (Figure 3.2), as well as experiments using boxcar models with full durations ranging from 10 s to 600 s.

We construct a second set of models using simplified representations of the shape of the force histories recorded in laboratory experiments and refer to this family of models

as Fixed Source Time Function (FSTF) models. The inversion technique is identical to that employed with boxcar force models, with the sole difference being the use of a more complex force history. We represent the force-history shape in the FSTF models using a series of isosceles triangles that overlap by 50%. All triangles have the same duration, and relative amplitudes of the triangular sub-sources are fixed throughout the inversion so that the input force shape is maintained.

GPS observations, laboratory observations, and numerical-modeling results are in general agreement on the shape and duration of the left-hand side of the glacial-earthquake source. We therefore construct the left-hand side of the majority of the models we use in this study based on these constraints. A second robust feature observed in all three non-seismic datasets is the rapid force reversal from up- to down-glacier orientation. Because seismic waves are efficiently generated by rapid force changes, this feature is the most likely source of glacial-earthquake energy seen in the portion of the source constrained by these datasets. We include a rapid force reversal in the majority of models tested in this study, and note that the success of the simple 50-s boxcar model likely stems from the fact that it too captures a rapid reversal in force orientation. Additionally, GPS observations and laboratory results both have horizontal and vertical force histories with generally similar shapes through the time of the rapid force reversal. We therefore simplify construction of models in this study by specifying that the vertical and horizontal force functions have the same shape in all boxcar and FSTF models.

We refer to the three FSTF models we discuss in detail as Models A, B, and C. We construct the left-hand sides of all three models identically, using an average shape from the tank-derived force histories. This average is calculated by normalizing the horizontal force histories recorded in eight of the tank experiments (two for each of the four aspect ratios considered) and aligning them on the first zero-crossing time of the

force history (approximately $t = -20$ s). We then calculate the average of these time series between $t = -600$ and 50 s.

The right-hand side of Model A is constructed to include the rapid force reversal and ∼20 s down-glacier force taken from the tank-averaged time series. Model A does not integrate to zero (Figure 3.6). The left-hand side of Model B is constructed using the tank-average shape as described above, and the right-hand-side is constructed as a triangle with area equal to that of the left-hand side. The maximum force on the right-hand side of Model B is one half the value of the maximum force on the left-hand side (Figure 3.6). Model C is constructed in the same way as Model B, with the difference that the right-hand-side triangle has a maximum-force amplitude twice that of the maximum-force amplitude on the left-hand side (Figure 3.6). Models B and C integrate to zero.

We also perform inversions in which we estimate the source time function using a technique developed for modeling seismic signals generated by landslides (Ekström and Stark, 2013), and which we refer to as the Landslide Force History (LFH) technique. In these inversions we restrict the force function to consist of a small number (4 – 8) of isosceles triangles overlapping by 50%. We solve for the amplitude of each triangular sub-source, and allow horizontal and vertical forces to vary independently. To minimize oscillation in the force functions we apply a weak smoothing constraint to these models. The force histories are constrained to integrate to zero.

3.3.3 Inversion Procedure

We bandpass filter the synthetic seismograms calculated in section 3.3.1, transformed to ground velocity, to the period band 50 – 150 s, consistent with standard analysis of glacial earthquakes. We invert each set of input seismograms using the analysis approach employed in previous glacial-earthquake studies (e.g., Tsai and Ekström, 2007;

Veitch and Nettles, 2012; Olsen and Nettles, 2017). Wave propagation is calculated using PREM (Dziewoński and Anderson, 1981). Inversion outputs are assessed using standard criteria including the fit to the data, inversion stability, recovery of input geometry, time shift, and location.

Several measures of earthquake size are evaluated for each event. Because the tank-derived force histories we use to generate the synthetic seismograms do not integrate to zero, a zero-frequency M_{CSF} value is not recovered. This arises from the fact that for the tank-derived force histories the once-integrated force function with respect to time, the impulse function, is not symmetric (Figure 3.2). For the same reason, the twice-integrated force function does not converge to a constant value as it does with force functions that integrate to zero. We choose to evaluate the impulse function and the twice-integrated source function at the same point in time, when the impulse function reaches its maximum value, which occurs at the time of the first zero crossing of the horizontal force (Figures 3.2, 3.7). We refer to the value of the twice-integrated force function, reported at the time of maximum impulse (Figure 3.2f), as M^{*}_{CSF} to distinguish it from the zero-frequency M_{CSF} value recovered using boxcar and LFH source models (Figure 3.2c). Because of these differences in the once- and twice-integrated values reported in this study versus previous studies, we also consider a third metric for glacial-earthquake size, maximum force, defined as the maximum absolute value of the force history.

3.4 Results

Inversions conducted using a 50-s boxcar-shaped source model return maximum-force values between 0.25 and 0.33 of the true maximum-force values of the input source (Figure 3.8). The corresponding maximum impulse and twice-integrated force history values returned by the model are ∼0.05–0.01 those of the true values, primarily because

the duration of this model is less than 10% that of the input source. The 50-s boxcar model produces very good fits to the tank-derived waveforms, with misfit values of approximately 0.2 (Figure 3.8e).

All three of the tank-derived models, Models A, B, and C, recover the maximum-force value to within 50% of the input value (Figure 3.8a). Model C most closely reproduces input maximum-force values, to within 20% of true values, for the ten experiments presented in this study.

The best recovery of maximum impulse and M_{CSF} values is achieved using models A and C. For experiments using icebergs with aspect ratios of 0.22 or 0.28, Model C underestimates maximum impulse values by an average of 44% and overestimates the maximum impulse values of experiments with aspect ratios of 0.43 and 0.54 by 3% and ∼25%, respectively. For experiments using icebergs with aspect ratios of 0.22 or 0.28, Model A underestimates maximum impulse values by an average of 43%, and overestimates the maximum impulse values of experiments with aspect ratios of 0.43 and 0.54 by 1% and 25%, respectively. A similar aspect-ratio dependence is observed in the M^*_{CSF} values for both Models A and C. Model B overpredicts maximum-impulse values, especially at larger aspect ratios, and overpredicts M_{CSF} values by factors of >2 – 8.

Experiments using Models A and C produce low misfit values, with model seismograms that fit the input seismograms well. Experiments using Model A produce an average misfit value of 0.15, with misfit values ranging from 0.05 – 0.25. The average misfit value for experiments using Model C is 0.17, with misfit values ranging from 0.06 – 0.32. Waveforms generated using Model B are longer period than input seismograms, and the poorer fit to data is reflected in misfit values between 0.44 and 0.76.

A 50-s LFH force model constructed using four overlapping isosceles triangles with half durations of 10 s each returns maximum-force values between 0.5 and 0.7 of the

maximum input force (Figure 3.8a). Impulse and M_{CSF} values recovered by this model are >1% of input values. The LFH force model explains the data less well than the FSTF models do, and misfit values using this model are between 0.18 and 0.4.

Input force azimuths are very well recovered by all models tested, never deviating from the input values by more than 1° (Figure 3.8d). By convention, the force azimuth reported is the force orientation of the first part of the force history (during the iceberg-acceleration phase of the source). Event locations are also recovered well by all models: latitude values are recovered to within 2 km, and longitude values to within 8 km. The plunge of the input model varies with time, while the inversion procedure for CSF and FSTF models estimates a single value. Therefore, we do not directly compare input and recovered plunge values, but instead note that the shallow plunge values recovered by all FSTF and CSF models in this study ($0 - 36°$) are consistent with the majority of plunge values during the left-hand side of the force history, as well as with the plunge values in the glacial-earthquake catalog (Tsai and Ekström, 2007; Veitch and Nettles, 2012; Olsen and Nettles, 2017).

3.5 Discussion

Although the boxcar model underpredicts M_{CSF} values, maximum-force values are surprisingly well recovered, and, encouragingly, the underprediction is by a nearly constant value, across iceberg mass and aspect ratio. Recovery of all seismic-magnitude metrics is improved with the LFH and tank-derived models. Model C appears to be the best choice among the models tested, due to its low misfit values and ability to recover input maximum-force and orientation values robustly. In this section, we consider model characteristics that control successful recovery of input values, and test the FSTF approach on real data. We explore the relationship between maximum-force values and iceberg size, and discuss future work needed to construct a scaling relationship.

3.5.1 Key Components of an Improved Source Model

In order to evaluate the characteristics needed for a simple but useful representation of the glacial-earthquake source, we consider features that control how well source parameters are recovered. Given the long (hundreds of seconds) force histories of the laboratory, field, and numerical constraints, it is surprising that the 50-s boxcar model recovers source parameters as well as it does, despite having a duration $< 10\%$ that of the synthetic sources we test and a symmetric shape. It is likely that the boxcar model works well because it contains a rapid force reversal that is similar to that contained in the synthetic sources. Indeed, the boxcar model's short duration means that it overlaps only with the portion of the source function dominated by the rapid force reversal (Figure 3.9a). The similarity of the shape of the force reversal across all ten laboratory experiments likely explains why the misfit values for all experiments using a boxcar model are similarly low, around 0.2 (Figure 3.8e), and why the boxcar model works well with real data.

As with the boxcar models, the key feature controlling the ability of FSTF models to recover accurate estimates of input data appears to be the presence of a rapid force reversal. Models A and C have the largest peak-to-peak force reversal across the same duration, and these two models do a better job recovering seismic estimates of size than Model B (Figure 3.8a – c), which has a peak-to-peak amplitude that is half that of Model C over the same interval (Figure 3.9). We construct an additional 16 FSTF models to thoroughly investigate the effect of model shape on input-value recovery, and find that models which lack a steep force reversal and instead reverse force orientation over a longer time interval have high misfits and poor recovery of input parameters. For example, a sine-wave model with a wavelength of 200 s returns synthetic seismograms that fit the input data poorly, poorly recover maximum-force values, and produces misfit values around 0.9. All models we construct with a rapid force reversal recover

input parameters more accurately.

In addition to a rapid force reversal, the shapes of the left- and right-hand sides of the FSTF models appear to play a role in the recovery of input parameters. As expected, models informed by the shape of the input source, such as Models A, B, and C, do a better job recovering input parameters than the boxcar model. We find that models constructed using the tank-average shape for the left-hand side of the source do a better job of recovering input parameters than do FSTF models with similar durations that use the simpler approximation of constructing the left-hand side of the source out of a single right triangle.

We find very poor fits to the seismograms using an FSTF model constructed using the tank-average left-hand-side but that stops at the first zero crossing of the force, entirely omitting the right-hand side. This suggests that information contained in the force history after the first zero crossing plays an important role in seismic-signal generation in the frequency band of interest.

However, models with right-hand-side durations equal to or greater than the left-hand side, like Model B (Figure 3.6), also result in poor fits to the data. We find that a model similar to Model B, but with a much shorter right-hand-side duration (100 s, as opposed to $\sim$800 s; not shown here), has lower misfit values than Model B and more accurately recovers maximum-force values. Model C, which captures the high-amplitude force reversal and has a right-hand duration of 200 s, provides the best fit to data of the $\sim$20 models we test.

The FSTF models recover seismic-magnitude values significantly better than the boxcar model does, despite the fact that waveform fits are comparable between the two types of models (Figure 3.10). This result highlights a limitation of the long-period seismic data: the data are insufficiently sensitive to the shape of the source function to discriminate one source function from another based on waveform fits alone, as

previously recognized by Tsai et al. (2008). However, our results demonstrate that including knowledge of the source shape derived from other datasets can markedly improve recovery of glacial-earthquake magnitude parameters.

3.5.2 Limitations on Direct Inversion for Force History

In addition to experiments using the fixed model shapes of the boxcar model and the suite of FSTF models, we experiment with using a simple version of the Landslide-Force-History technique to invert directly for the shape of the glacial-earthquake force function. We find that a simple 50-s LFH model with four sub-sources overlapping by 50% reproduces the input force to within 50% (Figure 3.8e). Misfits for these experiments are higher than those using a boxcar model, but are within the range found for published glacial earthquakes. Extending the duration of the four sub-sources to 40 s, resulting in a full source duration of 100 s, produces maximum-force values similar to results using a 50-s LFH model, and similar fits to data. However, all evidence points to a source function that is significantly longer than 100 s, yet experiments that further lengthen the duration of each sub-source lead to poor parameter recovery and high misfits. This is likely due to the fact that a rapid force reversal is not captured by an LFH source when long-duration sub-sources ($\geq$50 s) are used. We also experiment with increasing the number of shorter-duration (10 - 20 s) sub-sources as an alternative way to increase the full source duration. However, higher numbers of sub-sources lead to force histories that contain multiple rapid force oscillations which are inconsistent with our knowledge of the left-hand side of the source. In addition, these experiments frequently return down-glacier force orientations, 180° from the input orientation.

We perform a set of experiments using a suite of LFH models with different durations to invert ten glacial earthquakes that occurred at Helheim Glacier and Jakobshavn Isbræ. We construct the models to have full durations between 40 and 80 s, using four

to eight overlapping sub-sources. We find high misfit values (0.4 – 0.8) using the model with 40 s durations, and force histories that oscillate in what we believe to be a non-physical way for many of the glacial earthquakes using the 70- and 80-s models, similar to the behavior we observe in the experiments using synthetic data.

We conclude that the available seismic data are not sufficient to constrain the shape of the glacial-earthquake source function on their own. While the LFH-modeling technique has proven successful with landslide data (Ekström and Stark, 2013), glacial-earthquake data constraints are poorer, due in part to longer source-to-station distances for glacial earthquakes and poorer azimuthal station coverage. Our experiments using synthetic data show that even with a uniform azimuthal distribution of stations at teleseismic distances similar to those used in glacial-earthquake analysis, the LFH technique is unable to robustly reproduce the duration or maximum-force amplitudes of input glacial-earthquake force histories.

Sergeant et al. (2016) have also addressed the question of solving directly for the force history of a glacial earthquake. They use a deconvolution technique to attempt to recover the source function from displacement seismograms. However, the force histories they recover contain rapid oscillations in both the horizontal and vertical forces, which are not observed in any of the independent constraints on the shape of the force history from laboratory or field observations. These rapid force oscillations have no physical basis, and we therefore do not consider these results to be accurate representations of glacial-earthquake force histories.

While ideally we could obtain a description of the full force history directly, neither the LFH approach nor the approach of Sergeant et al. (2016) produces results we deem satisfactory. In addition to challenges to analyzing real glacial earthquakes due to non-uniform station coverage and large source-to-station distances, the seismic data are only weakly sensitive to the low-amplitude, long-period part of the signal used in

determining the character of the source. Because of these limitations, we turn to the FSTF approach as a simple path forward for improving source-parameter estimates.

3.5.3 Maximum Force as a Preferred Metric of Glacial-Earthquake Size

Because of its integrated nature, estimated M_{CSF} values are highly sensitive to the shape and duration of the specified force-time function. As long as the true duration and shape of a glacial-earthquake source function are unknown, serious limitations exist in the use of the M_{CSF} metric and its interpretation. However, our experiments show that the value of the maximum force acting during a glacial earthquake can be recovered robustly. For this reason, we suggest that the maximum force provides a better, simple measure of glacial-earthquake size than the M_{CSF} value that has been reported to date in the glacial-earthquake literature (Tsai and Ekström, 2007; Veitch and Nettles, 2012; Olsen and Nettles, 2017, 2019). The recovered maximum-force value is far less sensitive to assumptions about the force-time history than is the M_{CSF} value.

For the majority of sources, the maximum-force value occurs at the end of the rapid force reversal (Figure 3.4), when the force is oriented downglacier. The exceptions are the two laboratory experiments conducted using icebergs with aspect ratios of 0.22 (Experiments 1 and 2), in which the maximum-force values occur at the beginning of the rapid force reversal, with the force oriented upglacier. In experiments involving icebergs with aspect ratios of 0.43 and 0.54, the peak downglacier force has an amplitude approximately double that of the peak upglacier force, whereas in the experiments with smaller aspect ratios the peak up and downglacier force amplitudes are approximately equal. Therefore, a model's success in recovering maximum-force values lies partly in its ability to capture the peak force value that occurs as part of the rapid force reversal.

Sergeant et al. (2019) also consider the maximum force generated during a rota-

tional calving event, and discuss advantages to this size metric as opposed to M_{CSF}. However, they calculate maximum-force values using a force model that describes only the acceleration-phase of iceberg capsize, and does not include the iceberg deceleration phase of the force history. Because 8 out of 10 of the laboratory experiments we consider in this study have maximum-force values at the end of the rapid force reversal, with the force oriented downglacier, we believe this portion of the force history is necessary to include for accurate description of maximum glacial-earthquake force values. The technique of Sergeant et al. (2019) relies on fitting a force time series deconvolved from ground-motion seismograms to a catalog of modeled force histories that have been bandpass filtered. Because this technique omits the deceleration phase of the force history, bias may be introduced in maximum-force estimates if the deceleration phase of the source contributes to the seismic signal, which we believe it does. We therefore favor the FSTF technique for estimating maximum force, using a model that represent both the acceleration and deceleration phases of the seismic source function.

All evidence points to a true glacial-earthquake source duration longer than 50 s, which means that the M_{CSF} values reported in the glacial-earthquake literature likely underestimate true M_{CSF} values. Our experiments with synthetic data demonstrate that M_{CSF} values recovered using the 50-s boxcar model underestimate the twice-integrated force function values by approximately an order of magnitude. However, maximum-force values can be calculated from the M_{CSF} values estimated in previous studies using a boxcar-shaped model (Tsai and Ekström, 2007; Veitch and Nettles, 2012; Olsen and Nettles, 2017) in a straightforward manner; our results suggest that multiplication of these maximum-force values by a factor of 3-4 would bring them close to the likely true values. As expected, these peak force values, generated primarily by horizontal acceleration of the iceberg mass during capsize, are smaller than peak force values expected for acceleration due to gravity, suggesting that peak force values

calculated from M_{CSF} values are within a realistic range. These peak force values are also within the range of force values retrieved for landslides with similar masses (Ekström and Stark, 2013).

3.5.4 Relationship between Maximum Force and Iceberg Mass, Revisited

All three measures of glacial-earthquake size that we consider, maximum force, maximum impulse, and M^*_{CSF}, read from the force histories of the 10 tank experiments discussed in this study, correlate with iceberg mass (grey squares in Figure 3.11). Slightly different trends are observed for laboratory experiments with different aspect ratios, however the dominant relationship in all cases is an increase in each of the three seismic-magnitude parameters with increasing iceberg size. Analog icebergs with aspect ratios of 0.22 and 0.28 demonstrate a slightly different trend than those with aspect ratios of 0.43 and 0.54 (Figure 3.11a), due to the higher peak amplitudes of the down-glacier force recorded in experiments with larger aspect ratios, compared to those with smaller aspect ratios (Figure 3.4).

Like the direct observations of force from the tank experiments, the seismic-magnitude values recovered using all five of the models discussed in detail in this study correlate positively with iceberg mass (Figure 3.11). Models A, B, and C do a better job capturing the relationship between iceberg mass and maximum force than does the boxcar model, and the FSTF models also do a fairly good job capturing the relationship between iceberg mass and maximum impulse (Figure 3.11b).

Improved recovery of all three seismic-magnitude metrics by Models A and C (Figures 3.8, 3.11) is encouraging, and suggests the potential utility of reanalyzing glacial-earthquake data using a more-sophisticated model. We use Model C in an FSTF analysis of twelve glacial earthquakes previously analyzed using the 50-s boxcar model

(these events are shown as circles and squares in Figure 3.1) to test the approach. As for the results with the boxcar model, we recover maximum-force values that are positively correlated with iceberg mass (Figure 3.12). As expected from our synthetic experiments, maximum-force values recovered using Model C are higher than those calculated for the same events using the boxcar model. The values for the real earthquakes obtained using Model C occupy approximately the same space in the maximum-force vs. mass diagram as the values from the tank experiments, suggesting that the values are likely to be realistic.

The seismically recovered maximum-force values for a number of landslides (Ekström and Stark, 2013; Hibert et al., 2014, 2015) are approximately an order of magnitude larger than maximum-force values recovered for glacial earthquakes with similar masses (Figure 3.12), and than the values for the scaled-up tank experiments. Data constraints are better for landslides, and as expected less scatter is seen in these data. Assuming mass remains constant throughout the duration of an iceberg-calving event or a landslide, acceleration values for glacial earthquakes and landslides can be compared by dividing the maximum force of each event by its mass. Landslide acceleration values are $\sim$2 m/s^2, whereas the maximum acceleration values for icebergs, estimated using Model C, are an order of magnitude lower, ranging from 0.21 – 0.38 m/s^2. The lower values for icebergs may be due to hydrodynamic effects of water interacting with the iceberg while it rotates, limiting iceberg acceleration. Obtaining greater accuracy in such estimates would provide important, quantitative constraints on the physics of the calving process.

Sergeant et al. (2019) use a different approach to investigate the relationship between seismic magnitude and iceberg size. They estimate force histories using a deconvolution technique, and compare them to numerically modeled force histories for capsize of a range of iceberg sizes. By performing a grid search over possible modeled

force histories, they identify the height and iceberg aspect ratio of the model that most closely fits the data. They then consider a range of plausible iceberg cross-flow-length values and calculate an average volume estimate for a single iceberg. The iceberg volumes estimated using this technique come from model results; Sergeant et al. (2019) do not have independent estimates of iceberg size. Whereas we observe only a minor dependence of seismic-magnitude parameters on iceberg aspect ratio, a clear aspect-ratio dependence is observed in the relationship reported by Sergeant et al. (2019) between maximum force and model predictions of iceberg size. We discuss the need for further exploration of aspect-ratio dependence in the following section.

3.5.5 Current Limitations and Future Outlook

Refining the models presented here and ultimately constructing an optimized source model to use in glacial-earthquake analysis moving forward will require both further experimentation with seismic data and the collection of additional non-seismic information to elucidate the full nature of the seismic source. Uncertainty regarding the character of the right-hand side of the source is currently a key limitation, and further observations of calving in the laboratory and the field are needed to clarify the character of this deceleration phase.

Future synthetic tests should incorporate realistic approximations of seismic noise and investigate the effect this has on source-parameter recovery. We anticipate the effect of noise will be small, however, based on synthetic experiments we perform to test the effect of un-modeled Earth structure on parameter recovery. Using different Earth models for synthetic seismogram generation and waveform modeling produces a larger discrepancy between input and output seismograms than the addition of seismic noise is expected to have. Nevertheless, the use of two different Earth models has only a minor effect on azimuthal values, on the order of 3°, and affects plunge values by a

similarly small amount ($\sim 5^{\circ}$). Location perturbations resulting from addition of unmodeled Earth structure are within the location uncertainties when using long-period data.

The role aspect ratios play in determining the shape of force histories is also worth exploring further. Laboratory experiments show minor differences in force shape for icebergs with aspect ratios between 0.22 and 0.54. Because the aspect ratios of the icebergs that generate glacial earthquakes is rarely known, routine estimation of source parameters requires a model capable of recovering source parameters for icebergs with a range of aspect ratios. Additional laboratory experiments exploring a larger range of aspect ratios are needed to quantify the effect this variable has on recovery of source parameters.

The force histories of top-out calving events should also be considered in future work. Like aspect ratio, the rotation direction of a calving iceberg has an effect on the shape of the force histories recorded in laboratory experiments. Though top-out buoyancy-driven calving is observed in the field less frequently than bottom-out calving, investigation into the ability of an FSTF model based on bottom-out calving to recover source parameters for a top-out calving event is needed to fully quantify the range of parameter uncertainties involved with using the FSTF technique.

Future work should also investigate the effect of using models with different shapes for the horizontal and vertical force histories generated by a calving iceberg. Constructing a model for the vertical force history using pressure records from laboratory experiments, converted to vertical force, may improve source-parameter recovery. This may be especially helpful in modeling the deceleration phase of glacial earthquakes, as both field observations of glacial earthquakes (Murray et al., 2015a) and tank force histories (Cathles et al., 2015) show that the vertical- and horizontal-force histories differ in shape most notably after the rapid force reversal.

Known relationships between scalar moment and earthquake source duration are used to choose time functions for CMT analysis of tectonic earthquakes (Ekström and Nettles, 2014), and may aid in modeling of glacial earthquakes, particularly in light of the range of iceberg sizes now known to generate glacial earthquakes (Olsen and Nettles, 2019). To explore this possibility, additional investigation into the effect of scaling the shape or duration of an FSTF model based on initial estimates of glacial-earthquake size is needed.

3.6 Conclusions

In this study, we have explored the feasibility of improving estimates of glacial-earthquake source parameters through incorporation of improved knowledge of the earthquake force-time function. In particular, we explore the utility of replacing the boxcar-shaped function used in much previous work (Tsai and Ekström, 2007; Veitch and Nettles, 2012; Olsen and Nettles, 2017, 2019) with a more sophisticated time function based on knowledge obtained from laboratory, field, and numerical-modeling studies (Cathles et al., 2015; Murray et al., 2015a; Sergeant et al., 2018).

We demonstrate that, even without a full physical description of the glacial-earthquake source, estimates of source parameters can be obtained by this straightforward extension of the centroid-single-force modeling approach. We find that the rapid force reversal, from upglacier to downglacier, is the most important feature for a force-time model to include; this finding likely explains the success of the boxcar model used in earlier studies. Previous modeling work (Sergeant et al., 2018) focused exclusively on the acceleration phase of the glacial-earthquake source, however we find that the deceleration phase of the source function also plays a role in generating waveforms that has not previously been appreciated.

Our preferred model, Model C, captures the gradual force onset observed in the

acceleration phase of the laboratory experiments we investigate. It contains the rapid force reversal from up to downglacier, and contains a ∼200 s deceleration phase. Model C recovers well source parameters for icebergs with a range of aspect ratios, which is important given our limited knowledge of the true aspect ratios of capsizing icebergs. Moving forward, key areas to explore with this model include the forces generated by icebergs that rotate top-out during calving, and the incorporation of different force histories for vertical and horizontal forces.

The waveform-modeling approach we apply in this study is simple, computationally efficient, and returns robust estimates of source parameters despite the data-quality limitations inherent to work with glacial earthquakes. By incorporating non-seismic constraints on the shape of the force history, we overcome limitations associated with the sensitivity of seismic data and produce better recovery of seismic-magnitude values.

Using a set of experiments on synthetic seismograms, we demonstrate that the maximum force generated by a calving iceberg can be more accurately retrieved than the twice-integrated force value, M_{CSF}. We therefore prefer maximum force as a seismically derived measure of glacial-earthquake size because it is a simple metric that is far less sensitive to modeling choices than integrated measures. We find that maximum-force values associated with the M_{CSF} values reported for the events in the published glacial-earthquake catalog likely underpredict true maximum-force values for these events by a factor of 3–4 due to the short duration and fixed shape of the 50-s boxcar model used, but that the underprediction is nearly constant across iceberg mass and aspect ratio.

Our results help clarify the relationship between iceberg mass and seismic observables, moving us closer to the use of glacial-earthquake data as a geophysical tool for mass-loss estimation. Maximum-force values for glacial earthquakes derived using our preferred simple model of the earthquake source are approximately an order of magnitude smaller than those generated by landslides of comparable mass (Ekström

and Stark, 2013), suggesting the potential utility of further comparison between these two phenomena, and the opportunity to gain additional insight into the physics of the calving process.

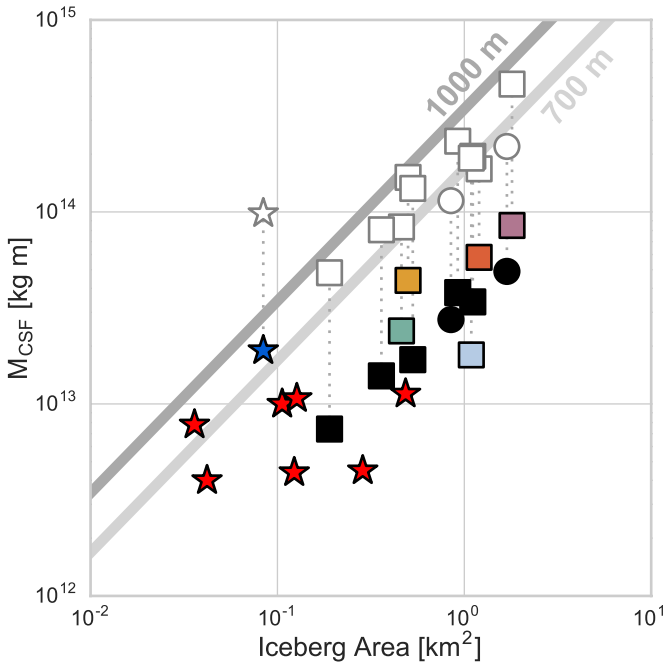

Figure 3.1: Comparison between M_{CSF} and iceberg surface area, updated from Olsen and Nettles (2019). Multicolored and black symbols represent glacial earthquakes at Jakobshavn Isbræ and Helheim Glacier, modeled using a 50-s boxcar time function. Event details for multicolored symbols are given in Figure 9 of Chapter 2 and Olsen and Nettles (2019). Black symbols represent calving events at Helheim Glacier, newly analyzed in this study using a 50-s boxcar time function. These events are reported in Murray et al. (2015c), and iceberg area estimates are courtesy of Timothy James. From left to right in the figure, the dates and times of the events represented by black symbols are: 2013/7/26 01:43; 2013/05/25 13:03; 2013/08/08 06:50; summed M_{CSF} and iceberg area from two events: 2013/07/24 19:37 and 19:39; 2013/07/25 12:56; 2013/07/30 20:01; summed M_{CSF} and iceberg area from two events: 2013/08/14 23:41 and 23:50. Grey lines represent values expected from a simple model of the relationship between iceberg area and M_{CSF} in which iceberg aspect ratio is 0.25 and iceberg height is fixed at either 1,000 m (dark grey) or 700 m (light grey), as described in Section 5.5 of Chapter 2 and Olsen and Nettles (2019). White symbols represent the predicted M_{CSF} values for each large glacial earthquake according to the simple model and given the observed iceberg dimensions for each event. White symbols are not presented for the events represented by red stars because these are very small glacial earthquakes for which signal-to-noise ratios are lower than for standard glacial earthquakes and M_{CSF} estimates may be less robust.

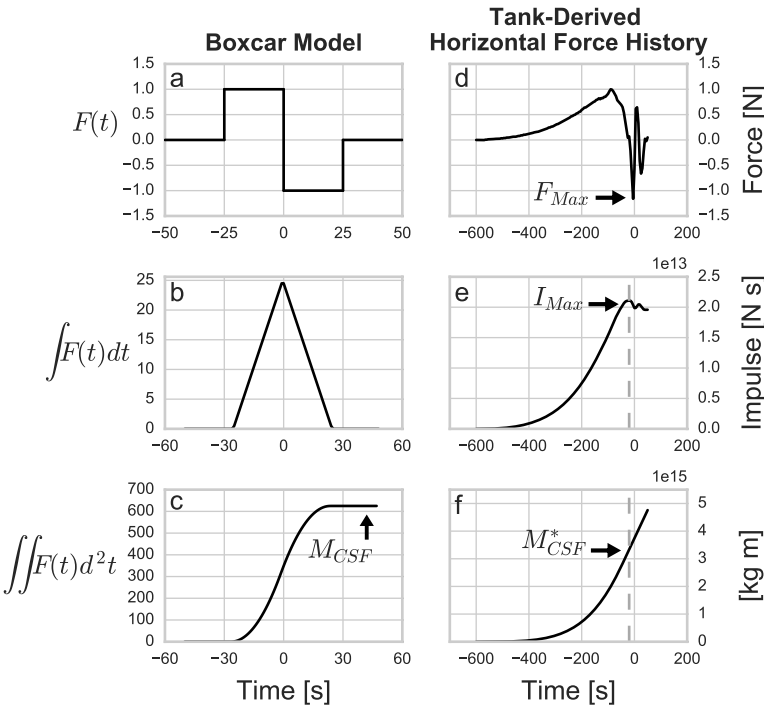

Figure 3.2: Force histories and integrated quantities for (a) the 50-s boxcar model and (d) laboratory experiment Source 5 of Figure 3.4. The first row in each column shows force histories. F_{Max} in panel (d) identifies the maximum force for this particular force history. The second row in each column shows the integral with respect to time of each force history (the impulse history). In panel (e) the time of the maximum impulse value (I_{Max}) for this particular force history is identified by the grey dashed line. For the boxcar model, the maximum impulse value occurs at $t = 0$. The third row shows the second integral with respect to time of each force history. For the boxcar model, the twice-integrated force history reaches its final value at $t = 25$ s and then remains constant; this constant value is referred to as M_{CSF} in glacial-earthquake literature. For the tank-derived force history, which does not integrate to zero, we in this study evaluate the twice-integrated force history at the time of the maximum impulse value, denoted by the grey dashed line, and refer to this value as M^*_{CSF}.

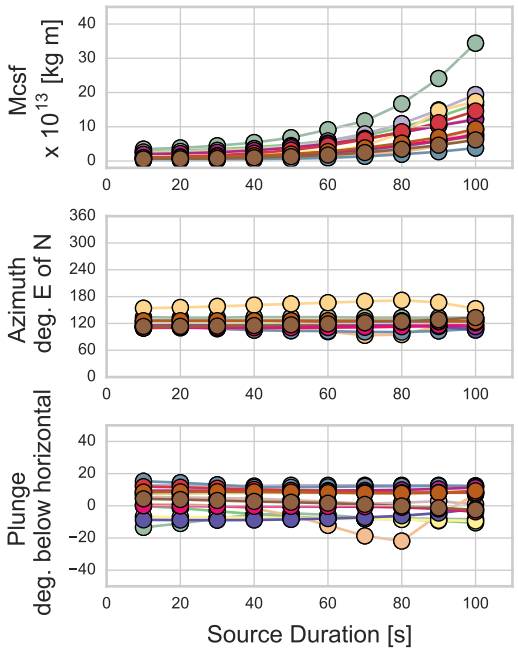

Figure 3.3: Source parameters for 15 glacial earthquakes estimated using boxcar models with source durations from 10 – 100 s. Each set of connected colored points represents results from a different glacial-earthquake event, modeled using increasing source durations. Top panel shows magnitude results (M_{CSF}) for each experiment, second and third panels show results for the orientation of each glacial-earthquake force in the horizontal (azimuth) and vertical (plunge) planes.

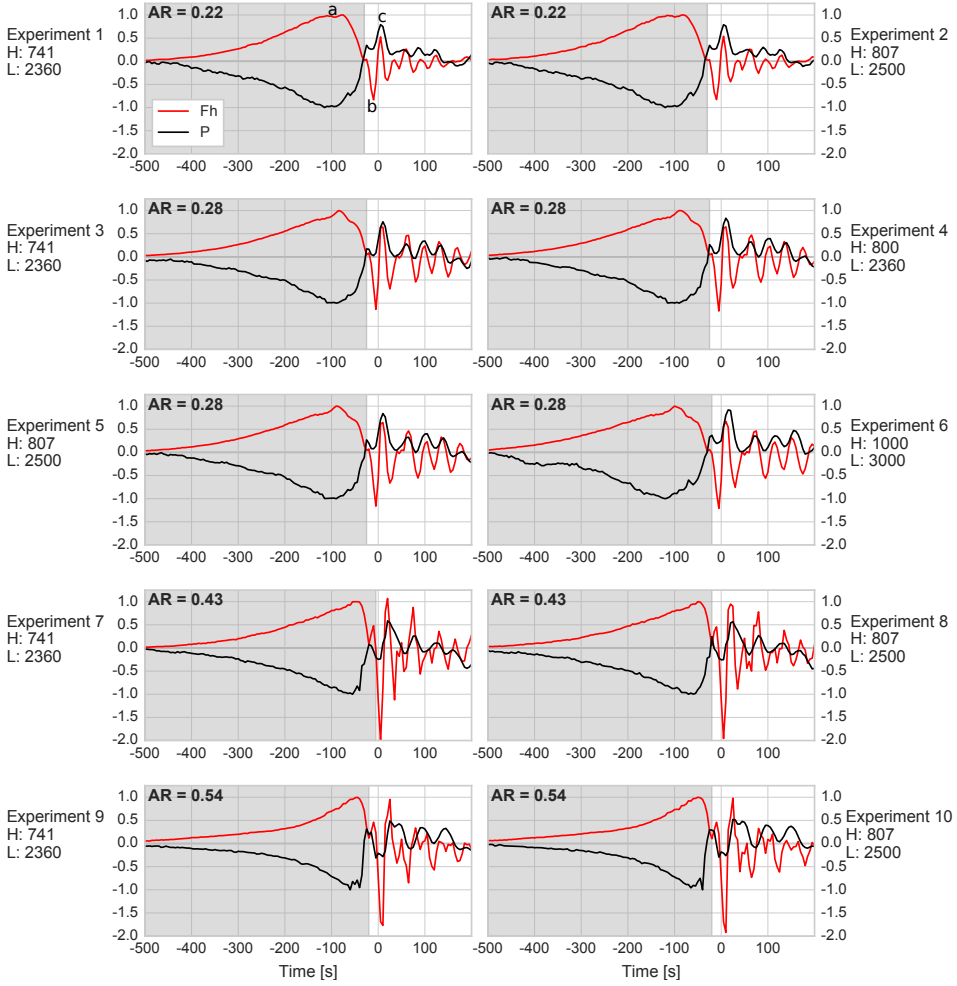

Figure 3.4: Normalized (red) horizontal-force and (black) pressure histories for the ten laboratory experiments used as seismic sources in this study. Grey shading identifies the part of the time series referred to in the text as the 'left-hand side'; white background identifies the part of the time series referred to as the 'right-hand side'. Each force and pressure history is normalized by the part of the timeseries within the grey-shaded region. AR: aspect ratio. Scaled-up dimensions for each analog iceberg are given beside each event, below the Experiment number. L: iceberg length in m scaled up to glacier dimensions; H: iceberg height in m scaled up to glacier dimensions. Positive vertical-axis values represent horizontal force in the up-glacier direction, and an increase in pressure. Time = 0 in each experiment represents the time at which the capsizing iceberg first reached horizontal. 'a', 'b', and 'c' in the top left panel refer to parts of the horizontal-force histories discussed in the text.

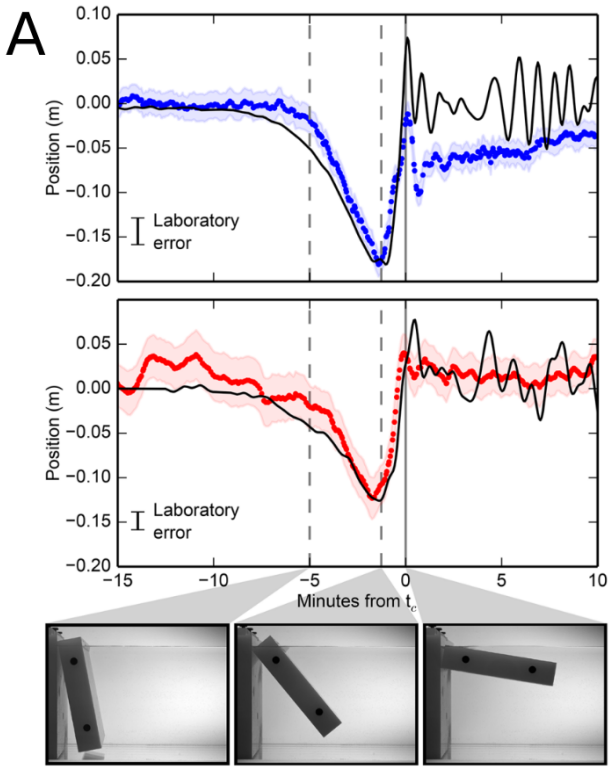

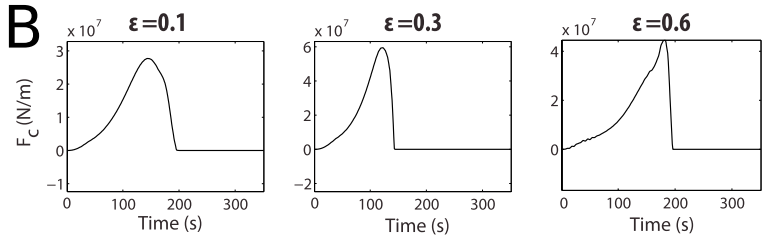

Figure 3.5: Constraints on the glacial-earthquake source from previous studies. A. From Murray et al. (2015a). Top two panels show laboratory data (black lines), scaled up to glacier dimensions and used to predict position deflections, compared to horizontal GPS displacement data (blue) and vertical GPS displacement data (red) collected during an iceberg-calving event. Bottom three photographs show the capsize stages of the analog iceberg that generated the laboratory data. Image times are indicated by the dashed and solid grey lines in the upper two panels. Analog iceberg aspect ratio is 0.22. B. Figure modified from Sergeant et al. (2018), Figure 9. Horizontal-force histories calculated using a finite-element model for bottom-out calving events with three different aspect ratios (ϵ).

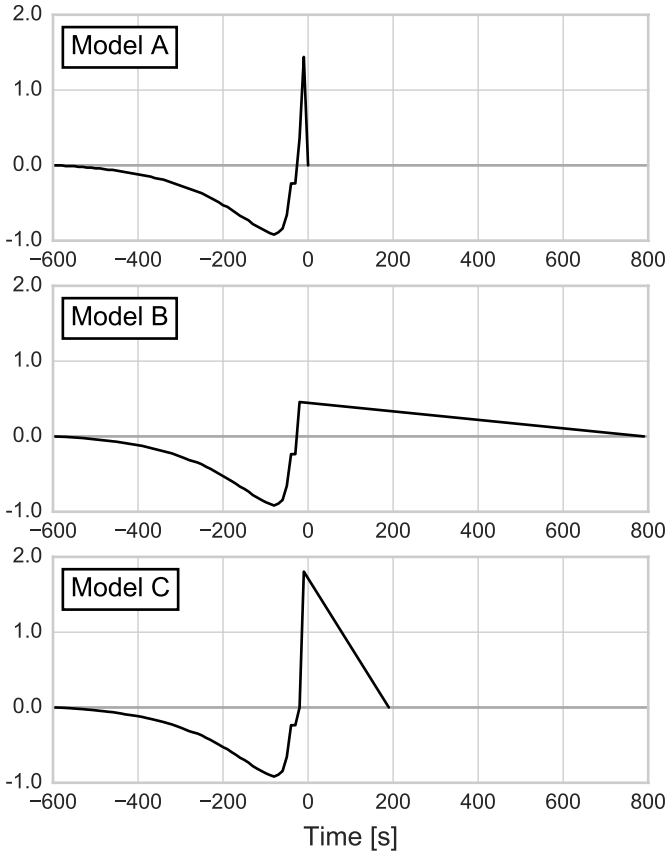

Figure 3.6: Fixed-source-time-function (FSTF) models used in this study. Left-hand side of each force history, from $t = -600$ s to the first zero crossing, is calculated by aligning the normalized horizontal force histories recorded during eight laboratory experiments on their zero-crossing time and taking the average. The portion of Model A after the zero-crossing time is also taken from the laboratory average. The portion of Model B after the zero-crossing time is constructed so that the maximum-force value is one half of the maximum value on the left-hand side, and the areas of the two sides are equal. The portion of Model C after the zero-crossing time is constructed so that the maximum-force value is twice the maximum value on the left-hand side, and the areas of the two sides are equal.

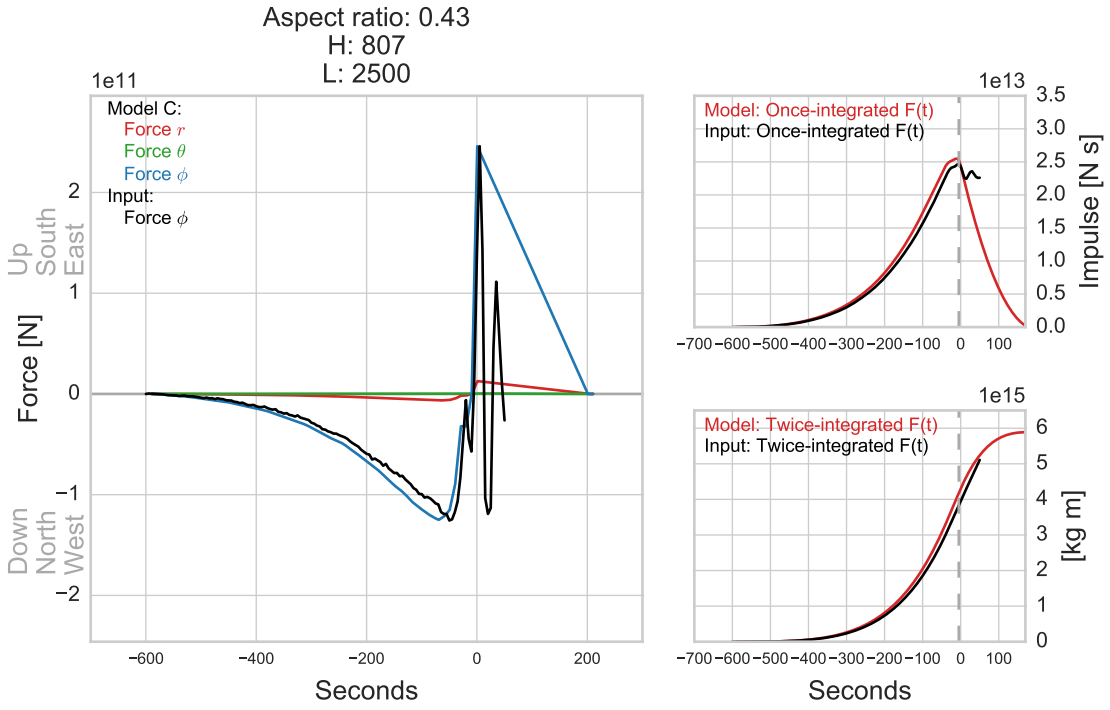

Figure 3.7: Force history for laboratory experiment 8 and recovered history using Model C. Input vertical force not shown. Panels on right show once- and twice-integrated force histories. Dashed grey line indicates the time of the maximum impulse value of the input source. The value of the twice-integrated force history of the source discussed in the text is measured at the time of the grey dashed line.

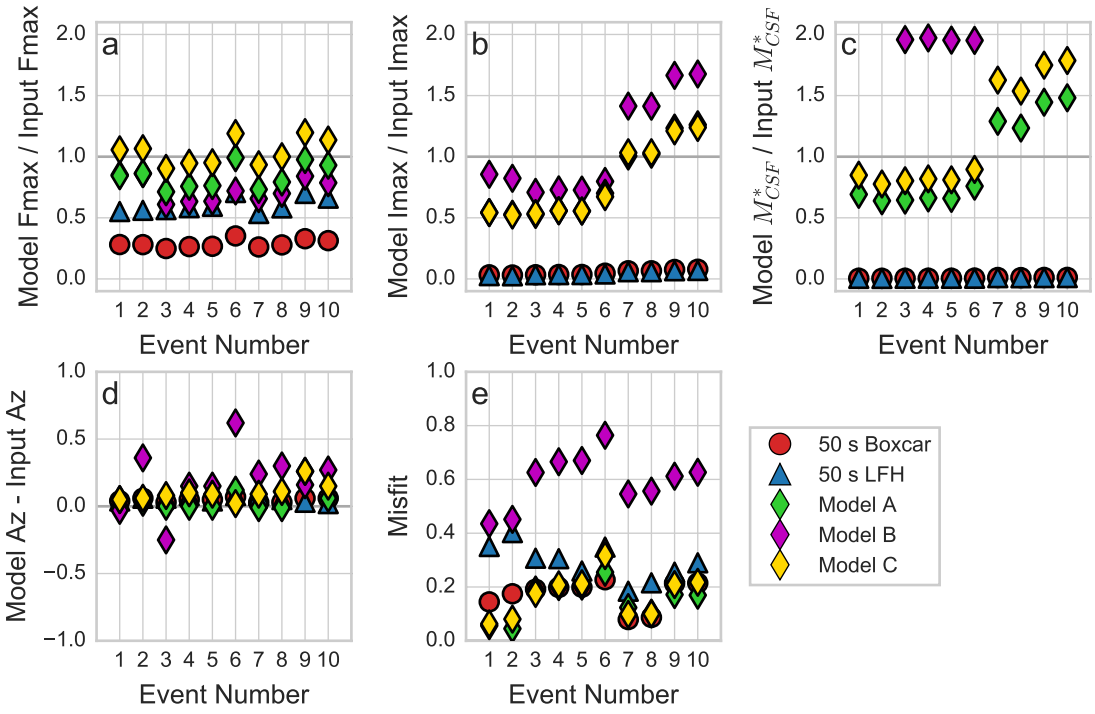

Figure 3.8: Source-parameter recovery results for the five models discussed in the text. Event number (horizontal axes of all panels) refers to the laboratory experiments shown in Figure 3.4. Panel (a) shows a comparison of maximum-force results (F_{Max} identified as in Figure 3.2d). Panel (b) shows a comparison of maximum-impulse results (I_{Max} identified as in Figure 3.2e). Panel (c) shows a comparison of M^*_{CSF} results (M^*_{CSF} identified as in Figure 3.2f). Panel (d) shows the difference between input and recovered force azimuth for each event in degrees E of N. Panel (e) shows inversion misfit values for each model. Some symbols plot beneath others, and some data points for Model B in panel (c) plot beyond the limits of the figure.

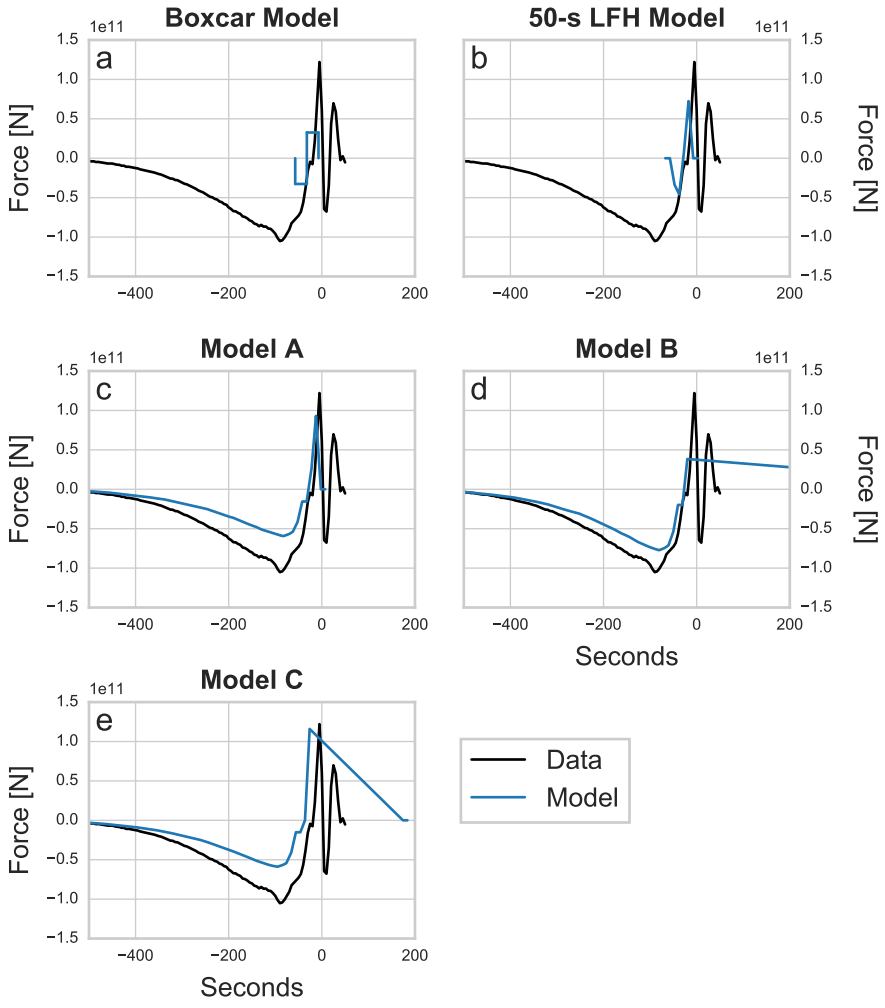

Figure 3.9: Horizontal-force data from Experiment 5 (Figure 3.4), shown with the east-west components of the horizontal-force results recovered using the five models described in this study. Model B extends beyond the edge of the figure, to ∼800 s.

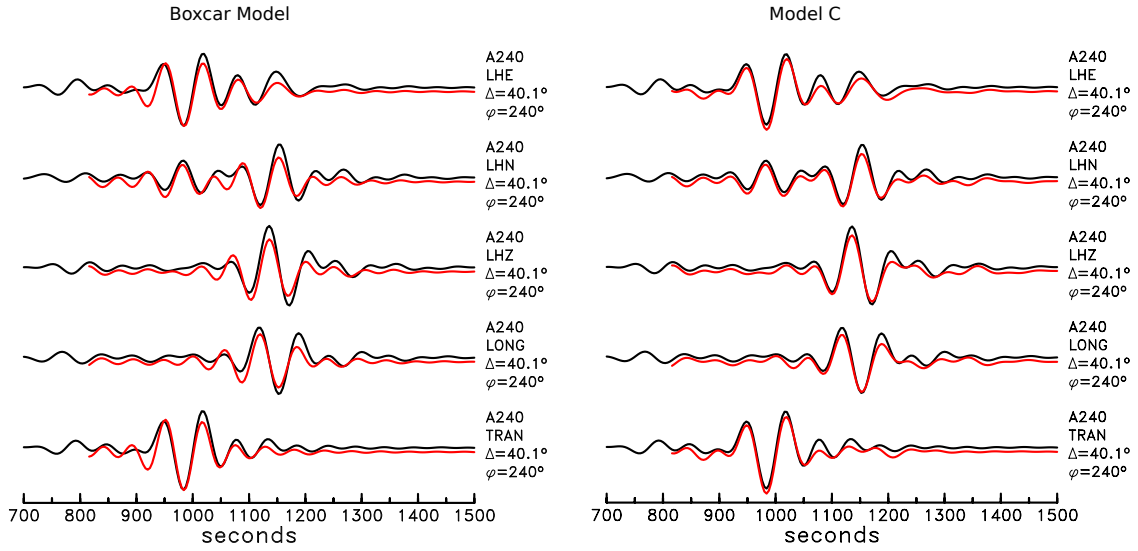

Figure 3.10: Seismograms (black) showing surface waves generated using tank-derived Experiment 1 (Figure 3.4) and best-fit waveforms (red) calculated using a 50-s boxcar model (left panel) and Model C (right panel). Seismograms are calculated at a synthetic station located at azimuth 240° E of N and distance ∼40° from the event location. All data are velocity records, bandpass filtered to 50-150 s. The channel names LHE, LHN, and LHZ refer to the east, north, and vertical components of ground motion, and LONG and TRAN refer to records of longitudinal and transverse motion calculated by rotating the horizontal time series.

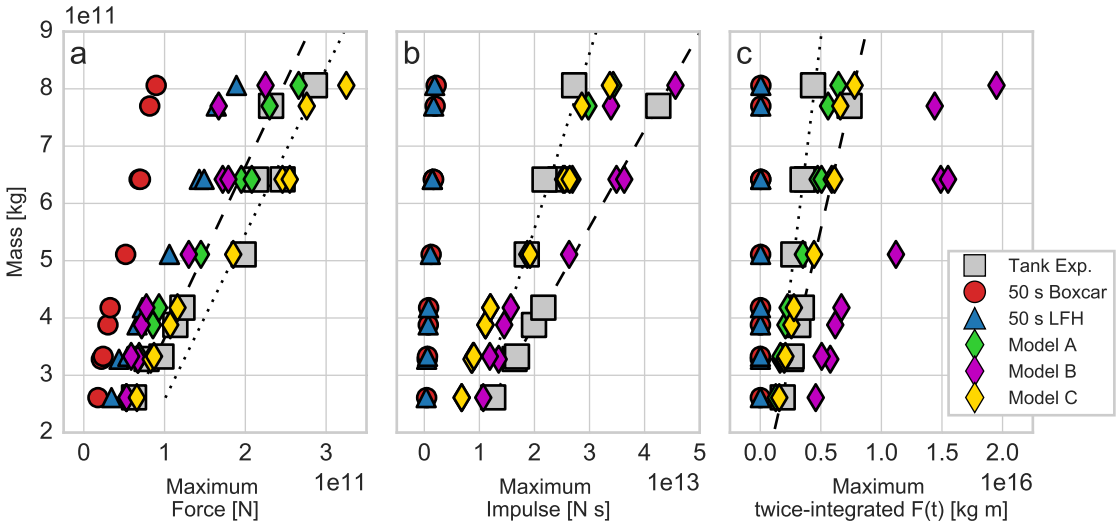

Figure 3.11: Measures of seismic magnitude versus mass for tank-derived data and model results. Laboratory mass values ("Tank Exp.") are measured from scaled-up analog iceberg dimensions. Laboratory maximum force, maximum impulse, and twice-integrated F(t) values (M^*_{CSF}) are measured as shown in Figure 3.2 and described in section 3.3.3. Black dotted line indicates best fit to the four laboratory experiments with large aspect ratios (0.43 and 0.54). Black dashed line indicates best fit to the six laboratory experiments with small aspect ratios (0.22 and 0.28).

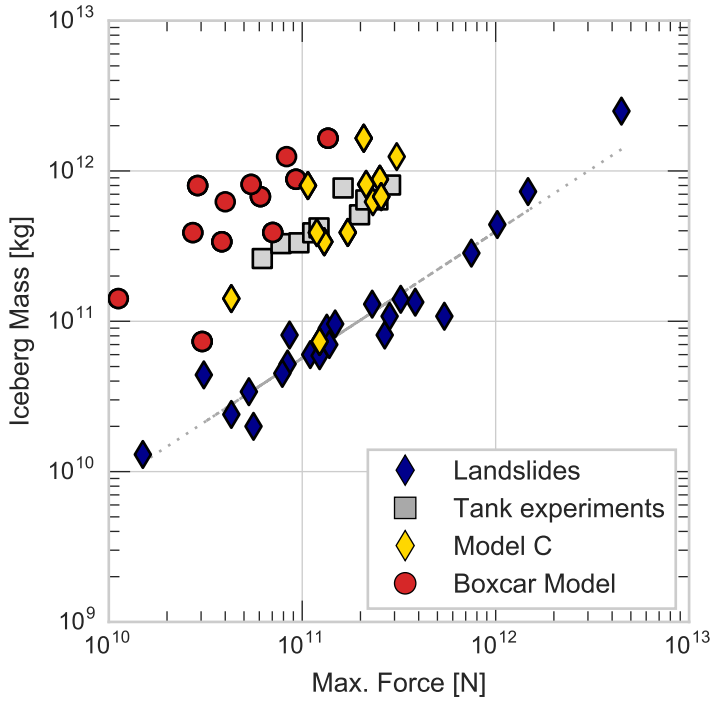

Figure 3.12: Maximum force values versus mass for (blue diamonds) landslides analyzed by Ekström and Stark (2013), Hibert et al. (2014), and Hibert et al. (2015); (grey squares) measured maximum-force values and iceberg masses from the ten scaled-up laboratory experiments used in this study; (red circles) twelve glacial earthquakes shown as circles, squares, and blue star in Figure 3.1 analyzed using a 50-s boxcar model, and (yellow diamonds) analyzed using Model C.

Conclusion

The research presented in this dissertation represents a step forward in our understanding of ice loss at the termini of Greenland tidewater glaciers. I have advanced understanding of how ice is lost, both the driving mechanisms and the distribution of iceberg sizes, when and where large calving events occur, and how calving behavior at Greenland's largest glaciers has evolved with time.

I employ the high-quality GLISN network located around Greenland to study smaller glacial-earthquake signals than has previously been possible, and detail these results in Chapter Two. I identify new, small seismic events before half of the glacial earthquakes I investigate, and following one third of such events. My waveform-modeling results demonstrate that these signals are small glacial earthquakes, generated by near-horizontal forces acting perpendicular to the glacier terminus. These results expand our understanding of buoyancy-driven calving and demonstrate that this mechanism acts on icebergs up to two orders of magnitude smaller than previously realized. These results reveal ∼25% more mass loss through buoyancy-driven calving than previously recognized, and highlight the strength of using multiple seismic analysis techniques to investigate the forces exerted on the Earth during calving.

I present the first empirical relationships between the size of a glacial earthquake and the volume of the iceberg lost. This important advance moves us closer to using a seismological observable to remotely assess mass loss at distant glaciers. In Chapter Two I demonstrate a relationship between iceberg size and M_{CSF}, the integrated

measure of glacial-earthquake size that has been reported to date. In Chapter Three I further refine the ability of waveform-modeling results to describe iceberg size, through development of new models of the glacial-earthquake source. I demonstrate that the maximum force generated by an iceberg during calving is a robust size metric of glacial-earthquake magnitude, and has the advantage of being relatively insensitive to modeling choices. These results suggest testable hypotheses for future work.

My experiments using synthetic seismograms confirm that the force orientations estimated in glacial-earthquake analysis are very robust, as are estimates of glacial-earthquake location. This provides further evidence that seismically recovered source parameters, such as those I calculate in Chapters One and Two, accurately record changes occurring at a glacier terminus and can be used to examine Greenland-wide trends of dynamic mass loss. The result is new knowledge about a glacier's grounded state, frequency of buoyancy-driven calving, and the range of iceberg sizes lost through this mechanism. The work in this dissertation has global importance in its implications for failure mechanisms of tall ice cliffs and terminus behavior around the Antarctic Ice Sheet in addition to illuminating Greenland-wide patterns of mass loss. In addition to furthering our knowledge of dynamic changes at Greenland glaciers, the research in this dissertation advances our understanding of an increasingly important part of the seismic wavefield, and therefore broadens our understanding of global seismicity. Results from this dissertation set the stage for future advances in glacial seismology, especially related to the use of improved seismic-magnitude estimates to calculate mass loss from calving, using glacial earthquakes.

References

Jason M Amundson and Martin Truffer. A unifying framework for iceberg-calving models. *J. Glaciol.*, 56(199):822–830, 2010. doi:10.3189/002214310794457173.

Jason M Amundson, Martin Truffer, Martin P Lüthi, Mark Fahnestock, Michael E West, and Roman J Motyka. Glacier, fjord, and seismic response to recent large calving events, Jakobshavn Isbræ, Greenland. *Geophysical Research Letters*, 35(22), 2008. doi:10.1029/2008GL035281.

Jason M Amundson, Mark Fahnestock, Martin Truffer, Jed Brown, Martin P Lüthi, and Roman J Motyka. Ice mélange dynamics and implications for terminus stability, Jakobshavn Isbræ, Greenland. *Journal of Geophysical Research: Earth Surface*, 115 (F1), 2010. doi:10.1029/2009JF001405.

Jason M Amundson, Justin C Burton, and Sergio Correa-Legisos. Impact of hydrodynamics on seismic signals generated by iceberg collisions. *Annals of Glaciology*, 53 (60):106–112, 2012. doi:10.3189/2012/AoG60A012.

Sridhar Anandakrishnan and Charles R Bentley. Micro-earthquakes beneath Ice Streams B and C, West Antarctica: observations and implications. *Journal of Glaciology*, 39(133):455–462, 1993. doi:10.3189/S0022143000016348.

Timothy C Bartholomaus, Jason M Amundson, Jacob I Walter, Shad O'Neel, Michael E West, and Christopher F Larsen. Subglacial discharge at tidewater glaciers revealed by seismic tremor. *Geophysical research letters*, 42(15):6391–6398, 2015. doi:10.1002/2015GL064590.

Jeremy N Bassis and Catherine C Walker. Upper and lower limits on the stability of calving glaciers from the yield strength envelope of ice. *Proc. R. Soc. A*, pages 913–931, 2012. doi:10.1098/rspa.2011.0422.

Douglas I Benn, Charles R Warren, and Ruth H Mottram. Calving processes and the dynamics of calving glaciers. *Earth-Sci. Rev.*, 82(3):143–179, 2007. doi:10.1016/j.earscirev.2007.02.002.

Douglas I Benn, Jan Åström, Thomas Zwinger, Joe Todd, Faezeh M Nick, Susan Cook, Nicholas RJ Hulton, and Adrian Luckman. Melt-under-cutting and buoyancy-driven calving from tidewater glaciers: new insights from discrete element and continuum model simulations. *Journal of Glaciology*, 63(240):691–702, 2017. doi:10.1017/jog.2017.41.

Suzanne L Bevan, Adrian J Luckman, and Tavi Murray. Glacier dynamics over the last quarter of a century at Helheim, Kangerdlugssuaq and 14 other major Greenland outlet glaciers. *Cryosphere*, 6(5):923–937, 2012. doi:10.5194/tc-6-923-2012.

Claus W Böning, Erik Behrens, Arne Biastoch, Klaus Getzlaff, and Jonathan L Bamber. Emerging impact of Greenland meltwater on deepwater formation in the North Atlantic Ocean. *Nature Geoscience*, 9(7):523, 2016. doi:10.1038/ngeo2740.

Justin C Burton, Jason M Amundson, Dorian S Abbot, Alexandra Boghosian, L Mac Cathles, S Correa-Legisos, Kristopher N Darnell, Nicholas Guttenberg, David M Holland, and Douglas R MacAyeal. Laboratory investigations of iceberg capsize dynamics, energy dissipation and tsunamigenesis. *Journal of Geophysical Research: Earth Surface*, 117(F1), 2012. doi:10.1029/2011JF002055.

J Rachel Carr, Andreas Vieli, and Chris Stokes. Influence of sea ice decline, atmospheric warming, and glacier width on marine-terminating outlet glacier behavior in northwest Greenland at seasonal to interannual timescales. *J. Geophys. Res.: Earth Surf.*, 118(3):1210–1226, 2013. doi:10.1002/jgrf.20088.

Ryan Cassotto, Mark Fahnestock, Jason M Amundson, Martin Truffer, and Ian Joughin. Seasonal and interannual variations in ice melange and its impact on terminus stability, Jakobshavn Isbræ, Greenland. *J. Glaciol.*, 61(225):76–88, 2015. doi:10.3189/2015JoG13J235.

L. Mac Cathles, LM Kaluzienski, and Justin C Burton. Laboratory investigations of seismicity caused by iceberg calving and capsize. In *AGU Fall Meeting Abstracts*, number C43B-0803. American Geophysical Union Fall Meeting, December 2015.

Nolwenn Chauché, Alun Hubbard, Jean-Claude Gascard, Jason E Box, R Bates, Michele Koppes, A Sole, Poul Christoffersen, and Henry Patton. Ice–ocean interaction and calving front morphology at two west Greenland tidewater outlet glaciers. *Cryosphere*, 8(4):1457–1468, 2014. doi:10.5194/tc-8-1457-2014.

John F Clinton, Meredith Nettles, Fabian Walter, Kent Anderson, Trine Dahl-Jensen, Domenico Giardini, Aladino Govoni, Winfried Hanka, Stanislaw Lasocki, Won Sang Lee, et al. Seismic network in Greenland monitors Earth and ice system. *Eos, Transactions American Geophysical Union*, 95(2):13–14, 2014. doi:10.1002/2014EO020001.

Trine Dahl-Jensen, Tine B Larsen, Ingo Woelbern, Torben Bach, Winfried Hanka, Rainer Kind, Søren Gregersen, Klaus Mosegaard, Peter Voss, and Olafur Gudmundsson. Depth to Moho in Greenland: receiver-function analysis suggests two Proterozoic blocks in Greenland. *Earth and Planetary Science Letters*, 205(3-4):379–393, 2003. doi:10.1016/S0012-821X(02)01080-4.

Fiona A Darbyshire, Trine Dahl-Jensen, Tine B Larsen, Peter H Voss, and Guillaume Joyal. Crust and uppermost-mantle structure of Greenland and the Northwest Atlantic from Rayleigh wave group velocity tomography. *Geophysical Journal International*, 212(3):1546–1569, 2017. doi:10.1093/gji/ggx479.

Robert M DeConto and David Pollard. Contribution of Antarctica to past and future sea-level rise. *Nature*, 531(7596):591, 2016. doi:10.1038/nature17145.

Reinhard Dietrich, Hans-Gerd Maas, Marco Baessler, Axel Rülke, Andreas Richter, E Schwalbe, and Patrick Westfeld. Jakobshavn Isbræ, west Greenland: Flow velocities and tidal interaction of the front area from 2004 field observations. *J. Geophys. Res.: Earth Surf.*, 112(F3):F03S21, 2007. doi:10.1029/2006JF000601.

Adam M Dziewoński and Don L Anderson. Preliminary reference Earth model. *Phys. Earth Planet. Inter.*, 25(4):297–356, 1981. doi:10.1016/0031-9201(81)90046-7.

Adam M Dziewoński, T-A Chou, and John H Woodhouse. Determination of earthquake source parameters from waveform data for studies of global and regional seismicity. *J. Geophys. Res.: Solid Earth*, 86(B4):2825–2852, 1981.

Göran Ekström. Global detection and location of seismic sources by using surface waves. *Bull. Seismol. Soc. Am.*, 96(4A):1201–1212, 2006. doi:10.1785/0120050175.

Göran Ekström and Meredith Nettles. Long-Period Moment-Tensor Inversion: The Global CMT Project. *Encyclopedia of Earthquake Engineering*, pages 1–13, 2014. doi:10.1007/978-3-642-36197-5_291-1.

Göran Ekström and Colin P Stark. Simple scaling of catastrophic landslide dynamics. *Science*, 339(6126):1416–1419, 2013. doi:10.1126/science.1232887.

Göran Ekström, Jeroen Tromp, and Erik W.F. Larson. Measurements and global models of surface wave propagation. *Journal of Geophysical Research: Solid Earth*, 102(B4):8137–8157, 1997. doi:10.1029/96JB03729.

Göran Ekström, Meredith Nettles, and Geoffrey A Abers. Glacial earthquakes. *Science*, 302(5645):622–624, 2003. doi:10.1126/science.1088057.

Göran Ekström, Meredith Nettles, and Victor C Tsai. Seasonality and increasing frequency of Greenland glacial earthquakes. *Science*, 311(5768):1756–1758, 2006. doi:10.1126/science.1122112.

Göran Ekström, Meredith Nettles, and Adam M Dziewoński. The global CMT project 2004–2010: centroid-moment tensors for 13,017 earthquakes. *Phys. Earth Planet. Inter.*, 200:1–9, 2012. doi:10.1016/j.pepi.2012.04.002.

Ellyn M Enderlin, Ian M Howat, Seongsu Jeong, Myoung-Jong Noh, Jan H Angelen, and M R van den Broeke. An improved mass budget for the Greenland ice sheet. *Geophys. Res. Lett.*, 41(3):866–872, 2014. doi:10.1002/2013GL059010.

Mason J Fried, GA Catania, TC Bartholomaus, D Duncan, M Davis, LA Stearns, J Nash, E Shroyer, and D Sutherland. Distributed subglacial discharge drives signifi-

cant submarine melt at a Greenland tidewater glacier. *Geophysical Research Letters*, 42(21):9328–9336, 2015. doi:10.1002/2015GL065806.

Lucia Gualtieri and Göran Ekström. Seismic reconstruction of the 2012 Palisades rockfall using the analytical solution to Lamb's problem. *Bulletin of the Seismological Society of America*, 107(1):63–71, 2016. doi:10.1785/0120160238.

Christopher Harig and Frederik J Simons. Ice mass loss in Greenland, the Gulf of Alaska, and the Canadian Archipelago: Seasonal cycles and decadal trends. *Geophys. Res. Lett.*, 43(7):3150–3159, 2016. doi:10.1002/2016GL067759.

Clément Hibert, Göran Ekström, and Colin P Stark. Dynamics of the Bingham Canyon Mine landslides from seismic signal analysis. *Geophysical research letters*, 41(13): 4535–4541, 2014. doi:10.1002/2014GL060592.

Clément Hibert, Colin P Stark, and Göran Ekström. Dynamics of the Oso-Steelhead landslide from broadband seismic analysis. *Natural Hazards and Earth System Sciences*, 15(6):1265–1273, 2015. doi:10.5194/nhess-15-1265-2015.

Anna E Hogg, Andrew Shepherd, Noel Gourmelen, and Marcus Engdahl. Grounding line migration from 1992 to 2011 on Petermann Glacier, North-West Greenland. *J. Glaciol.*, 62(236):1104–1114, 2016. doi:10.1017/jog.2016.83.

David M Holland, Robert H Thomas, Brad De Young, Mads H Ribergaard, and Bjarne Lyberth. Acceleration of Jakobshavn Isbræ triggered by warm subsurface ocean waters. *Nat. Geosci.*, 1(10):659–664, 2008. doi:10.1038/ngeo316.

Ian M Howat and Alex Eddy. Multi-decadal retreat of Greenland's marine-terminating glaciers. *J. Glaciol.*, 57(203):389–396, 2011. doi:10.3189/002214311796905631.

Ian M Howat, I Joughin, S Tulaczyk, and S Gogineni. Rapid retreat and acceleration of Helheim Glacier, east Greenland. *Geophysical Research Letters*, 32(22), 2005. doi:10.1029/2005GL024737.

Ian M Howat, Ian Joughin, and Ted A Scambos. Rapid changes in ice discharge from Greenland outlet glaciers. *Science*, 315(5818):1559–1561, 2007. doi:10.1126/science.1138478.

Timothy D James, Tavi Murray, Nick Selmes, Kilian Scharrer, and Martin O'Leary. Buoyant flexure and basal crevassing in dynamic mass loss at Helheim Glacier. *Nat. Geosci.*, 7(8):593–596, 2014. doi:10.1038/NGEO2204.

Trine S Jensen, Jason E Box, and Christine S Hvidberg. A sensitivity study of annual area change for Greenland ice sheet marine terminating outlet glaciers: 1999–2013. *J. Glaciol.*, 62(231):72–81, 2016. doi:10.1017/ jog.2016.12.

Ian Joughin, Ian Howat, Richard B Alley, Göran Ekström, Mark Fahnestock, Twila Moon, Meredith Nettles, Martin Truffer, and Victor C Tsai. Ice-front variation and tidewater behavior on Helheim and Kangerdlugssuaq Glaciers, Greenland. *Journal of Geophysical Research: Earth Surface*, 113(F1), 2008a. doi:10.1029/2007JF000837.

Ian Joughin, Ian M Howat, Mark Fahnestock, Ben Smith, William Krabill, Richard B Alley, Harry Stern, and Martin Truffer. Continued evolution of Jakobshavn Isbræ following its rapid speedup. *J. Geophys. Res.: Earth Surf.*, 113(F4):F04006, 2008b. doi:10.1029/2008JF001023.

Ian Joughin, Ben E Smith, Ian M Howat, Dana Floricioiu, Richard B Alley, Martin Truffer, and Mark Fahnestock. Seasonal to decadal scale variations in the surface velocity of Jakobshavn Isbrae, Greenland: Observation and model-based analysis. *Journal of Geophysical Research: Earth Surface*, 117(F2), 2012. doi:10.1029/2011JF002110.

Ian Joughin, Ben E Smith, David E Shean, and Dana Floricioiu. Brief communication: Further summer speedup of Jakobshavn Isbræ. *Cryosphere*, 8:209–214, 2014. doi:10.5194/tc-8-209-2014.

Hitoshi Kawakatsu. Centroid single force inversion of seismic waves generated by landslides. *J. Geophys. Res.: Solid Earth*, 94(B9):12363–12374, 1989. doi:10.1029/JB094iB09p12363.

Laura M Kehrl, Ian Joughin, David E Shean, Dana Floricioiu, and Lukas Krieger. Seasonal and interannual variabilities in terminus position, glacier velocity, and surface elevation at Helheim and Kangerlussuaq Glaciers from 2008 to 2016. *J. Geophys. Res.: Earth Surf.*, 122, 2017. doi:10.1002/2016JF004133.

Shfaqat A Khan, Andy Aschwanden, Anders A Bjørk, John Wahr, Kristian K Kjeldsen, and Kurt H Kjaer. Greenland ice sheet mass balance: a review. *Reports on Progress in Physics*, 78(4):046801, 2015. doi:10.1088/0034-4885/78/4/046801.

Peter Lemke, Jiawen Ren, Richard B Alley, Ian Allison, Jorge Carrasco, Gregory Flato, Yoshiyuki Fujii, Georg Kaser, Philip Mote, Robert H Thomas, et al. Observations: changes in snow, ice and frozen ground. In Solomon, S., Qin, D., Manning, M., Chen, Z., Marquis, M., Averyt, K.B., Tignor, M., Miller, H.L., editor, *Climate Change 2007: The Physical Science Basis*, volume Contribution of Working Group 1 to the Fourth Assessment Report of the Intergovernmnetal Panel on Climate Change, page 996. Cambridge University Press, 2007.

Yue Ma, Cory S Tripathy, and Jeremy N Bassis. Bounds on the calving cliff height of marine terminating glaciers. *Geophysical Research Letters*, 44(3):1369–1375, 2017. doi:10.1002/2016GL071560.

Douglas R MacAyeal, Emile A Okal, Richard C Aster, and Jeremy N Bassis. Seismic

and hydroacoustic tremor generated by colliding icebergs. *Journal of Geophysical Research: Earth Surface*, 113(F3), 2008. doi:10.1029/2008JF001005.

Ellyn M McFadden, Ian M Howat, Ian Joughin, Ben E Smith, and Yushin Ahn. Changes in the dynamics of marine terminating outlet glaciers in west Greenland (2000–2009). *J. Geophys. Res.: Earth Surf.*, 116(F2):F02022, 2011. doi:10.1029/2010JF001757.

Twila Moon, Ian Joughin, Ben E Smith, and Ian M Howat. 21st-century evolution of Greenland outlet glacier velocities. *Science*, 336(6081):576–578, 2012. doi:10.1126/science.1219985.

R.J. Motyka. *Calving Glaciers: Report of a Workshop*, volume 15, chapter Deep-water calving at Le Conte glacier, southeast Alaska, pages 115–118. Ohio State University, Columbus., Feb. 28–March 2, 1997 1997. doi:10.3189/S0022143000031014.

Tavi Murray, Meredith Nettles, Nick Selmes, L Mac Cathles, Justin C Burton, Timothy D James, Stuart Edwards, Ian Martin, Timothy O'Farrell, Robin Aspey, et al. Reverse glacier motion during iceberg calving and the cause of glacial earthquakes. *Science*, 349(6245):305–308, 2015a. doi:10.1126/science.aab0460.

Tavi Murray, Kilian Scharrer, Nick Selmes, Adam D Booth, Timothy D James, Suzanne L Bevan, Jerry A Bradley, Susan Cook, L Cordero Llana, Yoann Drocourt, et al. Extensive retreat of Greenland tidewater glaciers, 2000-2010. *Arct. Antarct. Alp. Res.*, 47(3):427–447, 2015b. doi:10.1657/AAAR0014-049.

Tavi Murray, Nick Selmes, Timothy D James, Stuart Edwards, Ian Martin, Timothy O'Farrell, Robin Aspey, Ian Rutt, Meredith Nettles, and Tim Baugé. Dynamics of glacier calving at the ungrounded margin of Helheim Glacier, southeast Greenland. *J. Geophys. Res.: Earth Surf.*, 120(6):964–982, 2015c. doi:10.1002/2015JF003531.

Meredith Nettles and Göran Ekström. Glacial earthquakes in Greenland and Antarctica. *Annual Review of Earth and Planetary Sciences*, 38, 2010. doi:10.1146/annurev-earth-040809-152414.

Meredith Nettles, Tine B Larsen, P Elósegui, Gordon S Hamilton, Leigh A Stearns, Andreas P Ahlstrøm, Jim L Davis, Morten L Andersen, Julia de Juan, Shfaqat Abbas Khan, et al. Step-wise changes in glacier flow speed coincide with calving and glacial earthquakes at Helheim Glacier, Greenland. *Geophys. Res. Lett.*, 35(24):L24503, 2008. doi:10.1029/2008GL036127.

Faezeh M Nick, Cornelis J Van der Veen, Andreas Vieli, and Douglas I Benn. A physically based calving model applied to marine outlet glaciers and implications for the glacier dynamics. *Journal of Glaciology*, 56(199):781–794, 2010. doi:10.3189/002214310794457344.

Faezeh M Nick, Andreas Vieli, Morten Langer Andersen, Ian Joughin, Antony Payne, Tamsin L Edwards, Frank Pattyn, and Roderik SW van de Wal. Future sea-level rise from Greenland's main outlet glaciers in a warming climate. *Nature*, 497(7448): 235–238, 2013. doi:10.1038/nature12068.

Kira G Olsen and Meredith Nettles. Patterns in glacial-earthquake activity around Greenland, 2011–13. *Journal of Glaciology*, 63(242):1077–1089, 2017. doi:10.1017/jog.2017.78.

Kira G Olsen and Meredith Nettles. Constraints on terminus dynamics at Greenland glaciers from small glacial earthquakes. *Journal of Geophysical Research: Earth Surface*, 2019. doi:10.1029/2019JF005054.

Shad O'Neel, Hans P Marshall, Daniel E McNamara, and William Tad Pfeffer. Seismic detection and analysis of icequakes at Columbia Glacier, Alaska. *Journal of Geophysical Research: Earth Surface*, 112(F3), 2007. doi:10.1029/2006JF000595.

David Pollard, Robert M DeConto, and Richard B Alley. Potential Antarctic Ice Sheet retreat driven by hydrofracturing and ice cliff failure. *Earth and Planetary Science Letters*, 412:112–121, 2015. doi:10.1016/j.epsl.2014.12.035.

Niels Reeh. On the calving of ice from floating glaciers and ice shelves. *Journal of Glaciology*, 7(50):215–232, 1968. doi:10.3189/S0022143000031014.

Jose A Rial, Chaunhai Tang, and Konrad Steffen. Glacial rumblings from Jakobshavn ice stream, Greenland. *Journal of Glaciology*, 55(191):389–399, 2009. doi:10.3189/002214309788816623.

Eric Rignot, Ian Fenty, Yun Xu, Cilan Cai, and Chris Kemp. Undercutting of marine-terminating glaciers in West Greenland. *Geophysical Research Letters*, 42(14):5909–5917, 2015. doi:10.1002/2015GL064236.

Eric Rignot, Ian Fenty, Yun Xu, Cilan Cai, Isabella Velicogna, Colm Ó Cofaigh, Julian A Dowdeswell, W Weinrebe, Ginny A Catania, and Daniel D Duncan. Bathymetry data reveal glaciers vulnerable to ice-ocean interaction in Uummannaq and Vaigat glacial fjords, west Greenland. *Geophys. Res. Lett.*, 43(6):2667–2674, 2016. doi:10.1002/2016GL067832.

Claudia Röösli, Fabian Walter, Stephan Husen, Lauren C Andrews, Martin P Lüthi, Ginny A Catania, and Edi Kissling. Sustained seismic tremors and icequakes detected in the ablation zone of the Greenland ice sheet. *Journal of Glaciology*, 60(221):563–575, 2014. doi:10.3189/2014JoG13J210.

Claudia Röösli, Agnes Helmstetter, Fabian Walter, and Edi Kissling. Meltwater influences on deep stick-slip icequakes near the base of the Greenland Ice

Sheet. *Journal of Geophysical Research: Earth Surface*, 121(2):223–240, 2016a. doi:10.1002/2015JF003601.

Claudia Röösli, Fabian Walter, Jean-Paul Ampuero, and Edi Kissling. Seismic moulin tremor. *Journal of Geophysical Research: Solid Earth*, 121(8):5838–5858, 2016b. doi:10.1002/2015JB012786.

Ralf Rosenau, Ed Schwalbe, Hans-Gerd Maas, Marco Baessler, and Reinhard Dietrich. Grounding line migration and high-resolution calving dynamics of Jakobshavn Isbræ, West Greenland. *Journal of Geophysical Research: Earth Surface*, 118(2):382–395, 2013. doi:10.1029/2012JF002515.

Anthony Seale, Poul Christoffersen, Ruth I Mugford, and Martin O'Leary. Ocean forcing of the Greenland Ice Sheet: Calving fronts and patterns of retreat identified by automatic satellite monitoring of eastern outlet glaciers. *J. Geophys. Res.: Earth Surf.*, 116(F3):F03013, 2011. doi:10.1029/2010JF001847.

Amandine Sergeant, Anne Mangeney, Eléonore Stutzmann, J Montagner, Fabian Walter, Laurent Moretti, and Olivier Castelnau. Complex force history of a calving-generated glacial earthquake derived from broadband seismic inversion. *Geophys. Res. Lett.*, 43(3):2015GL066785, 2016. doi:10.1002/2015GL066785.

Amandine Sergeant, Vladislav A Yastrebov, Anne Mangeney, Olivier Castelnau, Jean-Paul Montagner, and Eléonore Stutzmann. Numerical modeling of iceberg capsizing responsible for glacial earthquakes. *Journal of Geophysical Research: Earth Surface*, 123(11):3013–3033, 2018. doi:10.1029/2018JF004768.

Amandine Sergeant, Anne Mangeney, Vladislav A Yastrebov, Fabian Walter, Jean-Paul Montagner, Olivier Castelnau, Eléonore Stutzmann, Pauline Bonnet, Velotioana Jean-Luc Ralaiarisoa, Suzanne Bevan, et al. Monitoring Greenland ice sheet buoyancy-driven calving discharge using glacial earthquakes. *Annals of Glaciology*, pages 1–21, 2019. doi:10.1017/aog.2019.7.

Victor C Tsai and Göran Ekström. Analysis of glacial earthquakes. *J. Geophys. Res.: Earth Surf.*, 112(F3):F03S22, 2007. doi:10.1029/2006JF000596.

Victor C Tsai, James R Rice, and Mark Fahnestock. Possible mechanisms for glacial earthquakes. *Journal of Geophysical Research: Earth Surface*, 113(F3), 2008. doi:10.1029/2007JF000944.

Michiel van den Broeke, Jonathan Bamber, Janneke Ettema, Eric Rignot, Ernst Schrama, Willem Jan van de Berg, Erik van Meijgaard, Isabella Velicogna, and Bert Wouters. Partitioning recent Greenland mass loss. *science*, 326(5955):984–986, 2009. doi:10.1126/science.1178176.

Stephen A Veitch and Meredith Nettles. Spatial and temporal variations in Greenland glacial-earthquake activity, 1993–2010. *J. Geophys. Res.: Earth Surf.*, 117(F4):ISSN 2156–2202, 2012. doi:10.1029/2012JF002412.

Stephen A Veitch and Meredith Nettles. Assessment of glacial-earthquake source parameters. *Journal of Glaciology*, 63(241):867–876, 2017. doi:10.1017/jog.2017.52.

Isabella Velicogna, Tyler C Sutterley, and Michiel R van den Broeke. Regional acceleration in ice mass loss from Greenland and Antarctica using GRACE time-variable gravity data. *Geophys. Res. Lett.*, 41(22):8130–8137, 2014. doi:10.1002/2014GL061052.

Fabian Walter, John F Clinton, Nicholas Deichmann, Douglas S Dreger, Sarah E Minson, and Martin Funk. Moment tensor inversions of icequakes on Gornergletscher, Switzerland. *Bulletin of the Seismological Society of America*, 99(2A):852–870, 2009. doi:10.1785/0120080110.

Fabian Walter, Jason M Amundson, Shad O'Neel, Martin Truffer, Mark Fahnestock, and Helen A Fricker. Analysis of low-frequency seismic signals generated during a multiple-iceberg calving event at Jakobshavn Isbræ, Greenland. *J. Geophys. Res.: Earth Surf.*, 117(F1):F01036, 2012. doi:10.1029/2011JF002132.

Fabian Walter, Marco Olivieri, and John F Clinton. Calving event detection by observation of seiche effects on the Greenland fjords. *Journal of Glaciology*, 59(213): 162–178, 2013. doi:10.3189/2013JoG12J118.

Surui Xie, Timothy H Dixon, Denis Voytenko, Fanghui Deng, and David M Holland. Grounding line migration through the calving season at Jakobshavn Isbræ, Greenland, observed with terrestrial radar interferometry. *The Cryosphere*, 12(4):1387, 2018. doi:10.5194/tc-12-1387-2018.

Ashley V York, Karen E Frey, and Sarah B Das. Analyzing the effects of sea ice variability on marine-terminating glacier retreat, central west Greenland. Number 74A2090 in Symposium on Interactions of Ice Sheets and Glaciers with the Ocean, La Jolla, California, 10 - 15 July, 2016 2016. International Glaciological Society.